

**Predictive Model for  
Temperature-Induced Deformation  
of Robot Mechanical Systems**

by

**Pranchalee Poonyapak**

**B.Eng.**, Chulalongkorn University,

**M.Eng.**, Carleton University

A thesis submitted to  
the Faculty of Graduate Studies and Research  
in partial fulfillment of  
the requirements for the degree of

**Doctor of Philosophy**

Ottawa-Carleton Institute for  
Mechanical and Aerospace Engineering

Department of  
Mechanical and Aerospace Engineering  
Carleton University

Ottawa, Ontario

May 7, 2010

© Copyright

2010 - Pranchalee Poonyapak



Library and Archives  
Canada

Published Heritage  
Branch

395 Wellington Street  
Ottawa ON K1A 0N4  
Canada

Bibliothèque et  
Archives Canada

Direction du  
Patrimoine de l'édition

395, rue Wellington  
Ottawa ON K1A 0N4  
Canada

*Your file* *Votre référence*  
ISBN: 978-0-494-70554-4  
*Our file* *Notre référence*  
ISBN: 978-0-494-70554-4

**NOTICE:**

The author has granted a non-exclusive license allowing Library and Archives Canada to reproduce, publish, archive, preserve, conserve, communicate to the public by telecommunication or on the Internet, loan, distribute and sell theses worldwide, for commercial or non-commercial purposes, in microform, paper, electronic and/or any other formats.

The author retains copyright ownership and moral rights in this thesis. Neither the thesis nor substantial extracts from it may be printed or otherwise reproduced without the author's permission.

---

In compliance with the Canadian Privacy Act some supporting forms may have been removed from this thesis.

While these forms may be included in the document page count, their removal does not represent any loss of content from the thesis.

**AVIS:**

L'auteur a accordé une licence non exclusive permettant à la Bibliothèque et Archives Canada de reproduire, publier, archiver, sauvegarder, conserver, transmettre au public par télécommunication ou par l'Internet, prêter, distribuer et vendre des thèses partout dans le monde, à des fins commerciales ou autres, sur support microforme, papier, électronique et/ou autres formats.

L'auteur conserve la propriété du droit d'auteur et des droits moraux qui protègent cette thèse. Ni la thèse ni des extraits substantiels de celle-ci ne doivent être imprimés ou autrement reproduits sans son autorisation.

---

Conformément à la loi canadienne sur la protection de la vie privée, quelques formulaires secondaires ont été enlevés de cette thèse.

Bien que ces formulaires aient inclus dans la pagination, il n'y aura aucun contenu manquant.

  
**Canada**

The undersigned recommend to  
the Faculty of Graduate Studies and Research  
acceptance of the thesis

**Predictive Model for Temperature-Induced Deformation  
of Robot Mechanical Systems**

submitted by **Pranchalee Poonyapak, B.Eng., M.Eng.**

in partial fulfillment of the requirements for  
the degree of Doctor of Philosophy

---

Dr. M.J.D. Hayes  
Thesis Supervisor

---

Dr. J.M.J. McDill  
Thesis Supervisor

---

Dr. M.I. Yaras  
Chair, Department of  
Mechanical and Aerospace Engineering

Carleton University

May 7, 2010

## Abstract

The positioning accuracy and repeatability of a robot are critical for many industrial applications. Drift in repeatability can occur with changes in environmental and internal conditions, such as those seen with temperature-induced deformation. Thermal instability causes dimensional deformation, and a warm-up cycle is typically required to bring the robot to a thermally stable working condition. The elimination of warm-up cycles will ultimately enhance the positioning accuracy of the robots, their productivity, and reduce unnecessary energy consumption. The main objective of this research was to develop a robot controller algorithm that would provide, *a priori*, compensation for temperature-induced deformation associated with warm-up in robot mechanical systems. The research started at the fundamental stage of gaining insight into the thermal behaviour and corresponding temperature-induced deformation of simplified, *i.e.*, one-dimensional, robot mechanical systems consisting of slender links and heat sources. The systems were studied using concomitant experimental, numerical and analytical models to provide cross-checking of the results. For the experimental model, the deformation was measured by tracking the drift of a laser diode spot across a charge-coupled device (CCD) camera chip. A non-contact measurement system consisting of an infrared camera, a CCD camera and a laser diode was developed to provide high accuracy measurement for the deformation. The numerical model was generated with a coupled thermal-mechanical finite element analysis incorporating thermal effects due to conduction and convection. The models were tested with the analytical model that was further extended using a finite difference technique. Once the three models showed excellent agreement, it was possible to develop a controller algorithm. Deformations predicted by the finite difference model were used as input for a validation experiment of the compensation algorithm. Results of the validation experiment confirmed that temperature-induced deformation of the simplified robot mechanical system can be accurately compensated for using a simple algorithm implemented in a robot controller.

# Contents

<b>Acceptance</b>	<b>ii</b>
<b>Abstract</b>	<b>iii</b>
<b>Contents</b>	<b>iv</b>
<b>List of Tables</b>	<b>vi</b>
<b>List of Figures</b>	<b>vii</b>
<b>List of Symbols</b>	<b>viii</b>
<b>1 Introduction</b>	<b>1</b>
1.1 Background . . . . .	1
1.2 Significance of this Research . . . . .	4
1.3 Literature Review . . . . .	7
1.4 Conceptual Process . . . . .	19
1.5 Contributions to Knowledge . . . . .	24
1.6 Thesis Overview . . . . .	27
<b>2 Preliminary Proof-of-Concept Work</b>	<b>30</b>
2.1 Introduction . . . . .	30

2.2	Positioning Repeatability Experiment . . . . .	32
2.2.1	Experimental Apparatus . . . . .	33
2.2.2	Experimental Procedure . . . . .	38
2.2.3	Experimental Results . . . . .	39
2.2.4	Analytical Analysis . . . . .	42
2.2.5	Discussion . . . . .	48
2.3	Electron Probe Microanalysis (EPMA) . . . . .	50
2.3.1	Analysis Methods . . . . .	51
2.3.2	Results . . . . .	53
2.3.3	Discussion . . . . .	54
2.4	Next Steps . . . . .	55
<b>3</b>	<b>Single-Link Experiment</b>	<b>56</b>
3.1	Introduction . . . . .	56
3.2	Experimental Model . . . . .	57
3.2.1	Simplified Robot Mechanical System . . . . .	58
3.2.2	Optical Measurement System . . . . .	61
3.2.3	Software . . . . .	64
3.2.4	Procedure . . . . .	67
3.3	Analytical Model . . . . .	68
3.4	Numerical Model . . . . .	70
3.4.1	Material Properties . . . . .	72
3.4.2	Boundary Conditions . . . . .	72
3.5	Results and Discussion . . . . .	73
3.5.1	Stationary Case . . . . .	74
3.5.2	Moving Case . . . . .	76

<b>4</b>	<b>Measurement System Improvement</b>	<b>81</b>
4.1	Introduction . . . . .	81
4.2	Evaluation of the Experimental Models . . . . .	82
4.3	Effects of Cantilever Bending . . . . .	84
4.3.1	Analytical Analysis of the Effects of Cantilever Bending . . . . .	84
4.3.2	Results and Discussion . . . . .	85
4.4	Effects of Link Alignment . . . . .	86
4.4.1	Analytical Analysis of the Effects of Link Alignment . . . . .	86
4.4.2	Results and Discussion . . . . .	90
4.5	Expansion of Diode Hole . . . . .	91
4.5.1	Analytical Analysis of Diode Hole Expansion . . . . .	92
4.5.2	Numerical Analysis of Diode Hole Expansion . . . . .	94
4.5.3	Results and Discussion . . . . .	95
4.6	Idle-Induced Robot Vibration . . . . .	99
4.6.1	Experimental Analysis of the Idle-Induced Robot Vibration . . . . .	100
4.6.2	Results and Discussion . . . . .	100
4.7	Effects of Accuracy of Laser Centroid Extraction Algorithm . . . . .	103
4.7.1	Laser Spot Size Adjustment . . . . .	104
4.7.2	Modification of the Laser Spot Geometric Centroid Extraction Algorithm . . . . .	105
4.7.3	Results and Discussion . . . . .	107
4.8	Thermal Effects of CCD Camera . . . . .	109
4.8.1	Experimental Analysis of the Thermal Effects of the CCD Camera . . . . .	110
4.8.2	Results and Discussion . . . . .	112
4.9	Heating Pad Flexibility . . . . .	115
4.9.1	Experimental Analysis . . . . .	116

4.9.2	Results and Discussion . . . . .	117
4.10	The Improved Deformation Measurement System . . . . .	118
4.11	Validation Experiment of the Improved Deformation Measurement System	118
<b>5</b>	<b>Two-Link Experiment</b>	<b>121</b>
5.1	Introduction . . . . .	121
5.2	Experimental Model . . . . .	122
5.2.1	Experimental Apparatus . . . . .	122
5.2.2	Experimental Procedure . . . . .	124
5.3	Finite Element Model . . . . .	124
5.3.1	Model Assembly . . . . .	125
5.3.2	Heating Pads . . . . .	125
5.3.3	Material Properties and Boundary Conditions . . . . .	125
5.4	Finite Difference Model . . . . .	127
5.4.1	Rule of Mixtures . . . . .	130
5.5	Results and Discussion . . . . .	131
5.5.1	Stationary Case . . . . .	133
5.5.2	Moving Case . . . . .	134
<b>6</b>	<b>Compensation Algorithm Concept Validation</b>	<b>137</b>
6.1	Introduction . . . . .	137
6.2	Experimental Concepts for Algorithm Validation . . . . .	138
6.3	Experimental Apparatus . . . . .	141
6.4	Compensation Process . . . . .	142
6.4.1	Finite Difference Model for Deformation . . . . .	143
6.4.2	Compensation Algorithm . . . . .	144
6.4.3	Incremental Location Command . . . . .	145

6.4.4	Absolute Location Command . . . . .	146
6.5	Experimental Results . . . . .	148
6.6	Statistical Analysis . . . . .	151
6.7	Discussion . . . . .	156
<b>7</b>	<b>Conclusions and Future Work</b>	<b>159</b>
7.1	Conclusions . . . . .	159
7.2	Future Work . . . . .	162
7.2.1	Compensation for Temperature-Induced Deformation . . . . .	162
7.2.2	Improvement of the Non-Contact Measurement System . . . . .	163
	<b>References</b>	<b>163</b>
	<b>Appendices</b>	<b>171</b>
<b>A</b>	<b>MATLAB Algorithms</b>	<b>171</b>
A.1	Laser Spot Centroid Extraction Algorithm . . . . .	171
A.2	Predictive Deformation Generations . . . . .	185
<b>B</b>	<b>LabView Virtual Instruments</b>	<b>187</b>
<b>C</b>	<b>Statistical Analysis from Validation Experiments</b>	<b>191</b>

# List of Tables

2.1	Coordinates of Cameras A and B CCD chip centres expressed in Frame $\{W\}$ .	36
2.2	Coordinates of tool flange centre coordinates for <i>Pose A</i> and <i>B</i> expressed in Frame $\{W\}$ .	36
2.3	Joint angles for <i>Poses A</i> and <i>B</i> .	38
2.4	$\Delta T$ and $\Delta l_x$ from estimation of positioning repeatability experiment.	42
2.5	KUKA KR-15/2 <i>effective</i> link lengths at $23 \pm 0.5^\circ\text{C}$ .	44
2.6	Linear coefficient of thermal expansion.	46
2.7	$\Delta l_x$ and prediction error.	48
2.8	Nominal composition by weight %.	54
3.1	Material properties.	72
3.2	Analytical and experimental total longitudinal deformation of stationary case.	75
3.3	Numerical and experimental longitudinal deformation of moving case.	78
4.1	Potential sources of error and types of available results.	83
4.2	Variation in link misalignment due to mechanical play.	91
4.3	Accuracy improvement due to idle-induced robot vibration.	102
4.4	Accuracy improvement due to centroid extraction algorithm.	109
4.5	Possible sources of error ranked by significance of effects on the deformation measurement system.	119

5.1	Parameters for finite difference model. . . . .	129
5.2	Material properties calculated using ROM. . . . .	131
6.1	Statistical results. . . . .	155
C.1	Intervals and frequency distribution of errors from incremental location com- mand. . . . .	191
C.2	Intervals and frequency distribution of errors from absolute location command.	192
C.3	Chi-squared test for errors from incremental location command. . . . .	192
C.4	Chi-squared test for errors from absolute location command. . . . .	193

# List of Figures

1.1	Schematic configuration of stimulated multi-station assembly operation experiment. . . . .	9
1.2	3-D fringe plot of deformation due to a temperature difference. . . . .	11
1.3	Structure of thermal actuators and sensor locations. . . . .	13
1.4	Structured light unit scanning a scene engaged by a robot. . . . .	15
1.5	OPTOTRAK LEDs mounted on a plate attached to the surgical probe. . .	16
1.6	Optical components of the laser tracking system. . . . .	17
1.7	Original conceptual process for compensating for temperature-induced deformation. . . . .	22
2.1	KUKA KR-15/2. . . . .	34
2.2	Reference coordinates for deformation measurement. . . . .	36
2.3	Camera placement and kinematic configuration for <i>Pose A</i> . . . . .	37
2.4	Thermal images of the robot at the start and end of Run 1. . . . .	39
2.5	Camera A raw image. . . . .	40
2.6	Laser spot centroid over time of <i>Poses A</i> and <i>B</i> for all runs. . . . .	41
2.7	Projected link length for <i>Pose A</i> . . . . .	44
3.1	Experimental apparatus. . . . .	58
3.2	Coupling and delrin disk. . . . .	60

3.3	Comparing experimental apparatus. . . . .	63
3.4	Flow diagram of image acquisition and robot motion control process. . . .	65
3.5	Sub-pixel coordinates. . . . .	67
3.6	Element assignment of single-link FEA model. . . . .	71
3.7	Temperature distribution at steady state of stationary case from experimen- tal model. . . . .	74
3.8	Temperature distribution and longitudinal deformation of stationary case. .	75
3.9	Temperature distribution at steady state of moving case. . . . .	77
3.10	Temperature of two node locations over 3,600 s of moving case. . . . .	78
3.11	Thermal distribution ( $^{\circ}\text{C}$ ) at steady state of moving case predicted by the FEA. . . . .	79
3.12	Longitudinal deformation ( $\times 100$ ) superimposed on undeformed link at steady state of moving case. . . . .	79
3.13	Longitudinal deformation of FEA and experimental results immediately above laser diode of moving case. . . . .	80
4.1	Static deformation. . . . .	85
4.2	$\delta L_x$ and $\delta L_y$ . . . . .	86
4.3	Link and axes definition. . . . .	87
4.4	Link alignment showing misalignment $\theta$ . . . . .	87
4.5	Actual and measured $\Delta L$ due to misalignment about $z$ -axis. . . . .	88
4.6	Link alignment showing misalignment $\beta$ . . . . .	89
4.7	$\Delta L$ and $\Delta L_x$ due to misalignment about $y$ -axis. . . . .	90
4.8	Link alignment about $x$ -axis. . . . .	90
4.9	Dimension of link at diode end. . . . .	93
4.10	Diode dropping straight down. . . . .	93
4.11	Diode tilting vertically. . . . .	94

4.12	Tilt angle, $\alpha$ , due to hole expansion. . . . .	96
4.13	$\delta L_x$ due to tilting of laser diode. . . . .	97
4.14	Temperature distribution ( $^{\circ}\text{C}$ ) at steady state from FEA of single-link model.	98
4.15	Temperature and deformation at node above laser diode. . . . .	98
4.16	Results of robot idle-induced experiment. . . . .	101
4.17	Images of laser spot acquired by CCD camera. . . . .	105
4.18	Results of laser spot size experiment. . . . .	108
4.19	Results of the laser spot size experiment before normalizing. . . . .	109
4.20	Heated CCD camera stand. . . . .	110
4.21	CCD Camera stand. . . . .	111
4.22	CCD camera stand assembly before and after the improvement. . . . .	112
4.23	Temperature results of thermal-effect experiment with no heat applied. . .	113
4.24	Deformation results of thermal-effect experiment. . . . .	115
4.25	Original heating pad assembled on shaft. . . . .	116
4.26	IR image of flexible heating pad when supplying heat to the single-link experimental model. . . . .	117
4.27	Improved deformation measurement system. . . . .	120
4.28	FEA and experimental deformation results of the moving case experiment using improved deformation measurement system. . . . .	120
5.1	Assembly of two-link system. . . . .	122
5.2	Slender links. . . . .	123
5.3	New names assigned for shafts and links. . . . .	123
5.4	Two-link FEA model with short shafts. . . . .	126
5.5	Nodal boundaries of two-link analytical model. . . . .	127
5.6	Temperature contour of the link overlapped area. . . . .	133

5.7	Longitudinal deformation from experimental, finite difference and FEA models. . . . .	134
5.8	Temperature results (°C) of moving case. . . . .	135
5.9	Longitudinal deformation of moving case. . . . .	136
6.1	Concept of compensation for deformation. . . . .	140
6.2	Laser diode holder. . . . .	141
6.3	Incremental location command. . . . .	146
6.4	Absolute location command. . . . .	147
6.5	Results of validation experiment using incremental location command. . . .	149
6.6	Results of verification experiment using absolute location command. . . . .	150
6.7	Comparison of compensation and error curves between incremental and absolute commands. . . . .	151
6.8	Histograms. . . . .	154
6.9	Deformation of compensated and uncompensated systems. . . . .	157
A.1	Location of laser spot centroids in $x$ - and $y$ - axes directions. . . . .	172
A.2	Intensity distribution of each laser spot image. . . . .	173
A.3	Maximum intensity of each laser spot image. . . . .	173
A.4	Locations of laser spot centroids required for compensation corresponding to the deformation. . . . .	185
B.1	Front panel of image acquisition and robot motion control process. . . . .	188
B.2	Front panel of compensation algorithm LabView virtual instrument. . . . .	189
B.3	Flow diagram of compensation algorithm. . . . .	190

## List of Symbols

$A$	Parameter of first-order exponential curve
$a$	Link thickness
$b$	Link thickness (area moment of inertia)
$b$	Laser diode hole radius
$C$	Thermal capacity
$C_1, C_2$	Centroid locations
$C$	Heat capacity
$c$	Laser diode diameter (Chapter 4)
$c$	Specific heat (Chapter 5)
$D_1, D_2$	Diameter locations
$E$	Young's Modulus
$F$	Force
$I$	Area moment of inertia
$I^P(i, j)$	Pixel intensity at coordinate $(i, j)$
$h$	Link width (area moment of inertia)
$i$	Laser spot image coordinate in $x$ direction
$j$	Laser spot image coordinate in $y$ direction
$K$	Number of intervals
$k$	Thermal conductivity
$L$	Length
$l$	Nominal link length
$l_2$	Effective distance between Axes 2 and 3 of the robot
$l_3$	Effective distance between Axes 3 and 5 of the robot
$m$	Number of statistical values used in computation

$N$	Sample size
$n_j$	Observed number of occurrences
$n'_j$	Predicted number of occurrences
$q$	Heat-transfer rate per unit time
$R$	Thermal resistance
$S_x$	Standard deviation
$S_{\bar{x}}$	Standard deviation of the mean
$t_e$	Elapsed time
$T$	Temperature
$T_i$	Initial temperature, $T(x, 0)$
$T_0$	Surface temperature, $T(0, t_e)$ for $t_e > 0$
$T(x, t_e)$	Temperature at any position, $x$ , as a function of time, $t_e$
$V$	Volume
$\{W\}$	World coordinate frame of the robot
$x, y, z$	Cartesian space coordinates
$x_i$	Sample (statistical analysis)
$\mathbf{x}$	Independent variable of first-order exponential curve
$\mathbf{y}$	Dependent variable of first-order exponential curve
$\mathbf{y}_0$	Value of $\mathbf{y}$ , when $\mathbf{x} = 0$
$\alpha$	Linear coefficient of thermal expansion
$\alpha_d$	Thermal diffusivity
$\alpha_A$	Apparent linear coefficient of thermal expansion computed from data of Camera A
$\alpha_B$	Apparent linear coefficient of thermal expansion computed from data of Camera B

$\alpha_{6061-T6}$	Average linear coefficient of thermal expansion of 6061-T6 aluminium alloy in the temperature range 20°C to 100°C
$\bar{\alpha}$	Average apparent linear coefficient of thermal expansion computed from data of Cameras A and B
$\beta$	Angle
$\gamma$	Angle
$\Delta L, \Delta l$	Change in length due to change in temperature
$\Delta l_x$	Component of the change in length due to change in temperature measured on the $x_w$ -axis of the world coordinate frame
$\Delta\tau$	Time increment
$\delta l$	Deformation caused by potential sources of error
$\theta$	Angle
$\vartheta$	Joint angles of robot
$\rho$	Density
$\sigma$	Standard deviation
$\tau$	Time constant (Chapter 2)
$\tau$	Time (Chapter 3)
$\nu$	Degree of freedom in the variance for data set
$\phi$	Angle
$\chi^2$	Chi-squared distribution

# Chapter 1

## Introduction

The principal goal of this thesis was to compensate for temperature-induced deformation associated with the warm-up needed when an industrial robot is not operated in a thermally stable condition. To put the original contributions of this thesis into the proper context, the following background material should first be discussed so that the necessary terms are defined and the concepts are outlined.

### 1.1 Background

An industrial robot is considered to be a general purpose, reprogrammable machine that sometimes possesses a number of anthropomorphic characteristics. Specifically, ISO 8373: Manipulating industrial robots - Vocabulary [1] defines an industrial robot as follows:

*A robot is an automatically controlled, reprogrammable multipurpose, manipulative machine with several reprogrammable axes, which may be either fixed in place or mobile for use in industrial automation applications.*

The ability of a robot to automatically position and orient its end-effector with both accuracy and repeatability according to stored commands is a key factor of industrial

robots in many industrial processes. Typical commercial applications for industrial robots, such as spot welding, spray painting, assembly, packaging, palletizing, etc., require that a variety of *taught* poses (positions and orientations of a coordinate reference frame that moves with the robot tool flange) be *repeatable*. A taught pose is one that the manipulator is moved to physically. The joint sensors are read and the corresponding angles stored. When the robot is commanded to return to that configuration from some other position, each joint is returned to the stored value. Thus, *repeatability* is a measure of how precisely a robot can return to a taught pose [2]. The robot repeatability has come to be the standard configuration performance indicator specified by manufacturers [3]. The repeatability is normally expressed as a dimension of length, typically as microns ( $\mu\text{m}$ ).

A robot can also be programmed, by other means external to the controller, to move to a position and orientation that it may never have attained before. In this case, repeatability alone is not a sufficient performance index, especially when the robot's tasks are guided by vision or other motion guidance systems external to that of the robot.

Accuracy is the industry-accepted performance index used to measure the ability of the robot to position the manipulator at a specific position in the reachable workspace<sup>1</sup>. The *accuracy* of the robot is the precision with which a computed pose can be attained [2]. The positioning accuracy is also normally expressed as a dimension of length. When required robot poses in Cartesian space (the task space) are computed off-line, external to the robot controller, the inverse kinematics of the device must be computed in order to solve for the required joint angles. If the goal position and orientation create a pose that the robot has never before attained, then a measure of repeatability is no longer sufficient to assess the precision of the computed pose; accuracy must now be considered. The inadequacy of repeatability in assessing pose precision is especially true when robotic metrology tasks are guided by systems external to that of the robot. Even if an application does not rely on

---

<sup>1</sup>The reachable workspace refers to the set of locations of the end-effector reference point that may be reached with at least one orientation (also called *maximal workspace*) [4].

the absolute accuracy of a robot, and instead uses only the accuracy of relative motion in restricted areas of the workspace, the repeatability represents the lower bound. However, the accuracy of a robot is typically an order of magnitude worse than its repeatability [5]. Thus, a ‘teach and playback’ method that mainly depends on repeatability of the robots, is popular with automotive manufacturers as it provides better performance than off-line programming. In practice, industrial robot manufacturers provide a vague quantification of repeatability and virtually ignore accuracy. For example, the repeatability of the KUKA KR-15/2 is given as  $\pm 100 \mu\text{m}$  [6], while that of the Thermo CRS A465 is  $\pm 50 \mu\text{m}$  [7], and in neither case the accuracy is specified.

In general, the specifications for repeatability are considered as vague because they are not defined with respect to other operating parameters such as environmental temperature, motor speeds and payload. Aluminum alloys are used for the bulk of the structural components of many robots. However, aluminum alloys undergo deformation due to changes in temperature, thereby inducing operation errors in the robot. As a result, long warm-up cycles are typically required to reach operational steady state. If the thermal response of the robot for specific cyclic tasks were known, the temperature-induced deformation could be predicted *a priori* and compensated for using a set of coefficients programmed into the controller. Corresponding warm-up and cool-down cycles could be eliminated. Hence, the drift of pose and orientation repeatability could also be eliminated.

Calibration adjustments are limited by the fact that accuracy can only be improved to the lower bound of repeatability. The absolute accuracy and repeatability of a robot can drift significantly depending on environmental and internal conditions, such as thermal expansion, gravity effects, manufacturing errors, dynamic characteristics, and system errors of the controller’s inverse kinematics algorithms [8, 9]. Hence, if the drift in positioning and orientation repeatability could be determined *a priori*, and accounted for, then calibration could potentially improve the accuracy to a new lower bound that is significantly

better value than the reported repeatability.

The motivation for the research presented in this thesis arises from the potential for increasing industrial robot workcell productivity while simultaneously eliminating warm-up times, and associated costs from loss in productivity. The long-term goal of this research is to eliminate the warm-up cycle times needed when an industrial robot is not operated in a thermally stable condition. A model-based control algorithm to compensate for the temperature-induced deformation associated with the warm-up period will be developed and a refined finite difference model will be used for motion control. For any given assigned trajectory and load, the control algorithm will relate robot geometry to temperature changes, material behaviour, and the contribution of each motor and gearbox.

## 1.2 Significance of this Research

Fluctuations in repeatability and accuracy arise mainly from temperature-induced deformations, responses to applied loads, dimensional errors, dynamic characteristics, and system errors of the controller inverse kinematics algorithms. Temperature-induced deformation appears to be particularly critical during the warm-up cycle [10].

Thermal instability, which causes the dimensional distortion, is induced by heat losses in the robot motors and gearboxes and typically requires a period of two hours of continuous motion through the workspace to establish steady state [11]. When an industrial robot at ambient temperature is powered up, a warm-up cycle may be required to bring the robot to a thermally stable working condition. Without such a warm-up cycle, temperature-induced dimensional distortion [10] may seriously affect the positioning and orientating capabilities of the robot. It has been reported [12] that in some applications, where a precise trajectory must be followed, a warm-up of as much as five hours may be required for a medium payload robot to reach steady state. Similarly, if a robot workcell

goes offline for any number of reasons, such as unexpected maintenance or material or tool changes, a short warm-up period will be required to restore a steady state condition. During this warm-up, the workcell has zero productivity. Such warm-up cycles carry with them a large cost on a production line and also represent a potential loss due to an unnecessary consumption of energy [13].

Repeatability is also affected by several design variables such as mechanical rigidity, link dimensions, joint encoder characteristics, gear backlash, gear train compliance, motor bearings and address resolution. Stresses, caused by sources such as moment of the inertia of the arm when it is carrying a load, and environmental variables, such as heat and humidity, can adversely affect the repeatability of the robot.

In ISO 9283: Manipulating industrial robots - Performance criteria and related test methods [11], one of the most-used standards among robot users, it is stated in *Section 6.2: Conditions Prior to Testing*, as follows:

*The test shall be preceded by an appropriate warm-up operation...*

This statement indicates that warm-up is required in order for the robot to perform at its expected capacity. However, the ISO statement also implies that warm-up cycle times may vary depending on the size, model and application of the robot. Hence, the appropriate warm-up cycle must be specified by manufacturers. Robot accuracy can be improved through calibration of the end-effector position up to the limit of repeatability. It has been shown that operating the robot in a thermal steady state improves its repeatability [10, 14], in turn potentially improving its accuracy.

The ability of a simple mathematical predictive model to accurately predict the deformation of a robot, demonstrated in the results of an estimation of positioning repeatability experiment presented in Section 2.2, suggests the possibility of an improvement in positioning accuracy and productivity of industrial robots. When a KUKA KR-15/2 robot is operated in a warmed-up condition (steady state), its repeatability is almost one order of

magnitude better than the catalogue-specified value; *i.e.*,  $\pm 20 \mu\text{m}$  instead of  $\pm 100 \mu\text{m}$  [5]. However, if the robot is operated starting from a cold state, the actual repeatability is substantially worse than the specified value; *i.e.*,  $\pm 140 \mu\text{m}$  as opposed to  $\pm 100 \mu\text{m}$ . Note that there is no mention of such thermal effects on robot performance in the literature supplied by the manufacturer for the KUKA KR-15/2 [6].

The elimination of drift of positioning repeatability not only has the potential to improve positioning accuracy and enhance the productivity of industrial robots allowing them to perform applications more precisely, but may also reduce overall energy consumption of the robots. The significance of reduction in unnecessary energy consumption is presented in the following energy case study [15]:

“Consider a modest assembly line of 15 small payload (15 kg) robots, each with an installed motor capacity (maximum energy consumption) of 3 kW. The average power consumption at average power usage of each robot is 1.2 to 1.5 kW [6, 16]. If the robots work continuously for three, eight-hour shifts each day (45 robot shifts) with an overall efficiency of 98% [13], then approximately one robot will be out of service for one shift each day. During the unloaded warm-up cycle approximately 1 kW is consumed. If a one-hour warm-up period is required, there will be an unnecessary energy consumption of 1 kWh each day or 365 kWh each year. This corresponds to two weeks of energy consumption for a typical North American family [17], or that of a small village of 40 for a year in the developing world [18]. However, for a line of 15 large payload robots, the unloaded consumption per robot is approximately 10 kW and the warm-up cycle time may be 3 to 5 hours [14]. In this case there is an unnecessary energy consumption of 18,250 kWh per year.

According to the Ontario Energy Board [19], the cost for non-residential con-

sumers is \$0.05/kWh (up to 750 kWh) and \$0.059/kWh for consumption exceeding 750 kWh. Therefore, energy wasted in the warm-up cycle for the hypothetical large payload robot line costs \$1,070. If a plant has multiple assembly lines or multiple facilities, the total cost will be that much greater. There is also the associated loss of production that occurs during the warm-up cycle. For high-performance production lines, the economic consequences of the wasted energy may become even more significant.”

### 1.3 Literature Review

The body of archival literature contains virtually no work that is directly related to compensation of temperature-induced deformation in a robotic system. This literature review is therefore comprised of studies that are relevant, but only partially related to the research pursued in this thesis. To identify a clear connection between each study and this thesis research, relevant articles are categorized into five topics: robot characteristics; robot calibration; temperature-induced deformation in parallel manipulators and robotic systems; compensation of temperature-induced deformation in machine tools and parallel manipulators; and experimental methods and measurement systems.

#### **Robot Characteristics: Specification and Evaluation**

It is well known that the specifications of robot parameters supplied by manufacturers are not always well defined, or in some cases, not given at all. For those important specifications associated with a robot manipulator, such as repeatability and accuracy, problems occur when these values are not defined with respect to other specified parameters such as velocity and payload [3]. Users cannot determine the expected specifications under different operational conditions, and therefore have difficulty in selecting the right

robot to suit their requirements. It was suggested in [20] that specifications provided by manufacturers were to be considered as average, or expected values, rather than values expected for best performance. The average and worst case repeatability can also be obtained through similar testing procedures to those of the average repeatability but the data must be collected at different locations in the workspace: at the mid range of the joint indices for an average repeatability, and at the limit of the joint indices for a worst case repeatability [21]. In [3], two identical robots were tested in order to evaluate their performance and the repeatability, obtained through statistical analysis, was compared. It was found that the performance and repeatability of a particular robot depended on actual operating conditions.

The importance of standardized evaluation methods for robot performance characteristics has been strongly emphasized among robotics researchers over the past three decades only [22]. A wide variety of performance characteristics is available (*e.g.*, accuracy, repeatability, stabilization time, position overshoot, cornering deviations, etc.), but robot repeatability is mainly used because of its fundamental importance to robot performance (regarding either on-line or off-line programming) and the simplicity of methods used to evaluate the repeatability, relative to other performance characteristics, such as accuracy. Many researchers have proposed standards for methods used for determining robot repeatability [3, 21]. The standards specify the methods of data collection, instrumentation, procedure, and data uncertainty analysis.

## **Robot Calibration: Improving Robot Accuracy through Robot Repeatability**

Robot calibration is another important aspect of applied robotics. Kinematic calibration methods are used to improve the accuracy of a robot up to the limit of its repeatability. In robot performance evaluation, experimental results become less significant, if not com-

pletely useless, without proper calibration. The goal of the improvement is to make the calibration as accurate and statistically robust as possible, at a reasonable cost. Ideally, a robot should have the ability to self-calibrate with minimal human involvement [23]. In this article Hollerbach and Wampler introduced a kinematic calibration index to categorize the measurement approaches. They found that the distinctions between the methods were often small and arbitrary.

There is a very broad spectrum of conceptual approaches proposing alternatives to calibration: namely, improving robot accuracy by improving robot repeatability. Two parameters that were found to have an effect on robot repeatability were speed and payload [20]. A simulated multi-station assembly operation was used in an experiment designed to study the effects of various combinations of speed and payload of the tool centre on robot repeatability. In Figure 1.1 the gripper of the robot handling a stylus is used together with a digitizing tablet to make coordinate measurements. The repeatability of

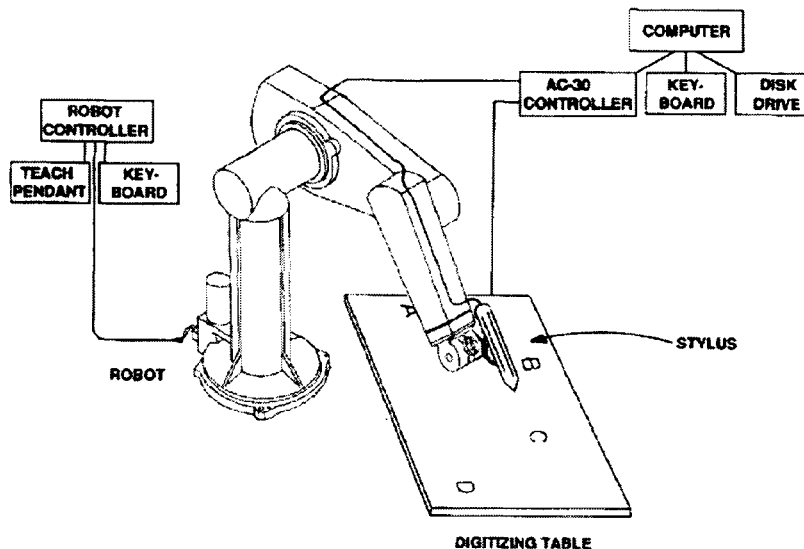


Figure 1.1: Schematic configuration of stimulated multi-station assembly operation experiment [20].

the robot deteriorated with an increase of tool speed and payload; *e.g.*, mass supported by

the end-effector. The range of speed used in the experiment was 5% – 50% of the robot's maximum speed (1 m/s), and the payload varied from 0.45 to 1.82 kg (1 to 4 lb). The manufacturer specified that the reported repeatability was achieved only when the robot was operated at 35% of its maximum speed, while carrying no payload. Interestingly, better values for repeatability than those specified by the manufacturer were obtained under various payload and speed conditions.

In studies of nanotechnology applications [8, 24], other parameters that were found to have effects on robot repeatability were thermal variation, gravity effects, and manufacturing errors. Numerical simulations conducted with *Ansys<sup>TM</sup>* and *ProEngineer<sup>TM</sup>* packages were used to examine inaccuracies in manipulators comprised of high precision co-operative robot systems. Figure 1.2 shows a 3-D fringe plot of deformation due to a change in temperature of a one-degree-of-freedom (1-DOF) robot obtained from a simulation conducted with *Ansys<sup>TM</sup>* [8]. The inaccuracies found in these cases were the results of all three parameters. The simulations in [8, 24] also showed that total deformation due to all above effects was not equal to the sum of the deformations due to the individual effects. The prediction of deformation is therefore more complicated than a simple superposition.

## **Temperature-Induced Deformation in Parallel Manipulators and Robotic Systems**

Many studies, such as [12, 25, 26, 27], have focused on the investigation and compensation of temperature-induced deformation. However, the majority of these studies have been focused on statistical analysis of data that was either based on, or directly provided by, the manufacturers of the robotic systems. A problem with this type of evaluation is that it does not take into account the actual operating conditions of the systems. Specifications provided by manufacturers are generally the best possible values obtained from a particular

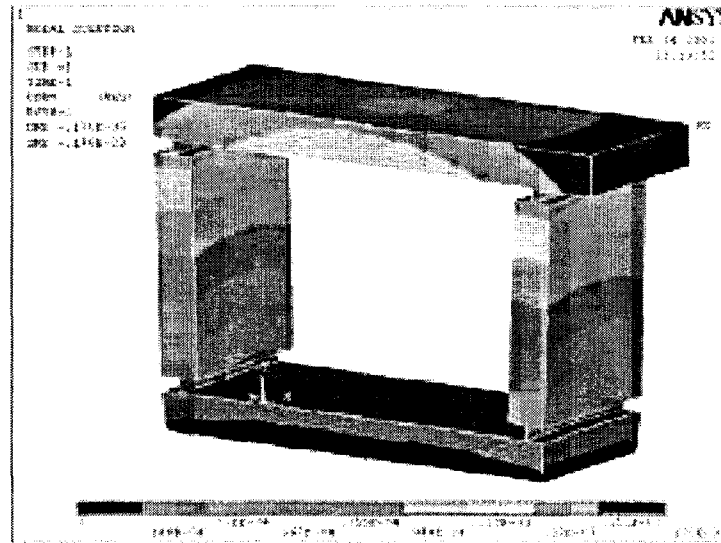


Figure 1.2: 3-D fringe plot of deformation due to a temperature difference of  $0.01^{\circ}\text{C}$  between a 1-DOF robot and the ambient temperature [8].

robot task based on a specific set of parameters at unknown, or at best vaguely defined, operating conditions.

For example, in [25], the geometric parameter errors, *i.e.*, joint states and link parameter errors, of serial link manipulators were estimated through a simple method that could be applied to any manipulator with any combination of revolute or prismatic joints. Manipulator biases were estimated and link error models were mathematically derived using Denavit-Hartenberg parameters. An implicit loop method for kinematic calibration was introduced in [26]. This method allowed errors to enter the kinematic loop equation implicitly, rather than just being explicit outputs as in a conventional input-output formulation. The article presented a successful kinematic calibration of a 6-DOF hand controller (joystick) and a modified Stewart Platform.

In an attempt to provide correction of temperature-induced deformation in [27], a ‘simple type concept’ approach of control integrated correction was utilized. A specific manipulator was developed and used in the correction of motion error in a parallel kine-

matic machine caused mainly by temperature. Results from experimental and numerical models showed sufficient compensation for the thermal load was provided.

Furthermore, techniques of real-time compensation for temperature-induced deformation in coordinate measurement machines and a series of machining systems were claimed to be successful in [12]. However, each study that yielded successful results required a complex system to compensate for the deformation. The practicality of solutions proposed in these studies as generic solutions is questionable due to constraints of each system specifically designed for a particular parallel kinematic machine.

## **Compensation of Temperature-Induced Deformation in Machine Tools and Parallel Manipulators**

Several studies demonstrate some successful results, or the promise of success of their future work for solving this temperature-induced deformation problem. For example, in [28], an active control system using thermal actuation was implemented on a machining centre in an attempt to compensate for temperature-induced distortion. The monitoring system consisted of force, vision, acoustic and deformation sensors. The real-time deformation compensation was done using column thermal actuators (as shown in Figure 1.3) comprising electric heaters and cooling jackets on the outer and inner surface of the actuator, respectively. The position of the spindle was maintained within  $10\ \mu\text{m}$ , as opposed to approximately  $30\ \mu\text{m}$  in the uncompensated system. The reduction of the deviation of the spindle indicated the level of effectiveness of the system.

However, the success reported in [28] does not provide methods applicable to a compensation method for articulated industrial robots. Despite the fact that the kinematics of machine tools and articulated industrial robots are based on the same theory, these two types of manipulators are very different in the nature of their application and in their corresponding motions. Machine tools are heavy but generally relatively precise, as they

have fewer joints and movable parts than articulated industrial robots, and have a very low payload-to-weight ratio. Machine tools mainly deform at spindles where heat is created by the cutting process [28], while articulated robots deform at links near motors that provide torque during the working process. Therefore, solutions that work for a deformation problem in a machine tool may not apply to the same problem for articulated industrial robots.

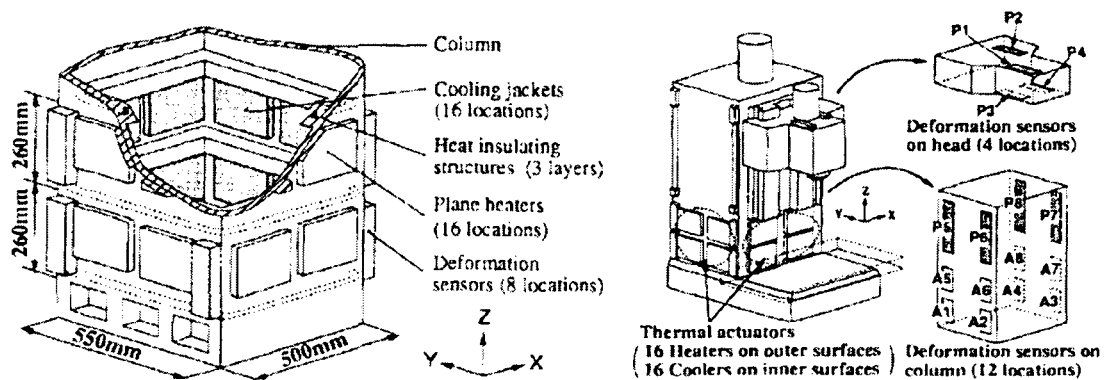


Figure 1.3: Structure of thermal actuators and sensor locations [28].

There appears to be little archival literature investigating the contribution of temperature-induced dimensional deformation in the kinematic geometry of serial robot mechanical systems with the exception of the studies reported in [5, 10, 12, 14, 15, 29, 30].

Gong, Yuan and Ni [12] investigated the effects of errors induced by temperature variation on robot positioning accuracy. The effects of the time-variant thermal errors were incorporated as part of the comprehensive error model, together with the effects from geometric errors and position-dependent compliance errors. Real-time calibration was provided for a 6-DOF industrial robot through a system consisting of a laser tracker, a temperature acquisition system, and a personal computer. Temperature variation along the robot arm was monitored with twelve thermistor sensors. Robot parameters were correlated with the temperature field using empirical temperature-induced error models generated using orthogonal regression methods. The possibility of building the models

into the controller to provide compensation to the robot was mentioned, however, the actual method of providing compensation in this particular experiment was not described. The mean residual errors were approximately ten times smaller than those of the system without the compensation.

In [5, 14], the researchers studied the warm-up and cool-down behaviour of a large industrial robot. In particular, thermal behaviour was observed as the robot repeated sequential motions at different speeds. Repeatability of the robot was then estimated accordingly. Significant drift of pose repeatability was detected, which implied the existence of deformation in robot geometry. If the drift in pose repeatability can be compensated for during operation of the robot then repeatability is essentially improved. The improved repeatability through compensation, in turn, implies that greater accuracy can be achieved through calibration.

The remaining available literature reports results by the author of this thesis [10, 15, 29, 30]. For example, in [10], the temperature-induced deformation in a simplified robot mechanical system was analyzed using experimental, numerical and analytical models. Good agreement in the results of temperature distributions and temperature-induced deformations obtained suggested the potential for the development of a predictive control algorithm to compensate for the deformation. The study presented in [10] will be fully discussed in Chapter 3.

## **Experimental Method and Measurement Systems**

Many studies [14, 31, 32, 33, 34, 35, 36, 37, 38, 39], although not directly related to temperature-induced dimensional deformation of robot mechanical systems, present experimental methods using contactless dimensional measurement systems and information extraction methods. The studies presented in [14, 31, 32, 33, 34, 39] demonstrate the success of the contactless dimensional measurement systems in a variety of applications.

The systems presented in [14, 34, 39] have become the foundation for the measurement system used in the experimental work reported in this thesis as presented at the end of this section.

A structured light scanner was used for 3-D robot vision in [31]. The structured light unit employed a light plane projected onto a scene and a camera. This portable unit was used by a robot for 3-D vision data collection, as illustrated in Figure 1.4. The intersection of a plane of light and a scanned object created a stripe of illuminated points on the object surface, which were recorded in the camera image plane. The importance of robot calibration was emphasized as a critical step toward the calibration of the scanner.

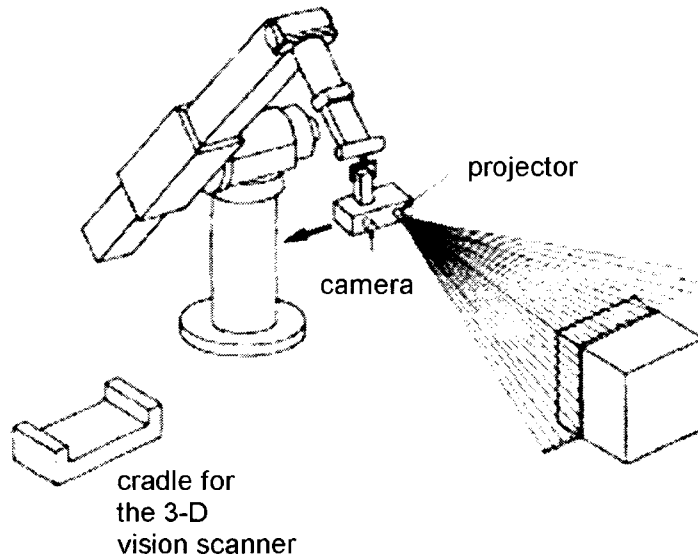


Figure 1.4: Structured light unit scanning a scene engaged by a robot [31].

A study intended for computer-assisted-image-guided neurosurgery compared the accuracy of a mechanically linked pointing device (FARO surgical arm) to an optical position tracker (OPTOTRAK) against a third measurement of a block with precision drilled holes [32]. The OPTOTRAK consisted of three charge-coupled device (CCD) cameras at fixed locations tracking light emitting diodes (LEDs) mounted on a probe attached to the end of the FARO surgical arm, as shown in Figure 1.5. The centroids of the LEDs were

calculated and used for determining the position of the probe tip in the OPTOTRAK frame. The accuracy of each system was determined by the mean of the norms of the measured vectors between holes relative to the precision of the milling machine used for drilling holes on the reference block. The results showed that slightly higher accuracy was obtained by the OPTOTRAK system. As reported in [32] other similar independent experiments were conducted using a larger six LED digitizer probe, and that the level of accuracy of the measurement system was found to be similar to that of the OPTOTRAK. The main conclusion was that the accuracy of the contactless optical system was superior to that of the mechanical system. Largely because of the results presented in this study [32], an optical contactless measurement system was created to record deformation data for the experiments reported in [34] and [39], which are the foundation of the deformation measurement system used in this thesis. The setup of the deformation measurement system of this thesis that was adjusted to suit the experimental setup and the requirements of the analysis are reported in Section 3.2.3.

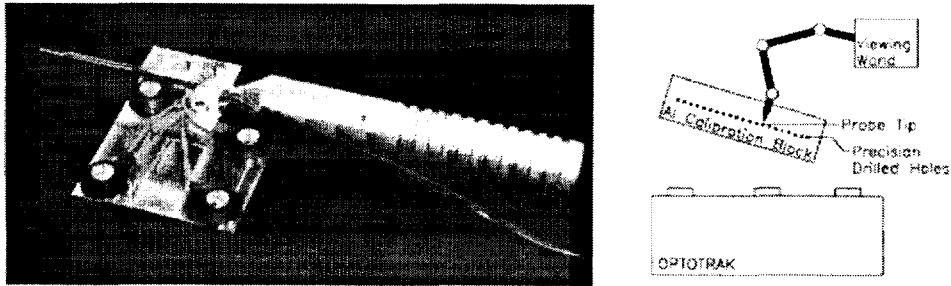


Figure 1.5: OPTOTRAK LEDs mounted on a plate attached to the surgical probe and overview of the measurement apparatus [32].

Contactless dimensional measurement systems using laser diodes and CCD cameras have been proven to be successful [14, 31, 32, 33, 34, 39]. A laser tracking system using a high-speed HeNe laser-interferometer was presented in [33]. In this system, a CCD camera takes images of a laser beam reflected by a set of three perpendicularly oriented plane mirrors. At the start of each measurement, the laser beam was set to hit the centre

point of the retroreflector, which is mounted on the end effector of the robot, causing no parallel displacement between the emitted and the reflected beams. A close-up view of the optical system is shown in Figure 1.6. When the robot started moving and the laser beam no longer pointed at the centre, the displacement due to robot motion was detected. This contactless system was able to dynamically measure all three positions and three orientation components without contacting the robot. The system, which processes automatically in real time within a large working area, also enabled most of the accuracy-repeatability characteristic measurements proposed in ISO 9283 [11].

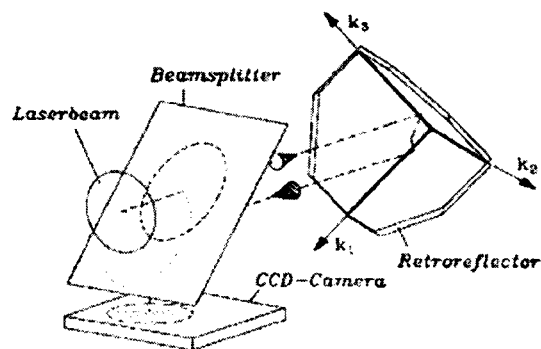


Figure 1.6: Optical components of the laser tracking system [33].

The major disadvantage of a dimensional measurement system that uses interferometers, such as Vince's [33], is the cost. The cost of a typical interferometer varies between \$15,000 and \$150,000 depending on the magnification of the interferometer [35, 36], and three interferometers would be required for a 3-D measurement system. The complex electronic hardware required for real-time signal processing, the sophistication of the system, and the difficulty in maintaining system calibration, all contribute to its cost [37, 38].

The deformation measurement system developed for this thesis provides the real-time measurements required for the compensation at a relatively low cost (less than \$2,500 for the complete system). Moreover, the required components are simple and accessible, and are available in most measurement laboratories. The development of the deformation

measurement system for this thesis is described in Section 3.2.2.

An application of a contactless dimensional measurement systems to kinematic calibration is presented in [39]. This study presented a calibration scheme for a manipulator based on relative measurements. Kinematic calibration is required to ensure accurate off-line programmed positioning of industrial robots, up to their repeatability. In the development of the experimental verification of the kinematic calibration procedure, measurement data were obtained by computing the difference between actual robot positions and the commanded robot positions with respect to a defined reference position. A CCD camera was rigidly mounted to a Thermo CRS A465 robot, and the metric information was extracted from sequential camera images of a precision-ruled straight edge.

In [34], an algorithm for extracting accurate metric information from images of a measurement artifact was developed during the determination of positioning error measurements required for robot calibration. The measurement system consisted of a camera and lens that were mounted to the robot using a stainless steel measurement head. The reference artifact was a thin block of aluminum. The pattern on the artifact consisted of a set of intersecting perpendicular grooves partially filled with black enamel paint so as to provide sharp contrast between the grooves and surface of the artifact. After the image was captured at the initial position of the robot, the robot moved through a series of motions and then attempted to return to the initial position where another image was captured. Differences between subsequent images indicated the positional error that the manipulator had produced while attempting to return to the original pose.

Both studies, presented in [34] and [39], were conducted at the same robotics laboratory at Carleton University as that currently used for the experimental work reported in this thesis. The foundation for the experimental setup and the method of extracting information from laser spot images taken by a CCD camera is built on the techniques revealed in these articles.

## 1.4 Conceptual Process

The long-term goal of this research was to develop a robot control algorithm that would provide, *a priori*, compensation for temperature-induced deformation associated with transient warm-up temperature changes. It was expected that as a minimum, the coefficient of thermal expansion for each link of the robot, taking into account the contribution of each motor and gearbox for a particular motion, could be determined. Through modification of coefficients programmed in the controller, warm-up and cool-down cycles could be eliminated thereby significantly enhancing the productivity of the robot.

Results from the estimation of a positioning repeatability experiment (see Section 2.2), and the proof-of-concept experiment conducted prior to the beginning of this research, suggested that thermal imaging provides useful data for extraction of changes in temperature of a target system. It was additionally expected that results of this research could be further studied and applied to a practical approach to compensation for temperature-induced deformation in an actual industrial robot. A Thermo CRS A465 small payload robot was used for the experiments reported in this thesis. The original conceptual process for compensating for temperature-induced deformation is described below:

**Step 1: Define parameters.** For a given task assigned to an industrial robot, parameters relating to the desired operating condition, such as trajectory, speed and load can be obtained. These parameters can then be specified for the motor work calculation in the next step.

**Step 2: Calculate work and losses.** From the information obtained from the assigned task, work required by each motor can be computed. Using the efficiency of the motors, either given by the manufacturer or obtained through experiments, the losses at each motor can be computed and the resulting heat that will be conducted to the linkages and convected into the environment can also be computed.

When the robot is accessible, Step 1 and Step 2 may be replaced by computation of heat losses corresponding to the actual measured temperatures of the robot links.

**Step 3: Identify material(s).** The materials comprising the bulk of the robot arm can be identified. The corresponding material properties of any given material, at room temperature, can be obtained from relevant handbooks.

**Step 4: Calculate temperature-induced deformation.** The temperature-induced deformation of each link of the robot, due to the heat loss from each motor, can be calculated. The deformation can be calculated using a linear coefficient of thermal expansion, the geometry of the linkage, material properties and boundary conditions. The total deformation, due to all of the links, measured at the tool frame can then be computed. The transient state deformation data can be obtained as a function of time and can be used for the compensation calculations in the next step. The results can be obtained via concomitant analytical and numerical models.

**Step 5: Calculate compensated path motion.** The temperature-induced deformation can be compensated for by requesting that the robot end effector move in the direction such that the tool frame should remain at the operational goal at all times. For example, for deformation occurred in the  $x$ -axis direction, the robot will be commanded to move in the negative  $x$ -axis direction by the same amount. For the best possible results, compensation should be provided with adequate time step resolution throughout the transient state until the deformation stops as the robot reaches a thermally stable state. The input motion of the robot is a function based solely on the total deformation over time obtained from the calculation in the previous step.

**Step 6: Generate coefficients.** Based on the motions required to compensate for the deformation, a set of coefficients can be obtained and provided to a robot controller. For a given task, such coefficients incorporate the deformation that occurred at each

link at a given time into the kinematic solution, and therefore the compensation will be automatically integrated into all joint commands (*i.e.* joint angles at a given time). The automatic integration of the compensation allows the tool frame of the robot to consistently return to the same goal point. Therefore, joint angle values fed to the controller will be different from resultant angles obtained from the inverse kinematics of the trajectory. The coefficients will vary over the transient state and relate directly to the deformation as a function of time.

The flowchart of the original conceptual process for compensating temperature-induced deformation is presented in Figure 1.7.

The original conceptual process could not be completed exactly as planned for several reasons. The ideal steps cannot be accomplished directly due to characteristics of the A465 robot. The motors of the A465 were small relative to the KUKA KR-15/2 robot used in the estimation of the positioning repeatability experiment [14]. Heat losses generated by the motors were not high enough to make the total deformation sufficiently large to be measured accurately with the contactless measurement system built at the lab. Also, during an attempt to develop analytical and numerical models of the A465 robot, it was discovered that a 3-D model was too complicated for either analytical or numerical analyses at this early stage. 3-D heat transfer analysis for a complex model required better understanding of the properties of the system (*i.e.*, the A465 robot), as well as its thermal behaviour with respect to a given set of boundary conditions. Hence, the objectives of this thesis were modified so as to lead to better understanding of the highly coupled fundamental principles involved.

To gain fundamental understanding and insight of temperature-induced deformation in a robot mechanical system, a simplified robot mechanical system was developed. First, a single slender link and a single heat source representing a servo motor similar to those used in small payload industrial robots were considered for a study of 1-D deformation. A link

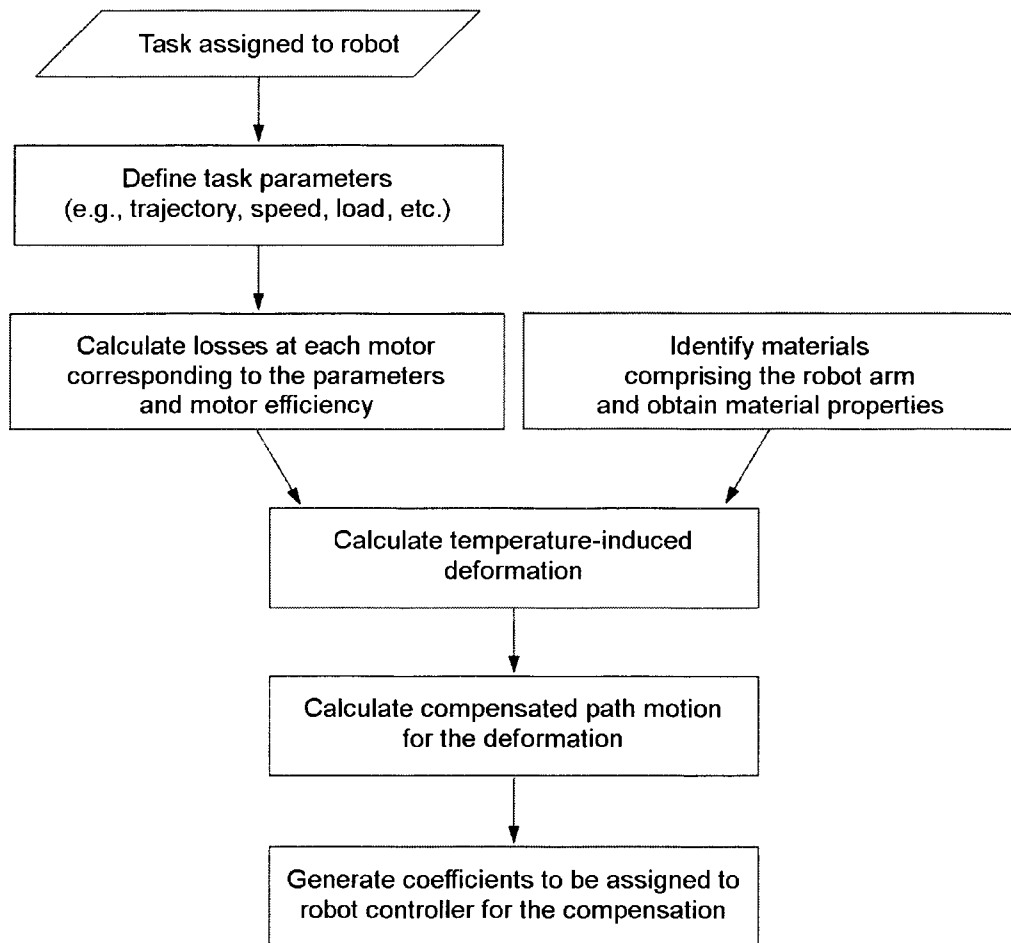
**Conceptual process for compensating temperature-induced deformation**

Figure 1.7: Original conceptual process for compensating for temperature-induced deformation.

was designed to be slender with one end fixed to the heat source and the other end free to expand, so that the total deformation was the deformation of the link in the longitudinal direction. In order to obtain accurate results from this experiment, the experimental model and measurement system needed to be carefully planned and implemented. A user-interface system was developed to integrate and synchronize the measurement systems, for both temperature and deformation, with the robot controller. Additional software was developed to extract deformation results from CCD images.

Analytical models were created based on a semi-infinite heat transfer model, while numerical models were generated with a coupled thermal-mechanical finite element analysis (FEA). The experimental, analytical and numerical models were used concomitantly. However, it was understood that none of the models alone would yield absolutely accurate deformation results of the simplified robot mechanical system. The accuracy of the deformation results obtained from the numerical and analytical models was affected by boundary conditions used in the models that might not match the real conditions, and/or material properties that could be different from the real properties. The simplification of the model from a 3-D system to a 1-D analytical model could also contribute to the error. Although the experimental model was created to represent an actual robot mechanical system, the model was only an attempt to mimic the behaviour of an industrial robot using a simpler system, which was therefore also prone to error, but error that could be fully characterized, and used as a foundation upon which to build.

After a single-link system was completely understood, the multiple-link system was studied for further understanding of a more complex system. The system consisted of two links and two heat sources. One link has both ends attached to each shaft, and the other link has one free end similar to the single-link system. The main focus of the multiple-link system was on temperature distribution and the corresponding deformation of the link that had the heat sources attached at each end. The analytical model of the single-link system was extended for the multiple-link system using finite difference method. The FEA model was developed in a similar manner done for the single-link system.

The next major hurdle came from a lack of access to the robot controller. The C500C controller used for the communication with the A465 robot was inaccessible. The original plan of integrating a set of coefficients directly into the controller, then, became impossible. To address this, stand-alone software was developed to pre-process the trajectory. To allow for the verification of the compensation in this particular case, the compensation had to be

done through a series of input commands. The validation experiment used the deformation as a function of time obtained in the two-link experiment as an input. Through empirical analysis, the path and speed of a robot tool frame were required to allow this compensation to be implemented. The input commands were directly entered into the controller of the A465 robot used in the experiment.

## 1.5 Contributions to Knowledge

### Major Contributions

#### 1. Compensation of temperature-induced deformation in industrial robots.

The success of the proof-of-concept experiments reported in Chapter 2 whereby temperature-induced deformation in a simplified robot mechanical system is compensated, suggests that the warm-up cycle in industrial robots may be eliminated or substantially reduced. The successful elimination of warm-up cycles stands to improve the productivity, energy consumption and overall quality of industrial robots.

##### **a. Improvement of robot workcell productivity and energy consumption.**

The warm-up cycle time carries with it a substantial cost on any production line. During the warm-up the workcell had zero productivity. Hence, elimination of the warm-up cycle is a potential solution for enhancing workcell productivity, as the robot can perform productive work during the warm-up cycles. The warm-up times and associated costs are then eliminated simultaneously from production schedules, thereby increasing productivity and reducing unnecessary energy consumption. Certain aspects of these novel results have appeared in [15].

**b. Improvement of industrial overall robot quality.**

With a sufficiently accurate predictive model incorporated into the control software, the repeatability of the robot, which is the lower bound of its accuracy, could be effectively improved. The improvement potential suggests that greater positioning accuracy can be achieved with the use of the predictive model rather than through calibration alone. By extension, the concept of a predictive model implies that the use of a control algorithm to compensate for temperature-induced deformation can increase the overall quality of the robot without increasing its cost. Certain aspects of these results have appeared in [10, 29].

**2. Development of a novel non-contact measurement system.**

A further significant contribution resulting from the experimental portion of this research was the development and refinement of a novel non-contact measurement system. The system, used to experimentally determine temperature-induced deformation, worked in concert with predictive thermal-mechanical FEA and a finite difference model. All three methods provided concomitant dimension estimates which were used to compensate for the joint angles computed by the robot controller using its constant nominal dimensions. With some additional development, the system would have the ability to perform non-contact measurement of temperature-induced deformation in three dimensions and could also be applied to a wide variety of other electro-mechanical devices.

**Minor Contributions**

To gain sufficient understanding of deformation measurement error, the potential sources of error were investigated during the development work on the experiment design. Several challenges were overcome, most notably errors caused by thermal effects of the CCD

camera and errors in calculating the pixel moments. Understanding and quantifying these errors led to significant improvements when applied to the experimental model. These improvements enhance the accuracy of the measurement results reported in this thesis, and additionally enhanced overall performance of each individual component.

### **1. Improvement of deformation measurement system using CCD camera.**

When a CCD camera acquires images, heat generated by the CCD camera is transferred to a camera mounting plate. The thermal expansion occurring at the mounting plate, in turn, alters the measurements made with the CCD camera. Therefore, when the camera is used to measure temperature-induced deformation to sub-pixel accuracy, the thermal effects must be considered. Heat fins were used to allow heat generated by the camera during the working period to be dissipated faster. The use of heat fins was found to be an effective method, especially when used in concert with a procedure of warming-up the camera prior to the start of a measurement.

### **2. Improvement of laser spot centroid extraction algorithm.**

A two-moment algorithm was used to extract the location of the geometric centre of the laser spot to sub-pixel accuracy. The algorithm was improved by the use of a threshold value that allows the lowest intensity value to be set for each image. The threshold value filtered out low intensity pixels, which generally appeared around the edge of the laser spot and were inconsistent in both location and intensity. These low intensity artifacts biased the centroid extraction. It was also discovered that a laser diode must be tuned so that the laser spot has large size with the sharpest edge possible appearing in the image. An increase in size of the laser spot increased the numbers of high intensity pixels, and thereby improved the accuracy of the coordinates of the geometric centre extracted from the image.

### 3. Improvement of LabVIEW virtual instrument.

The original LabVIEW virtual instrument developed in [39] was designed for communication between a development computer, a robot controller and a CCD camera. New features were incorporated to facilitate communication between the development computer and the infrared camera used to acquire change in temperature data. Deformation and temperature results can now be obtained simultaneously and automatically. The current version of the virtual instrument is also implemented with a deformation computation module that computes deformation of a two-link robot mechanical system and provides corresponding compensation motion commands to the robot controller. Certain aspects of these contributions are reported in [30].

## 1.6 Thesis Overview

Preliminary work is described in Chapter 2. First, the estimation of the positioning repeatability experiment is discussed. This experiment introduced a high accuracy non-contact measurement system for measuring deformation and temperature. The experimental results were analyzed and compared to the analytical results. Good agreement of the two results, which positively confirmed the concept of the predictive model, was found. The second part of the preliminary work presented was the electron probe microanalysis (EPMA). Characteristic analyses, in both qualitative and quantitative methods, were performed to obtain the composition of the material comprising the bulk of the robot arm. The composition of the specimen obtained from the robot arm was analyzed and compared to the reference specimen of a known aluminum type that was then used in the analytical analysis of the estimation of positioning repeatability experiment according to the material type identified.

Chapter 3 presents the development of a simplified robot mechanical system consisting

of only one link and one motor. The deformation of this system was limited to one dimension. A new non-contact measurement system, similar to that used in the estimation of positioning repeatability experiment was also developed. A combination of simplified experimental, numerical (FEA), and analytical models was utilized to allow cross-calibration and checking of the experimental, numerical and analytical results. A model developed in ABAQUS, an FEA software package, was used for coupled thermal-mechanical numerical analysis. A semi-infinite heat transfer equation was used in the analytical model. Two different experiments were performed, one with a stationary link and another with the link moving in reciprocating motion. Results from the experimental and the corresponding analytical and numerical models are presented. The results showed that it was possible to develop a simple predictive algorithm.

Although the results of the single-link experiment showed good agreement among the experimental, analytical and numerical models, there existed some unexplained differences among the results. It was unclear which model caused the difference, however several aspects of the experimental model were suspected to be potential sources of error. The modifications of the experimental model of the single-link experiment are presented in Chapter 4. Several potential sources of error were identified and are presented with details of the corresponding theoretical or experimental investigation and its results. Some sources were shown to be insignificant, but addressing others provided significant improvement in the accuracy of the results of the experiments and were permanently implemented in the experimental model. The completely modified experimental model provided much closer results to the numerical results, and would be used for the two-link experiment described in Chapter 5.

In Chapter 5, a two-link experiment is presented. Similar to the single-link experiment, experimental, FEA and finite difference models were developed. The finite difference model was developed based on the analytical model of the single-link and the concepts of thermal

resistance and capacitance [40]. Parametric studies were performed using the ABAQUS FEA model for a better understanding of the material properties and thermal boundary conditions. The two-link numerical model was also developed in ABAQUS. The results showed very good agreement among all three models.

The validation experiment of the compensation algorithm concept is described in Chapter 6. The robot was given the input data of the deformation results obtained in the two-link experiment, and provided a displacement to compensate for the temperature-induced deformation. With the limited accuracy of the robot, the total deformation was scaled up before being provided to the robot for this experiment. The results yield a constant position of the laser diode from start to finish, indicating successful compensation for the temperature-induced deformation of the system.

Finally, Chapter 7 presents conclusions and suggestions for future work. Two main topics of the future work include work related to the compensation of the temperature-induced deformation in robot mechanical systems, and work related to an improvement of the non-contact measurement system.

# Chapter 2

## Preliminary Proof-of-Concept Work

### 2.1 Introduction

As there exists little archival literature studying the effects of temperature-induced deformation in robot kinematic geometry during warm-up, it was necessary to verify the feasibility of predicting and compensating for the deformation in practice. To accurately compensate for the temperature-induced deformation of a robot mechanical system, the deformation must first be carefully estimated. The accuracy of the estimate depends on the physical parameters of the system and the method used to make the estimate. For verification of the estimate, several concomitant methods should be considered.

Work conducted prior to this research, involved a positioning repeatability experiment [14]. Experimental results confirmed that it is possible to estimate the temperature-induced deformation empirically, and also to predict the steady state deformation using analytical and numerical methods. Comparing the deformation obtained from each of the three methods, the difference was found to be less than 5%<sup>1</sup> [41], which indicated good agreement of the results from all methods.

---

<sup>1</sup>A general 95% probability level is suggested for all uncertainty calculations and most engineers follow this rule for consistency [41].

The experimental results in [14] indicated that when a KUKA KR-15/2 robot was operated in a thermally stable condition (*i.e.*, warmed-up), the repeatability of the robot was nearly one order of magnitude better than the manufacturer's stated value of  $\pm 100 \mu\text{m}$ . If the transient drift, which occurs before the robot reached steady state, could be compensated during operation, then the overall repeatability would be improved. The improvement of robot repeatability, in turn, implied that greater accuracy could be achieved through calibration of; in this case, the end-effector position. Although the results did not show any sign of significant error, the actual type of material comprising the KUKA robot arm had never been verified. Therefore, it was possible that the type of material assumed for the analysis was not the same as that of the actual robot arm. Normally, in this temperature range, the coefficient of thermal expansion of materials typically used in robot construction; *e.g.*, aluminum, were well defined and stable.

The proof-of-concept work was required to verify the appropriateness of the deformation and temperature measurement systems, and to identify any immediate concerns. This was done with the positioning repeatability experiment, which is discussed in detail in Section 2.2. The measurement system and procedures of the experiment, which are the fundamental model for the measurement system and experimental procedures used in this thesis research, are described. The apparent temperature and deformation results from the experiment are presented, and used analytically to estimate the coefficient of thermal expansion of the material comprising the robot used in the experiment. The coefficients are, in turn, used to compute subsequent deformation of the robot. The deformation obtained from the computation is compared to that measured from the experiment for verification of the results.

To address the uncertainty in the composition of the material in the robot arm, a material analysis was performed on the Thermo CRS A465 robot used in this thesis. In Section 2.3, the electron probe microanalyses of sample specimens of the robot arm

and a known 6061 aluminum alloy (further referred to as 6061 Al) are presented. The composition of this alloy was compared to the values listed in [42] to ensure an accurate reference. By comparing the detailed composition of a sample piece from the robot with the alloy standard, the specific aluminum alloy was determined.

## 2.2 Positioning Repeatability Experiment

The goal of the experiment presented in [14] was to obtain an estimate of the positioning repeatability of a KUKA KR-15/2 robot. The work in [14] presented a starting point for a proof-of-concept experiment on drift in positioning repeatability that helped to further develop an understanding of the thermally-induced dimensional changes. The drift in positioning repeatability caused by heat transferred to the links via losses in the motors and gearboxes was studied. In the experiment, the warm-up and cool-down behaviour of the robot was measured and its effect on the robot repeatability was examined. The temperature distribution history of the robot during the motion sequence was recorded with a thermal imaging camera. Temperature-induced robot dimensional changes (*i.e.*, deformation) were estimated from the geometry of the camera positions, and from the migration of a laser spot across a CCD chip of a CCD camera over time, from the start to the end of the thermal cycle (*i.e.*, when the deformation results indicated the thermal steady state of the robot). The results revealed that the overall positioning repeatability of the robot when operated in thermal steady-state was 80% better than the manufacturer-stated value, while it was 40% worse than that of the manufacturer-stated value when operated outside thermal steady-state.

### 2.2.1 Experimental Apparatus

The experimental apparatus of the positioning repeatability experiment in [14] consisted of two main components: an industrial robot and an optical measurement system. The measurement system consisted of two subsystems, one for temperature measurement and the other for deformation measurement. Information about the robot, the temperature measurement system and the deformation measurement system are presented in the three following subsections.

#### KUKA KR-15/2 Robot

The robot used in the experiment was a KUKA KR-15/2, a wrist-partitioned robot with six actuated revolute axes. The axes, together with the base and tool reference coordinate frames, are illustrated in Figure 2.1. The robot's rated payload is 15 kg and the volume of its working envelope, using the wrist-centre (intersection of orthogonal axes 4, 5 and 6) as a reference point, is approximately 13.1 m<sup>3</sup>. The specification that is most related to this experiment is the manufacturer's stated repeatability [6]:

$$\text{repeatability} = \pm 100 \mu\text{m}.$$

It should be noted that the repeatability is stated without explicit consideration of the environmental operating conditions.

#### Optical Measurement System

Estimation of the drift in positioning repeatability, deformation and changes in temperature of the robot was the key information required for the analysis. While the total change in temperature in the expected range of 5°C to 20°C could be accurately measured by many relatively straightforward methods, such as using thermocouples or an infrared (IR) camera, this was not the case for the dimensional deformation. The deformation was

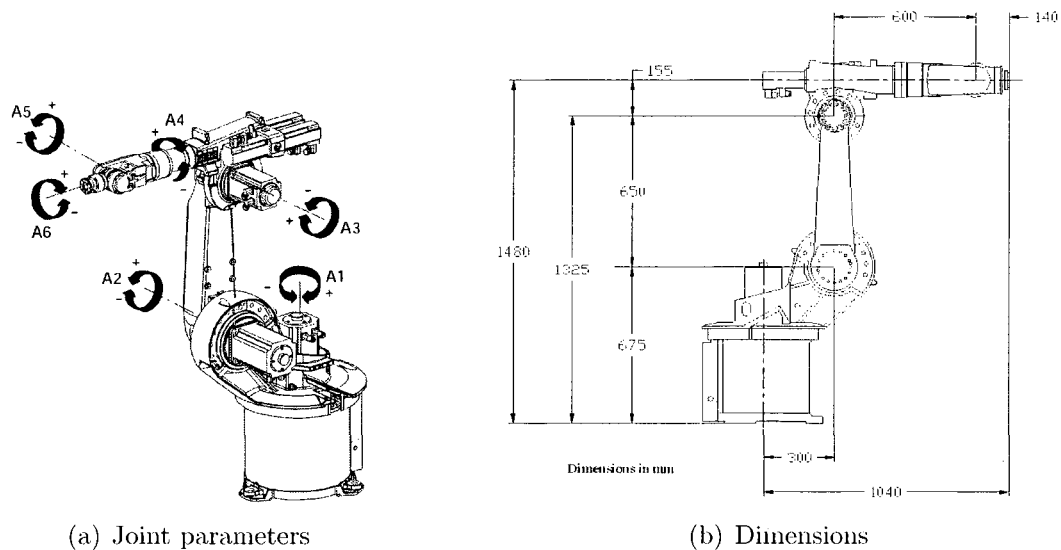


Figure 2.1: KUKA KR-15/2.

expected to be in the range of  $10^{-6}$  m, as approximated using the following simple case study:

The length of the longest link of KUKA robots of small payload (maximum 5 kg) varies from 0.36 m to 0.46 m [43]. If an average temperature rise due to the heat from the motor is  $5^{\circ}\text{C}$  and the material is a typical aluminum alloy, the deformation of the robot link due to temperature rise can be as small as  $40\ \mu\text{m}$ .

To measure such small deformation, the measurement system must have extremely high resolution. Also, since any extra deformation due to the load created from contact between the measurement tool, such as a mechanical touch probe sensor and the experimental setup during the measurement could significantly affect the measurement, a non-contact measurement system would be preferred.

The non-contact measurement system used consisted of an IR camera, a CCD camera and a laser diode. The IR camera provided measurements of the change in surface temperature, while the CCD camera and the laser diode worked in tandem to measure the deformation.

### Temperature Measurement System

Temperature measurements were obtained using a FSI FLIR SC 500 ThermoVision uncooled IR camera. The detector was a focal plane array, uncooled microbolometer with a resolution of  $320 \times 240$  pixels and a thermal sensitivity of  $0.1^\circ\text{C}$  at  $30^\circ\text{C}$ . Its temperature range was  $-20^\circ\text{C}$  to  $120^\circ\text{C}$ , with an accuracy of  $\pm 2^\circ\text{C}$  full scale.

### Deformation Measurement

Longitudinal deformation was measured by tracking the drift of the laser diode spot, pointed by the robot tool flange, across the CCD chip of a CCD camera. Two CCD cameras were used to determine the deformation in orthogonal directions. Each camera was a CCIR standard Pulnix TM-6CN with a cell size of  $8.6(H) \times 8.3(V) \mu\text{m}$ , and resolution of  $752(H) \times 582(V)$ . To obtain the highest quality of laser spot images, each camera was adjusted using manual gain control in field mode, with the following settings:  $\text{gamma} = 0.45$ ,  $\text{blacklevel} = 0.1 \text{ mV}$ ,  $\text{whitelevel} = 0.7 \text{ mV}$  and  $\text{electronic shutter speed} = 1/10000 \text{ s}$ . The framegrabber was a monochrome National Instrument PCI-1408. The laser diode made by Schaefer and Kirchhoff, had a wavelength of  $638 \text{ nm}$ , maximum output power of  $11 \text{ mW}$ , and was tuned to be almost invisible to the naked eye.

The two CCD cameras, A and B, were located in the workspace such that the geometric centres of the CCD arrays had coordinates in a relatively fixed reference, Frame  $\{W\}$ , as listed in Table 2.1. When the robot pointed the laser towards Camera A or B, the corresponding configuration was called *Pose A*, or *Pose B*, respectively. The corresponding tool flange centre coordinates relative to Frame  $\{W\}$  are also listed in Table 2.2. The CCD camera reference coordinate origin and basic directions are illustrated on a schematic drawing of the front view of the camera in Figure 2.2. The coordinates of the laser spot in each of the two camera images were described with respect to the corresponding camera coordinate system.

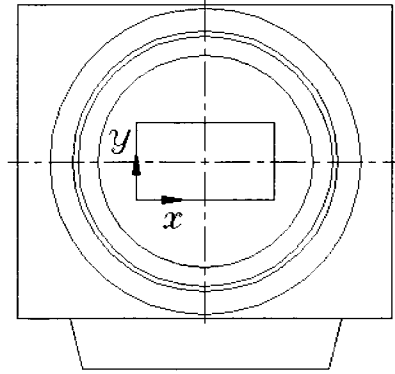


Figure 2.2: Reference coordinates for deformation measurement.

Table 2.1: Coordinates of Cameras A and B CCD chip centres expressed in Frame  $\{W\}$ .

Camera	$x_w$ (mm)	$y_w$ (mm)	$z_w$ (mm)
A	1017.20	-213.58	148.40
B	1016.20	-190.49	104.39

The camera coordinate planes were constrained with respect to the *world* coordinate frame of the robot,  $\{W\}$ , according to the location of both cameras, as illustrated in Figure 2.3. As stated in Leitner *et al* [14], the position and orientation of frame  $\{W\}$  were identical to that of the robot base frame and were located within the fixed zeroth link of the robot, as illustrated in Figures 2.1 and 2.3a. Figure 2.3b is an illustration of the cameras in their mounting brackets with the robot tool flange pointing the laser

Table 2.2: Coordinates of tool flange centre coordinates for *Pose A* and *B* expressed in Frame  $\{W\}$ .

Pose	$x_w$ (mm)	$y_w$ (mm)	$z_w$ (mm)
A	1087.78	-48.62	217.75
B	1087.33	-38.29	198.07

orthogonally onto Camera A as described in detail in [14]. Referring to Figure 2.3a, the  $y$ -axes direction of both cameras were parallel to the  $x_W$ -axis. The camera  $x$ -axis directions were different. For Camera A, the CCD array plane,  $xy_A$ , was parallel to the world frame plane  $xz_W$ . However, this was not the case for the plane  $xy_B$  of Camera B since the  $x_B$  axis was rotated about  $y_A$  by  $9.11^\circ$  [14].

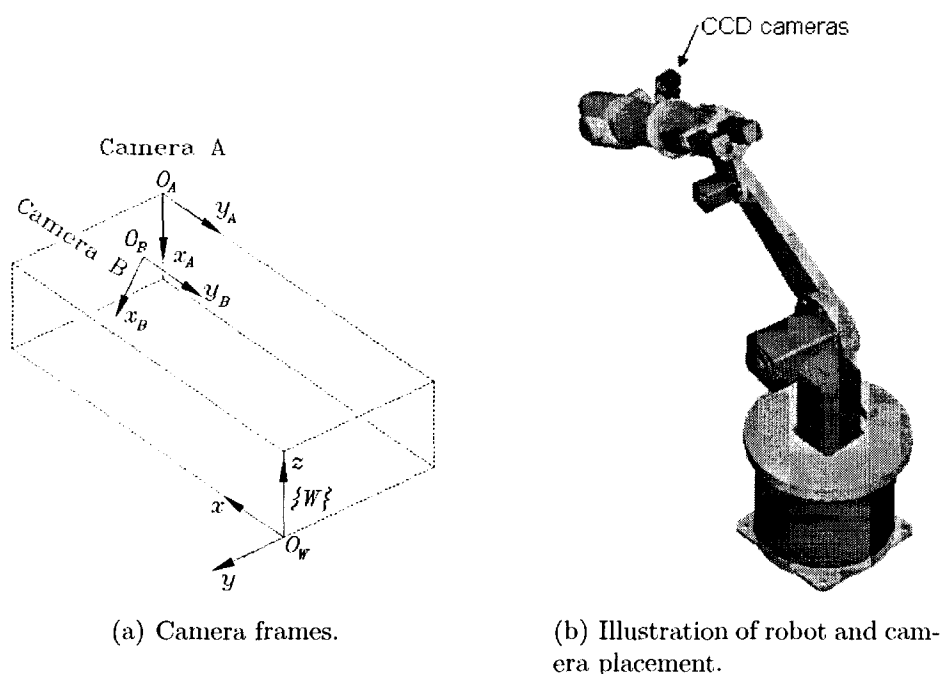


Figure 2.3: Camera placement and kinematic configuration for *Pose A*.

To get a focused image of the laser on the chip, the distance between the tip of the laser diode and the CCD array plane was 106 mm for both cameras and the laser was maintained nominally orthogonal relative to each CCD chip.

As indicated in the formative work by Leitner *et al* [14], it was assumed when the robot attained either of the two poses the first three links dominated the position error; therefore, in this case, only the joint angles of the first three joint axes were considered significant. This is a reasonable assumption for wrist-partitioned robots [2]. The joint angles for *Poses A* and *B* are listed in Table 2.3. The length of the first three links was

projected into the  $xy_w$ -plane using the nominal link lengths shown in Figure 2.1 and listed in Table 2.5. This allowed the effective link length to be determined.

Table 2.3: Joint angles for *Pose A* and *B*.

Joint	<i>Pose A</i>	<i>Pose B</i>
Axis	Joint angle ( $^{\circ}$ )	Joint angle ( $^{\circ}$ )
$\vartheta_1$	4.2300	4.2300
$\vartheta_2$	17.5462	17.5462
$\vartheta_3$	-16.8840	-16.8840
$\vartheta_4$	-89.5160	-89.5160
$\vartheta_5$	-66.8551	-57.7451
$\vartheta_6$	180.0000	180.0000

## 2.2.2 Experimental Procedure

The robot repeated a motion sequence of two taught configurations for a period of about 15 hours. In each pose the robot pointed the laser diode directly onto the CCD chip (*i.e.*, no lens). After posing the two camera configurations, the robot presented itself to the IR camera for a temperature measurement. The experiment was run three times using three different limits for joint actuator motor speeds: 30%, 75% and 10% of the maximum speed. Run 1 (30% speed) and Run 2 (75% speed) were started with the robot at ambient room temperature. For a study of contraction due to a decrease in temperature in Run 3 (10% speed), the robot was not allowed to cool down after completing Run 2.

The positioning repeatability in each camera plane was calculated from the positional variation of the laser spot on the CCD chips. The resolution of the laser spot images acquired by the CCD camera, which was estimated with the two-dimensional sub-pixel moment calculation [44], was approximately 1  $\mu\text{m}$ .

## 2.2.3 Experimental Results

### Temperature Results

The temperature distribution history of the robot during the measurement was recorded with the IR camera. The total change in temperature of the system over the course of the experiment was extracted from IR images taken at the start of the experiment (for room-temperature reference) and at the end of the experiment. IR images were also taken regularly during the experiment to verify the general trend of the temperature rise in the system.

Thermal images corresponding to start and end times are shown in Figure 2.4. Note that the hot spot visible on the nearly vertical arm of the robot in Figure 2.4a is the power supply of the laser diode. Leitner *et al* [14] determined by plotting temperatures of various locations over time that the resulting heating curves for those locations on the robot surface were all first-order exponential curves of the form  $y = y_0 + Ae^{-(x/\tau)}$ .

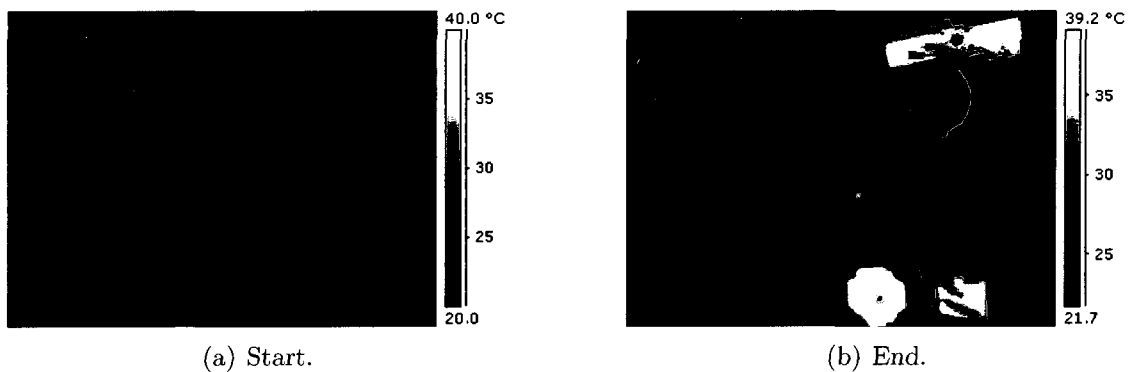


Figure 2.4: Thermal images of the robot at the start and end of Run 1.

## Deformation Results

Figure 2.5 illustrates a laser spot image recorded during the experiment. The temperature-induced deformation of the system was calculated from the positional variation of the laser spot on the CCD chips, which was extracted from the laser spot images.

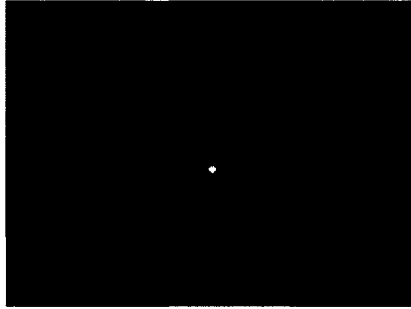


Figure 2.5: Camera A raw image.

Figure 2.6 illustrates plots of the laser spot centroid locations over time of both poses for all three runs. Note that the deformation,  $\Delta l_x$ , is measured as  $-\Delta y$  in camera coordinates. The heat generated by the operation of the robot caused its links to deform. Thermal effects dominated the locations of centroid over time during transient state, as can be seen with their exponential behaviour.

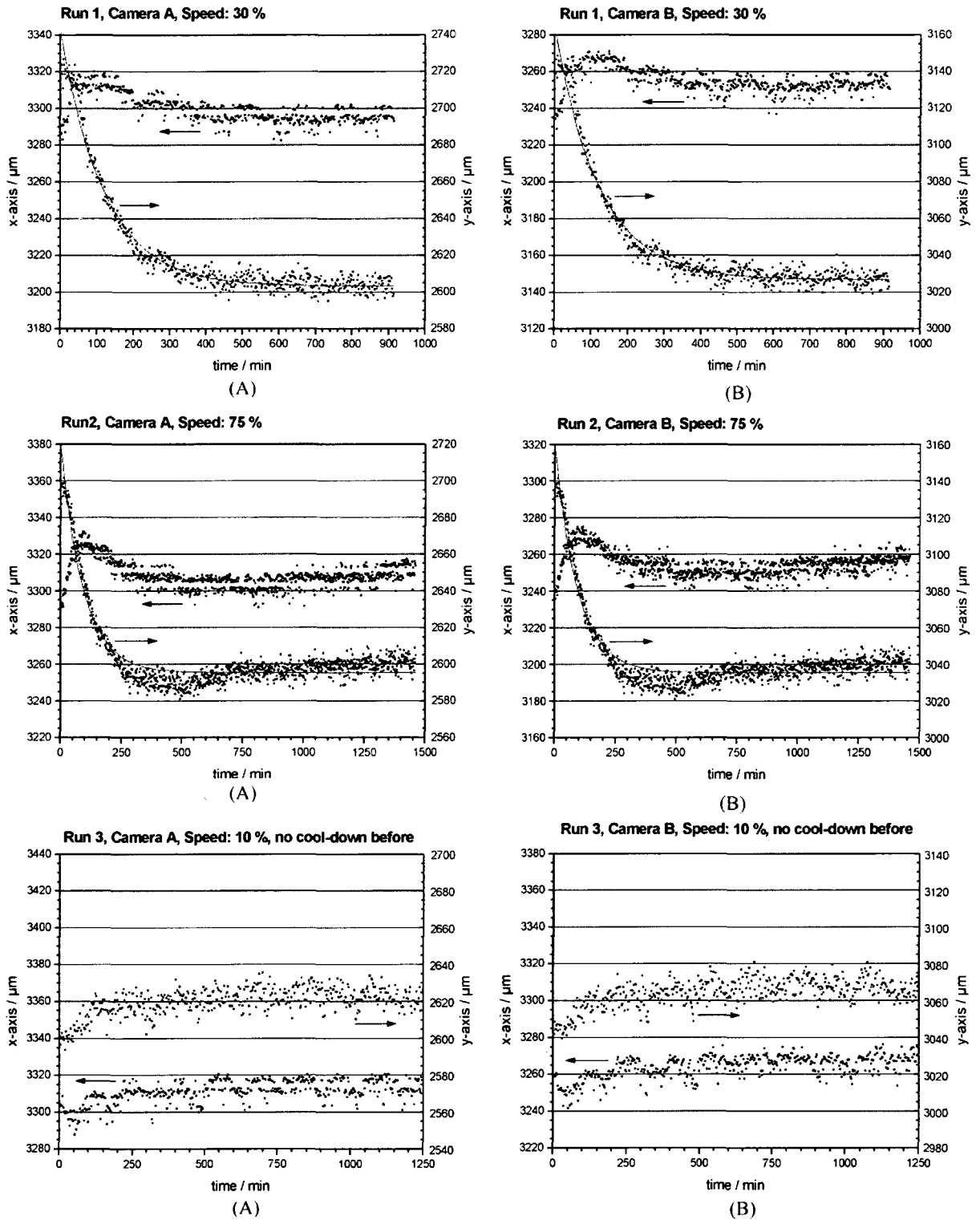


Figure 2.6: Laser spot centroid over time of *Poses A* and *B* for all runs.

## Summary of Experimental Results

The deformation,  $\Delta l_x$ , that was extracted from the laser spot migration measured by the cameras, and the change in temperature,  $\Delta T$ , is summarized in Table 2.4. Note that the deformation in the vertical direction,  $\Delta l_y$ , was not considered in this experiment and  $\Delta T$  was averaged from temperatures of 10 locations across the robot surface of each link.

Table 2.4:  $\Delta T$  and  $\Delta l_x$  from estimation of positioning repeatability experiment.

Run	Time	$\Delta T$ ( $^{\circ}\text{C}$ )				$\Delta l_x$ ( $\mu\text{m}$ )	
		Link 2		Link 3		Cam A**	Cam B**
1 (30%)	start	23.40	$\Delta T_2 = 4.70$	23.35	$\Delta T_3 = 6.75$	131	130
	end	28.10		30.10			
2 (75%)	start	24.40	$\Delta T_2 = 4.00$	24.34	$\Delta T_3 = 6.30$	120	120
	end	28.40		30.65			
3*(10%)	start	28.40	$\Delta T_2 = -1.20$	30.65	$\Delta T_3 = -2.20$	-40	-41
	end	27.20		28.45			

\* – cool down history.

\*\* – Camera A and Camera B.

The robot was supposed to start at room temperature for Run 2; however, this was not the case as shown in Table 2.4. The average link temperature at the start of Run 2 was  $1^{\circ}\text{C}$  greater than that of Run 1. The increase in temperature may be caused by the increase of room temperature, or the cooling down period of 10 hours between the end of Run 1 and the beginning of Run 2 that was not long enough to allow the link to cool down to room temperature. Note that for Run 3, the cool-down history, instead of the warm-up history, was recorded and presented.

### 2.2.4 Analytical Analysis

The goal of the analytical analysis was to estimate the coefficients of thermal expansion of the robot links and ascertain the accuracy of the estimated coefficients using the deformation and temperature results from the positioning repeatability experiment. In the

first part of the analysis, the coefficients of thermal expansion of the robot links were estimated using the change in temperature and deformation from the results of Run 1. Then, the accuracy of the coefficients was verified in the second part of the analysis. The coefficients were used to compute the deformation of the system as it corresponded to the change in temperature from the results of Runs 2 and 3. The deformation obtained from computation was compared to the deformation obtained from the experiment to ascertain the accuracy of the overall coefficient of thermal expansion.

### Determining Coefficients of Thermal Expansion

In general, it is well understood that most metals undergo a dimensional change that varies linearly with change in temperature, within a certain range. The linear coefficient of thermal expansion,  $\alpha$ , is defined to be

$$\alpha = \frac{\Delta l}{l\Delta T}, \quad (2.1)$$

where  $l$  is the nominal length at a specific initial reference temperature, and  $\Delta l$  is the deformation due to the change in temperature in degrees Kelvin (or Celcius because differences in temperature are considered),  $\Delta T$ .

The effective link length of the system was estimated from the basic geometry of the robot arm from the robot specifications [6]. With reference to Figure 2.7, it can be seen that

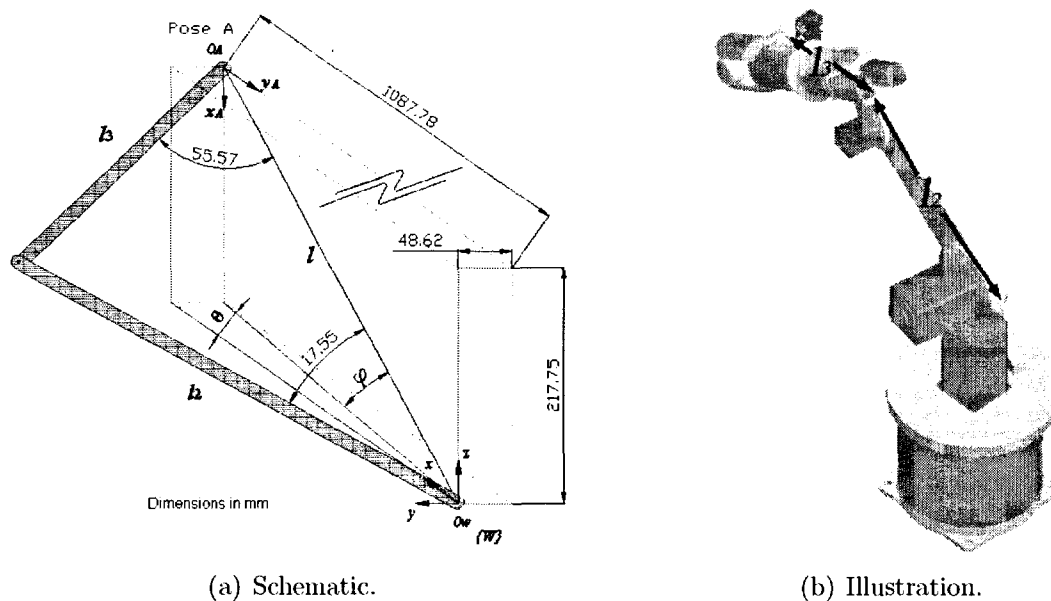
$$l = (l_2 \cos 17.55 + l_3 \cos 55.57). \quad (2.2)$$

The length  $l$  is the norm of the position vector of the tool flange centre in Frame  $\{W\}$ . This length was projected onto the camera frame to extract the deformation. The effective lengths  $l_2$  and  $l_3^2$ , listed in Table 2.5, included the portions of the robot links 1, 2, and

---

<sup>2</sup>The manufacturer specified link lengths of  $l_2 = 0.65 \text{ m}$  and  $l_3 = 0.74 \text{ m}$  respectively, however there were axis-to-axis values that are slightly different from the point-to-point measurement used here.

3 that were affected by heat transferred through the motor flanges at joint axes A1, A2, and A3 (joint parameters shown in Figure 2.1a).



(a) Schematic.

(b) Illustration.

Figure 2.7: Projected link length for *Pose A*.

The information of only the  $x$ -axes was considered because only in the  $x_w$ -axis (the  $y$ -axes of the camera) that the change in positional error exhibited first order exponential behavior, which corresponded to the behaviour observed in the temperature results of the positioning repeatability experiment. The thermal expansion was considerably more pronounced in the longitudinal direction of the link than in the other two directions (along the width and thickness of the link) as would be expected with the given geometry. The deviations of expansion in the other two directions were much smaller, less significant and therefore excluded at this stage.

Table 2.5: KUKA KR-15/2 *effective* link lengths at  $23 \pm 0.5^\circ\text{C}$ .

Link	Length (m)	Description
2	$l_2 = 0.70$	Effective distance between joint axes A2 and A3.
3	$l_3 = 0.78$	Effective distance between joint axes A3 and A5.

Equations (2.1) and (2.2) give:

$$\Delta l_x = \alpha (l_2 \cos 17.55 \Delta T_2 + l_3 \cos 55.57 \Delta T_3) \cos \phi \cos \theta. \quad (2.3)$$

$\Delta T$  and  $\Delta l_x$  from Run 1 are obtained from data listed in Table 2.4, while  $l$ ,  $\phi$  and  $\theta$  for *Pose A* are obtained from Table 2.1 and Figure 2.7. Angles  $\phi$  and  $\theta$  were determined using standard geometric and trigonometric relationships. For  $\phi = 11.31^\circ$  and  $\theta = 2.56^\circ$ ,  $\alpha$  can be determined:

$$\begin{aligned} \alpha_A &= \frac{131.00 \times 10^{-6}}{(0.70 \cos 17.55 \cdot 4.70 + 0.78 \cos 55.57 \cdot 6.75) \cos 11.31 \cos 2.56}, \\ &= 21.87 \times 10^{-6} K^{-1}. \end{aligned}$$

For *Pose B*,  $\phi = 10.32$  and  $\theta = 2.02$  and similarly:

$$\alpha_B = 21.63 \times 10^{-6} K^{-1}.$$

For this proof-of-concept approach, a simple averaging of  $\alpha_A$  and  $\alpha_B$  can be used for the purpose of estimating an overall coefficient of thermal expansion from the coefficients obtained for *Poses A* and *B* as follows:

$$\begin{aligned} \bar{\alpha} &= \frac{\alpha_A + \alpha_B}{2}, \\ &= 21.75 \times 10^{-6} K^{-1} \end{aligned}$$

In Table 2.6, the coefficient of thermal expansion calculated for each of *Pose A* and *Pose B*, and their average values are listed, together with the coefficient of thermal expansion of the 6061 Al, the principal structural material in the major of robot links [43].

Table 2.6: Linear coefficient of thermal expansion.

	Coefficient ( $\times 10^{-6} K^{-1}$ )
$\alpha_A$	21.87
$\alpha_B$	21.63
$\bar{\alpha}$	21.75
$\alpha_{6061}$	23.20 (20°C to 100°C [42])

### Verification Coefficients of Thermal Expansion

To ascertain the accuracy of the coefficients of thermal expansion listed in Table 2.6, these coefficients were, in turn, used to estimate the deformation of the system. The equation of the coefficient of thermal expansion was rearranged to calculate the deformation with respect to the change in temperature based on the deformation and temperature results from the positioning repeatability experiment. Using the change in temperature obtained from the experiment, the deformations that occurred during both Runs 2 and 3 were calculated and compared to the experimentally deformation listed in Table 2.4.

For Run 2,  $\alpha_A$  was used to predict  $\Delta l_x$  of *Pose A*. From Table 2.6,  $\alpha_A$  is determined to be  $21.87 \times 10^{-6} K^{-1}$ . Using Equation (2.3) and data listed in Tables 2.4 and 2.5,  $\Delta l_x$  can be obtained:

$$\begin{aligned}
 \Delta l_x &= \alpha_A (l_2 \cos 17.55 \Delta T_2 + l_3 \cos 55.57 \Delta T_3) \cos 11.309 \cos 2.559 \\
 &= 21.87 \times 10^{-6} (0.70 \cos 17.55 \cdot 5.00 + 0.78 \cos 55.57 \cdot 7.30) \cos 11.31 \cos 2.56 \\
 &= 140.46 \times 10^{-6} m.
 \end{aligned}$$

Because the robot did not cool down completely between Runs 1 and 2, the start temperature of links 2 and 3 at the start of Run 2 was 1°C higher than that of Run 1. To compare the predicted  $\Delta l_x$  with the measured  $\Delta l_x$  from the experiment of Run 2, an adjustment was required to account for the additional thermal expansion at the start of

Run 2. Using the same equation for computing  $\Delta l_x$  above, and the temperature difference of  $1^\circ\text{C}$ , the adjustment of deformation,  $\Delta l_{x_{adjust}}$ , due to the incomplete cool-down was computed.

$$\begin{aligned}\Delta l_{x_{adjust}} &= 21.87 \times 10^{-6} (0.70 \cos 17.55 \cdot 1.00 + 0.78 \cos 55.57 \cdot 1.00) \\ &\quad \cdot \cos 11.31 \cos 2.56 \\ &= 23.75 \times 10^{-6} \text{ m.}\end{aligned}$$

Therefore, the actual experimental  $\Delta l_x$  of Run 2 should be the sum of the experimental  $\Delta l_x$  (Table 2.4) and the corresponding adjustment. For *Pose A*:

$$\begin{aligned}\Delta l_x &= \Delta l_{x_{exp}} + \Delta l_{x_{adjust}} \\ &= 120.00 \times 10^{-6} + 23.75 \times 10^{-6} \\ &= 143.75 \times 10^{-6} \text{ m.}\end{aligned}$$

Similarly, for Run 3, using the appropriate values from Tables 2.4 and 2.5 to obtain  $\Delta l_x$  of *Pose A*:

$$\begin{aligned}\Delta l_x &= 21.87 \times 10^{-6} [0.70 \cos 17.55 \cdot (-1.20) + 0.78 \cos 55.57 \cdot (-2.20)] \\ &\quad \cdot \cos 11.31 \cos 2.56, \\ &= -37.94 \times 10^{-6} \text{ m.}\end{aligned}$$

Likewise,  $\Delta l_x$  of *Pose B*, predicted using  $\alpha_B$ , and  $\Delta l_x$  of *Pose A* and *Pose B*, predicted using  $\bar{\alpha}$ , were obtained by the same procedure. Note that for *Pose B*, with a different camera location from that of *Pose A*, the values of  $\phi$  and  $\theta$  were changed from  $11.31^\circ$  and  $2.56^\circ$  to  $10.317^\circ$  and  $2.039^\circ$  respectively. All results are listed in Table 2.7.

Table 2.7:  $\Delta l_x$  and prediction error.

		Run 2	Run 3	
$\alpha_{A\ CameraA}$	$\Delta l_x (\mu m)$	Predicted	140.46	-37.94
		Measured	143.75	-40.00
	%error		-2.29	-5.15
$\alpha_{B\ CameraB}$	$\Delta l_x (\mu m)$	Predicted	139.44	-37.67
		Measured	143.57	-41.00
	%error		-2.88	-8.12
$\bar{\alpha}_{\ CameraA}$	$\Delta l_x (\mu m)$	Predicted	139.69	-37.74
		Measured	143.62	-40.00
	%error		-2.74	-5.65
$\bar{\alpha}_{\ CameraB}$	$\Delta l_x (\mu m)$	Predicted	140.21	-37.88
		Measured	143.70	-41.00
	%error		-2.43	-7.61

## 2.2.5 Discussion

The appropriateness of the deformation and temperature measurement systems was verified in this proof-of-concept work. The small errors between the measured temperature-induced deformation and the predicted deformation, using the  $\alpha$ 's computed from data obtained from the measurement systems, confirmed the suitability of the accuracy level of both measurement systems.

Coefficients of thermal expansion based on the deformation recorded by Cameras A and B were computed from the data of Run 1. These were, in turn, used to predict the thermal deformation for Runs 2 and 3 using the corresponding measured changes in temperature and geometry of the robot. All computed  $\alpha$ 's listed in Table 2.6 were less than that reported [42] for the 6061 Al. The relatively consistent agreement in all values of  $\alpha$ 's suggested several possibilities. It is possible that the overall  $\alpha$  of the actual robot links was less than  $\alpha$  of the 6061 Al, which was the principal, but not only, constituent of the links. Second, the smaller value of computed  $\alpha$ 's might be caused by the construction of

the robot such that natural expansion of the links was restricted. Third, and most likely, other uncertainties in the experiment were contributing to an apparent reduction in  $\alpha$ . In particular, there was concern about the motion of the robot and the CCD camera during the measurement, as the robot might not be completely still when the laser spot images were taken and the camera might be affected by the idle-induced robot vibration.

Table 2.7 reveals that the predicted temperature-induced deformation was consistently smaller than the actual deformation. For Run 2 the motor speed was increased from 30% to 75% of maximum motor speed. The adjustment to correct errors due to the start temperature of Run 2 was required for all  $\Delta l_x$ . For Run 3, the opposite trend were found. The cool-down effects resulted in thermal contraction associated with the overall temperature decrease caused by the 10% motor speed. Regardless, the trend in the predicted deformation was consistent: the predicted contraction was less than the measured contraction.

As expected,  $\Delta l_x$  of *Pose A*, predicted using  $\alpha_A$  was more accurate than when predicted using  $\bar{\alpha}$ . However, using  $\bar{\alpha}$ , the overall prediction for the data of both cameras was more accurate. The better overall prediction from  $\bar{\alpha}$  suggests that  $\bar{\alpha}$  provided adequate predicted values of  $\Delta l_x$  for a basic approximation. Using only one value of  $\alpha$  for all links greatly simplified the mathematical model and reduced calculation time.

Once the robot had warmed-up, *i.e.*, the robot had reached its thermal steady state, its positioning repeatability was nearly one order of magnitude better than the manufacturer's stated repeatability ( $\pm 9\mu\text{m}$  [14] as opposed to  $\pm 100\mu\text{m}$ ). It is noteworthy that no mention of such heating effects on robot performance can be found in the manufacturer-supplied operating literature for the KUKA KR-15/2 [6].

The major implication of these results is that if the thermal response of the robot for specific cyclic tasks is known, the temperature-induced deformation can be numerically predicted and compensated for by the controller, eliminating the need to allow the robot to

warm-up. If the prediction and compensation are sufficiently accurate, the repeatability of the robot will be improved substantially thereby allowing the robot to perform consistently better than its manufacturing specifications.

The dominant material comprising the KUKA robot links was assumed to be 6061 Al. This assumption was made based on personal experience and knowledge of the material properties of aluminum. Although the results showed good agreement between deformation obtained from the experimental and data analyses using the material properties of the 6061 Al, a proper verification of the actual type of aluminum comprising the robot arm was still required. This material analysis and verification was later completed as part of the original contributions presented in this thesis, but is presented in the following section for completeness as the resolution of this issue is directly related to the outcome of the proof-of-concept work.

## 2.3 Electron Probe Microanalysis (EPMA)

A new series of experiments was planned to continue the positioning repeatability work performed in [14]. An experimental apparatus in the Robot Mechanical Systems Laboratory at Carleton University was set up to be as similar to the original system as possible, except that the KUKA robot was replaced by an A465 Thermo CRS robot. Analytical and numerical analyses were also performed for cross-checking the results. For this work, the material properties of the type of the assumed aluminum comprising the robot arm were collected from standard tables in material handbooks. It was essential that the material comprising the robot arm be clearly specified prior to the initiation of the series of experiments. Since the manufacturer of the A465 robot, Thermo CRS Ltd., was not able to supply the specific type of aluminum alloy used for the A465 robot arm, sample material from the actual robot arm was sent for an electron probe microanalysis (EPMA).

Both quantitative and qualitative EPMA analyses were performed.

To accurately analyze the composition of the material, two methods were applied to the sample piece obtained from the robot arm, as well as on a piece of 6061 Al as a reference. First, the samples were analyzed with a scanning electron microscope (SEM). The Cameca Camebax MBX electron probe microanalyser used in the Microprobe/SEM lab at the Department of Earth Sciences, Carleton University, scanned the sample surfaces with a high-energy beam of electrons in a raster scan pattern to obtain information such as surface topography, composition and electrical conductivity. A wide range of magnifications was available from about 25X, which was approximately equivalent to a magnification of a powerful magnifying glass to about 250,000X. High-resolution images provide three-dimensional images for surface structure studies.

For the second analysis, a collection of back-scattered electron (BSE) images was analyzed. By elastic scattering, the composition of the samples were determined through the reflection of beam electrons from the samples. The intensity of the BSE signal was strongly related to the atomic number ( $Z$ ) of the specimen.

### 2.3.1 Analysis Methods

Thin sample pieces, each with  $2 \times 2 \text{ mm}^2$  cross-sectional area, of the A465 robot arm and the 6061 Al standard were sent to the Microprobe/SEM lab at the Department of Earth Sciences, Carleton University for analysis. The pieces were each mounted in epoxy resin in a disk 25.4 mm (1 in) in diameter then ground and polished to a fine finish. The discs were subsequently coated with a layer of conductive carbon approximately 25 nm deep. The coated discs, or analysis specimens, were then placed in the sample chamber of a Cameca Camebax MBX electron microprobe.

### **Quantitative Electron Probe Microanalysis**

Quantitative EPMA's were made by the wavelength-dispersive method (WDX) using a four-spectrometer Camebax MBX electron probe operated at 20 kV accelerating potential and a beam current of 20 nA with the beam rastered over an area of  $5 \times 5 \mu\text{m}^2$ . The WDX counted the number of x-rays of a specific wavelength diffracted by a crystal. Peak counting times for each element were 40 s, which is equivalent to 40,000 counts. Background counting times were made at  $\frac{1}{2}$  peak counting time on each side of the analysed peak. Also, raw x-ray data were converted to elemental weight percent by the Cameca PAP matrix correction software.

### **Qualitative Electron Probe Microanalysis**

Qualitative EPMA analyses were made by the energy-dispersive x-ray spectroscopy (EDX), which is an integrated feature of the SEM. The x-rays emitted from a specimen in response to being hit with charged particles was analyzed. The number and energy of the x-rays were measured by an energy dispersive spectrometer, which allowed the elemental composition or chemical characterization of the specimen to be determined. The EDX of the matrix and inclusions of the samples were collected with a Kevex Si solid state x-ray detector and Aptec amplifier interfaced to a spectral engine from 4Pi Analysis Inc., utilizing the NIST<sup>3</sup> Desk Top Spectrum Analyzer software. The quantitative EPMA results are presented in tabulated format and the qualitative EPMA images are presented in section 2.3.2.

### **Back-Scattered Electron Image Analysis**

Digital back-scattered electron (BSE) images were collected for a cross-reference analysis. BSE forms an image by moving a beam of focused electrons across an object and reading both the electrons scattered by the object and its secondary electrons. The images were

---

<sup>3</sup>National Institute of Standards and Technology.

collected with an Electron Optic Services digital imaging system at a resolution of  $512 \times 512$  pixels with a Lamont 4 element solid state BSE detector. The BSE Quad Summing Amplifier was linked to a digital imaging, and the EDX system. The BSE images are presented in section 2.3.2.

### 2.3.2 Results

Quantitative EPMA results of robot and 6061 Al specimens are presented in Table 2.8. Three sets of analyses were completed for each specimen to provide a composition matrix of the specimen, inclusions of the specimen and the overall composition. The nominal composition of each specimen is shown as a weighted percentage. Note that the composition of 6061-T6 aluminum alloy [42, 45] is also presented. From Table 2.8, it can be seen that the compositions of the overall bulk material, matrix and inclusions of the robot and the 6061 Al specimens are very similar. The composition of the 6061 Al specimen also matched well with the reference values [42, 45], with the exception of iron (Fe) and manganese (Mn). This good agreement between the compositions of the 6061 Al specimen and the reference confirmed the type of this known alloy, and also demonstrated that the analysis method was suitable for the range of composition. Therefore, the similarity in major composition of the robot and the 6061 Al specimens can be used to confirm with confidence that the material comprising the robot arm is 6061 Al.

The following were also observed: the amount of Fe and Mn was extremely high in the inclusions for both the robot and the 6061 Al specimens; the amount of aluminum (Al) in the inclusions was noticeably lower than that in the overall and the matrix; the composition was very similar between the matrix and the overall, but slightly different in certain specific components between the matrix and the inclusions; titanium (Ti) and zinc (Zn) were found to be lower than expected in the matrix, inclusions and overall; and the overall composition was generally very similar to the composition of the matrix.

Table 2.8: Nominal composition by weight %.

specimen	nominal composition wt%								
	Al	Si	Mg	Ti	Cr	Mn	Fe	Cu	Zn
AL [42, 45]	rem	0.4-0.8	0.8-1.2	0.15	0.04-0.35	0.15	0.7	0.15-0.40	0.25
AL									
· overall	99.22	0.57	0.85	0.02	0.08	0.03	0.08	0.21	0.02
· matrix	98.83	0.67	1.00	0.02	0.09	0.02	0.13	0.19	0.03
· incl.	75.47	6.58	0.40	0.01	0.72	0.72	20.77	1.31	0.04
robot									
· overall	99.12	0.47	0.83	0.01	0.07	0.04	0.06	0.19	0.02
· matrix	98.75	0.60	0.94	0.02	0.07	0.05	0.30	0.21	0.03
· incl.	81.38	5.55	0.59	0.00	0.14	0.61	18.56	1.15	0.02

Al = 6061-T6 aluminum alloy

incl. = inclusions

### 2.3.3 Discussion

The results show good agreement in the composition of the robot and 6061 Al specimens with some small differences in specific components. According to materials handbooks [42, 45], the composition found in the material comprising the robot arm matched the 6061-T6 aluminum alloy in all main components. Although the composition also matches several other types of aluminum, most of them lack the other properties that would make them suitable for manufacturing or as use in industrial robot arms. The 6061 Al alloy is widely used in a variety of industries including industrial robots, therefore it is reasonable to assume that the material comprising the A465 robot, and possibly the KUKA KR15-2 robot, was 6061-T6 aluminum alloy.

## 2.4 Next Steps

Recall that the goal of this thesis is to develop a complete process for compensating for temperature-induced deformation, from generating a predictive model to implementing compensation in a robot mechanical system. However, to be able to reach this goal within the time frame for the thesis, the mechanical system needed to be simplified. The 6-DOF robot in the repeatability experiment was represented by simpler models: single-link and two-link systems; in which the magnitude of the longitudinal deformation was dominant. Studying the simple mechanical systems allows for a more comprehensive understanding of the deformation behaviour in an appropriate time frame. The single-link and two-link systems are introduced in Chapter 3 and Chapter 5 respectively.

# Chapter 3

## Single-Link Experiment

### 3.1 Introduction

During the proof-of-concept work with the positioning repeatability experiment (presented in Chapter 2), a number of concerns were identified such as the motion of the robot and the CCD camera. These were potential sources of errors. It was found that a better understanding of the nature of the temperature-induced deformation problem, the behaviours of the measurement system, and the properties of the mechanical system was required in order to accurately interpret temperature-induced deformation data in three dimensions. The 6-DOF industrial robot was deemed an unsuitable subject for gaining this fundamental insight due to its complex mechanical structure. It was decided to investigate a simplified, but representative, system with better known nominal properties.

A single-link system of one slender link and one servo motor similar to those used in small payload industrial robots was constructed. The temperature-induced deformation of the link caused by heat losses transferred from the motor could then be investigated. The link was made of 6061 Al, the material comprising the robot arm analyzed in Chapter 2, and was designed to be slender and thin in order to enable longitudinal deformation of the

system to be dominant.

General concepts and procedures for a new single-link experiment were similar to the positioning repeatability experiment, and provided three models: experimental, analytical and numerical. The experimental model considered two cases: stationary and moving. In the stationary case, the link remained fixed and horizontal, where as in the moving case, motions of the link were controlled by the wrist motion (sixth axis) of a Thermo CRS A465 robot. The analytical model was used for a study of the stationary case only. The numerical model was used for a study of the moving case only.

The development of each model is presented separately in Sections 3.2 through 3.4. Each model provides results including temperature distribution and temperature-induced deformation (*i.e.*, changes in dimensions) for the link over a period of one hour. The results corresponding to the stationary and moving cases are compared and discussed in Section 3.5. The single-link system was studied using concomitant experimental, numerical and analytical models to provide cross-checking of the results with the view to developing a strategy to provide, *a priori*, compensation for temperature-induced deformation through a robot controller algorithm.

## 3.2 Experimental Model

The home position of the single-link experimental setup; *i.e.*, a simplified robot mechanical system, is shown in Figure 3.1. The non-contact measurement system used is based on the measurement systems of Leitner *et al.* [14], Fratpietro and Hayes [34] and Simpson and Hayes [39]. It is comprised an IR camera, a CCD camera and a laser diode. It was setup for simultaneous and continuous measurements to estimate deformation and temperature changes of the simplified robot mechanical system.

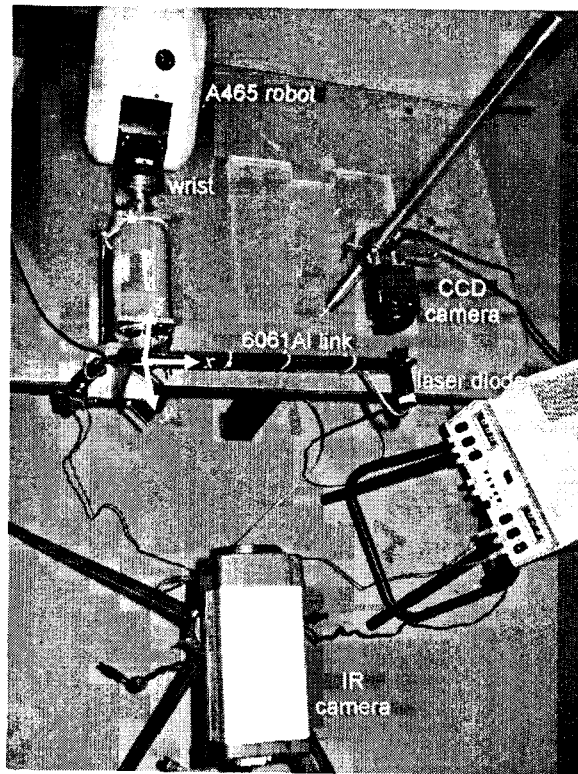


Figure 3.1: Experimental apparatus.

### 3.2.1 Simplified Robot Mechanical System

To study uni-directional deformation, the link of the single-link system was designed to be slender. Its length-to-width ratio of 10 ensured that the longitudinal deformation dominated the effects caused by an increase in temperature. The thickness of the link was approximately one quarter of the width, and thus, the deformation in the direction of the thickness was relatively insignificant. One end of the link was fixed to an output shaft of a servo motor, similar to those generally used in small payload industrial robots. A laser diode was fastened to the free end of the link. The laser beam of the diode was pointed straight at the CCD camera, providing laser images for deformation measurement. When the link was heated, the deformation extracted from the location of the laser spot represented the total deformation of the link in a longitudinal direction.

In reality, robot motors work to provide motions to the links. Generated heat losses due

to friction, etc. may cause thermal deformation of the links. For the purpose of analysis, precise knowledge and control of the amount of heat loss was required for the simplified robot mechanical system. The simulated heat loss was externally supplied using a silicone rubber heating pad. The output shaft of the motor, between the motor case and the link, was wrapped with the heating pad, which was plugged into a variac to control the heat input. The motion of the link was provided using the tool flange motor of a Thermo CRS A465 robot system consisting of a six-axis A465 robot, and a C500C controller. For the moving case, the motion imparted to the link was a reciprocating  $180^\circ$  arc. The A465 robot had nominal payload of 2 kg, and its repeatability was  $\pm 50 \mu\text{m}$ .

The link was 330.2 mm long, 25.4 mm wide and 6.4 mm thick. There was a hole at each end to accommodate, respectively, the output shaft of the motor and the laser diode. The centre of the output shaft hole was located at 25.4 mm from the proximal (near) end of the link. The centre of the laser diode hole was located 13.2 mm away from the distal (far) end of the link. The diameters of the shaft and the diode holes were 8.0 mm and 19.0 mm respectively. The link was painted flat black, emissivity  $\simeq 0.95$  [46], to reduce infrared and visible spectrum reflections that induced uncertainty for temperature readings in the experiment.

As illustrated in Figure 3.1, the link was attached to the output shaft of the motor. The output shaft was inserted into the hole on the link with an interference fit, and secured with two set screws. The laser diode was inserted into the hole at the distal end of the link, using both an interference fit and then fastened with two set screws. The input shaft of the motor was attached to the A465 robot via an aluminium coupling and a thermally insulating delrin acetal resin disk, as shown in Figure 3.2.

The coupling was aligned with the wrist of the robot to prevent link wobble. The coupling was fastened securely by four screws to prevent play, and to attach the tool flange of the robot to the input shaft of the motor. The 12.7 mm thick delrin disk, which

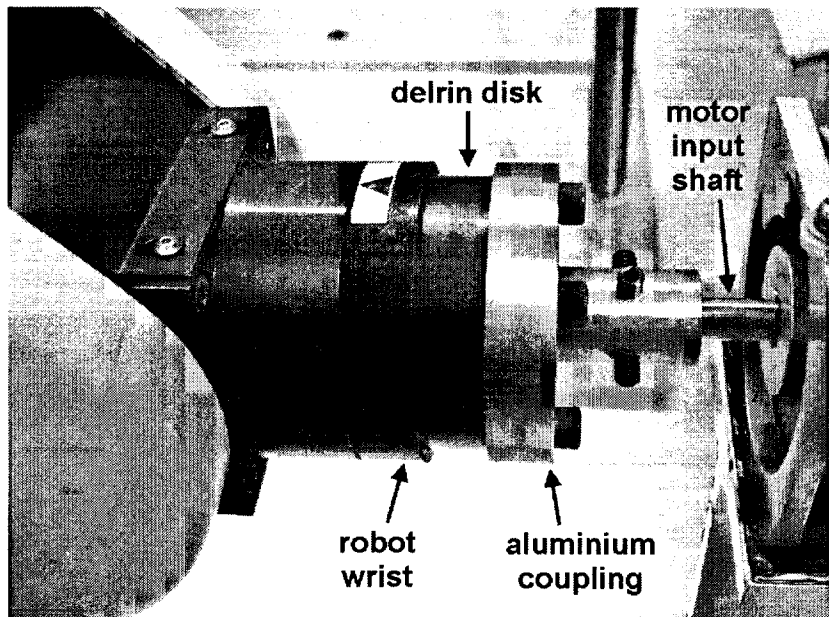


Figure 3.2: Coupling and delrin disk.

was inserted between the coupling and the robot wrist, provided thermal insulation from the A465 to the simplified robot mechanical system. The insulation prevented extra heat from the wrist of the robot, which was generated when the wrist worked to provide motions to the link, from being transferred to the coupling and the single-link system.

Motions of the link were controlled by Joint 6 of the A465 robot, and local heating of the link was consistently provided by the silicone heating pad. The heating pad was wrapped around the output shaft in an area between the motor case and the link. Using the heating pad, the temperature of the shaft was increased from approximately  $22^{\circ}\text{C}$  to approximately  $36^{\circ}\text{C}$  in the stationary case, and from approximately  $22^{\circ}\text{C}$  to approximately  $42^{\circ}\text{C}$  in the moving case.

Note that the subject of interest of the single-link experiment was the simplified robot mechanical system, and not the A465 robot. The study focused on the temperature distribution and the total deformation of the link of the simplified robot mechanical system. The A465 robot was utilized as a tool for providing precise motion to the link of the

simplified robot mechanical system for the moving case. It did not replace the role of the KR-15/2 robot in the positioning repeatability experiment presented Chapter 2.

### 3.2.2 Optical Measurement System

The non-contact measurement system introduced in the positioning repeatability experiment demonstrated sufficient measurement accuracy for the single-link experiment, and was implemented, with minor modifications, to allow the system to better suit the requirements of this new experiment. An IR camera, described next, was used to measure the temperature change. The deformation measurement, built on techniques of measurement systems of [34] and [39], tracked the drift of laser spot across the CCD camera chip.

#### Temperature Measurement

Temperature measurements were obtained with a FLIR A40M IR camera. Its detector was a focal plane array, uncooled microbolometer with spatial resolution of 1.3 mrad and thermal sensitivity of  $0.08^{\circ}\text{C}$  at  $30^{\circ}\text{C}$ . The temperature range used was  $-40^{\circ}\text{C}$  to  $120^{\circ}\text{C}$ , with an accuracy of  $\pm 2^{\circ}\text{C}$  full scale. The IR camera was positioned so as to obtain a frontal view of the link when in the home position, as shown in Figure 3.1.

Each image recorded by the IR camera contained both coordinates and temperature. The IR images were extracted with ThermaCAM<sup>TM</sup> Researcher 2.8 software [47], developed by FLIR System AB, for temperature of locations required for the analysis.

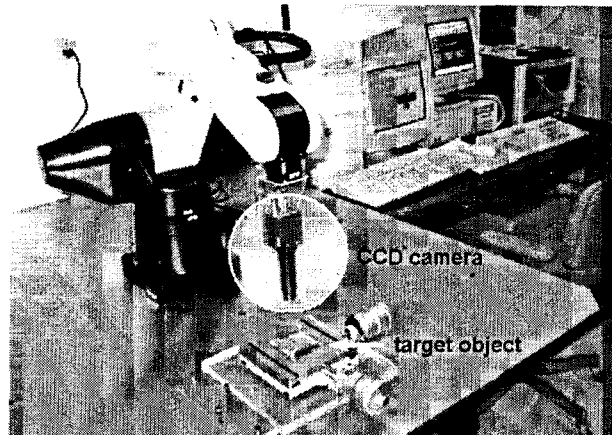
#### Deformation Measurement

The deformation measurement system of the single-link experiment was built on the techniques of the measurement system of Fratpietro, Simpson and Hayes [34, 39] developed at the Robot Systems Laboratory at Carleton University. The measurement technique of tracking the drift of a laser diode spot across the CCD chip of a CCD camera from [34, 39]

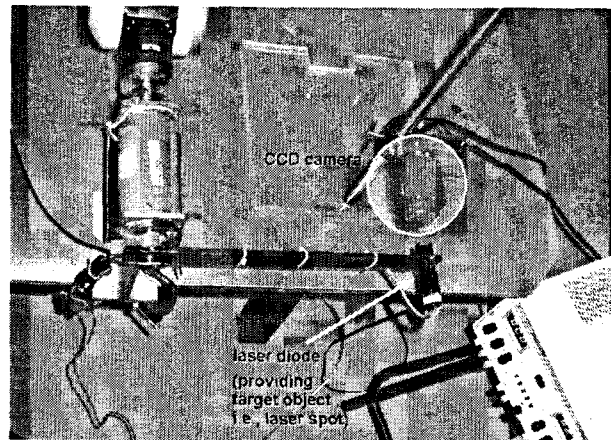
was reused with a modification associated with switching the mounting system of the CCD camera. In the original measurement system, the CCD camera was mounted on the robot tool flange, with the intention of giving the camera the same motion as the robot arm. The target object was mounted on a workbench. Examination of the preliminary data [14], along with the proof-of-concept work, suggested that the motion of the robot, and the CCD camera, were sources of errors. The robot was not completely still when the image was taken and/or the camera was affected by the vibration of the robot idle. The measurement system provided more accurate measurements when the CCD camera was stationary [10]. Thus, for the new measurement system, the CCD camera was mounted stationary on the workbench while a laser diode was mounted on the tool flange of the A465 robot. In the moving case experiment, the laser diode moved in unison with the link, and both paused to point the laser beam on the firmly mounted CCD camera. Figure

The CCD camera and the gain settings used were identical to those of the positioning repeatability experiment described in Section 2.2.1. The framegrabber was a monochrome National Instrument PCI-1409. Image distortion was attenuated by pointing the laser directly on the CCD chip. The laser diode was made by StockerYale and had a wavelength of 635 nm. It was tuned to be virtually invisible in order to limit numbers of brightened pixels of the CCD chip, with the expectation of enhancing the accuracy of the laser spot centroid extraction algorithm. All laser spot images acquired by the CCD camera were recorded as bitmap files and the geometric extracted centroid was extracted with an image processing algorithm implemented in MATLAB. The algorithm extracted the geometric centroid of the laser spot by summing the pixel moments in two orthogonal directions [48] yielding sub-pixel accuracy. The laser spot geometric centroid extraction algorithm is presented in detail in Section 3.2.3.

When the link was in the home position, the CCD camera was placed so that the laser diode pointed straight at the CCD chip. The longitudinal axis of the link was parallel



(a) Experimental apparatus by Fratpietro, Simpson and Hayes [34, 39].



(b) Single-link experimental apparatus.

Figure 3.3: Comparing experimental apparatus.

to the  $x$ -axis of a reference frame, and the laser diode was on the right-hand side of the motor, when viewed from the front, as shown in Figure 3.1. The diode was perpendicular to the deformation direction in the  $xy$ -plane (but at the same level in the  $z$ -axis), therefore the front plane of the laser diode was parallel to the front plane of the link. Hence, the drift of laser spot centroid locations detected by the CCD camera accurately represented the drift of the link. In Section 4.2, further explanation on possible measurement error caused by misalignment of the laser diode is presented.

### 3.2.3 Software

#### LabVIEW Virtual Instrument

Since the measurements of deformation and temperature must be synchronized, it was critical to have a reliable automated communication system between the two measurement systems. A virtual instrument was developed with communication protocols implemented in LabVIEW to handle the image-acquiring processes of both the CCD camera and IR camera, and their communication with the robot controller. A serial communication link was established between the C500C robot controller and the development computer to acquire the motion from the A465 robot. Communication between the virtual instrument and the robot controller was achieved using a command file developed in the RAPL-III CRS software. Communication between the virtual instrument and the IR camera was achieved using a toolkit developed specifically for LabVIEW application by FLIR Systems AB [47].

Prior to each measurement, the communication port and storing location of the images acquired by the cameras were specified in the virtual instrument. Similarly, the desired trajectory of the robot had to be specified through the RAPL-III command file. The virtual instrument and the RAPL-III program allowed the measurement to be completed automatically and consistently throughout the whole experiment, which helped to eliminate possible human errors. A flow diagram of the image acquisition and robot motion control process is presented in Figure 3.4.

#### Laser Spot Geometric Centroid Extraction Algorithm

The drift of laser spot centroid locations across the CCD chip was investigated for the deformation measurement. Each image of the laser spot, a white dot on a black background, acquired by the CCD camera, was processed to estimate the coordinates of its centroid.

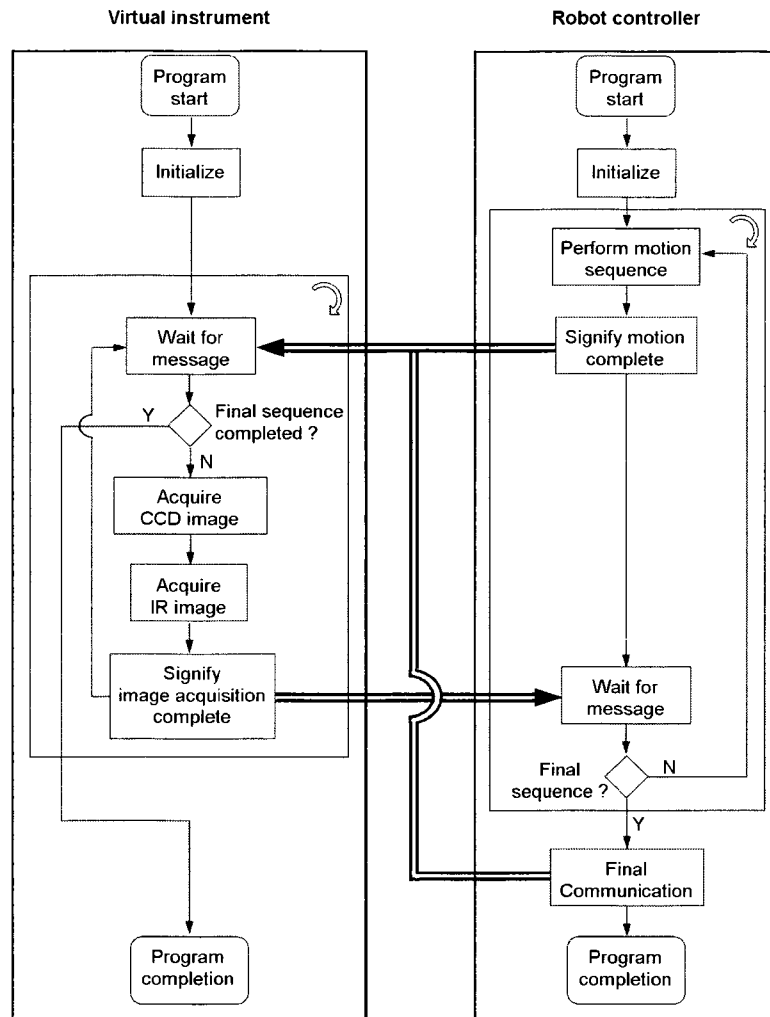


Figure 3.4: Flow diagram of image acquisition and robot motion control process.

Each digital image was processed in MATLAB. The algorithm extracted from the image a matrix of pixel intensities representing each discretized shade of gray within the image. Each pixel in the image of the laser spot contained a 16-bit grayscale value corresponding to intensity of the laser at a specific location. The scale ranged from black to white, and was evenly divided. Each shade of grayscale was assigned a discrete 16-bit value between zero and 65,535 (or  $2^{16} - 1$ ), where zero corresponded to the black, and 65,535 corresponded to the white. These values mapped the voltage produced in the presence of light and the resulting digital representation of this intensity in the image. Pixel intensity resolution

was increased by limiting the range of voltages observed by the CCD camera. The upper and lower limits of the voltage, adjusted through the framegrabber software, were 0 V and 1.4 V respectively. All voltages above the upper limit were assigned an arbitrarily large intensity value of 65,535 and all voltages below the lower limit were assigned to zero, *i.e.*, a binary image.

The actual area represented by each pixel on the Pulnix TM-200 CCD camera was approximately  $0.01 \text{ mm}^2$ . Therefore, the dimensional resolution of images obtained by this camera was  $\pm 5 \mu\text{m}$ . Comparing the expected 30 - 50  $\mu\text{m}$  deformation of the link, based on its length and coefficient of thermal expansion, to the resolution of the images provided by the CCD camera, it was found that the image resolution was relatively low and may not have been sufficiently accurate for the analysis of the deformation results. To increase the resolution of the result images acquired by this camera, the images needed to be extracted at sub-pixel accuracy using sub-pixel moment calculations. Figure 3.5 illustrated that the intensities of surrounding pixels effectively shift the coordinates of the pixel centre. Accounting for this effect enables computation of the laser spot centroid to sub-pixel accuracy.

Treating the intensities as masses, sub-pixel moment calculations can be estimated using moment Equations (3.1) and (3.2):

$$i = \frac{\sum \sum i \times I^P(i, j)}{\sum \sum I^P(i, j)}, \quad (3.1)$$

$$j = \frac{\sum \sum j \times I^P(i, j)}{\sum \sum I^P(i, j)}. \quad (3.2)$$

$I^P(i, j)$  is the intensity of the pixel at the coordinate  $(i, j)$  taken from the raw image data. These values were summed over a  $3 \times 3$  pixel area. The calculation was performed for each of the two coordinates at the location specified by the coordinates in the segmented data array.

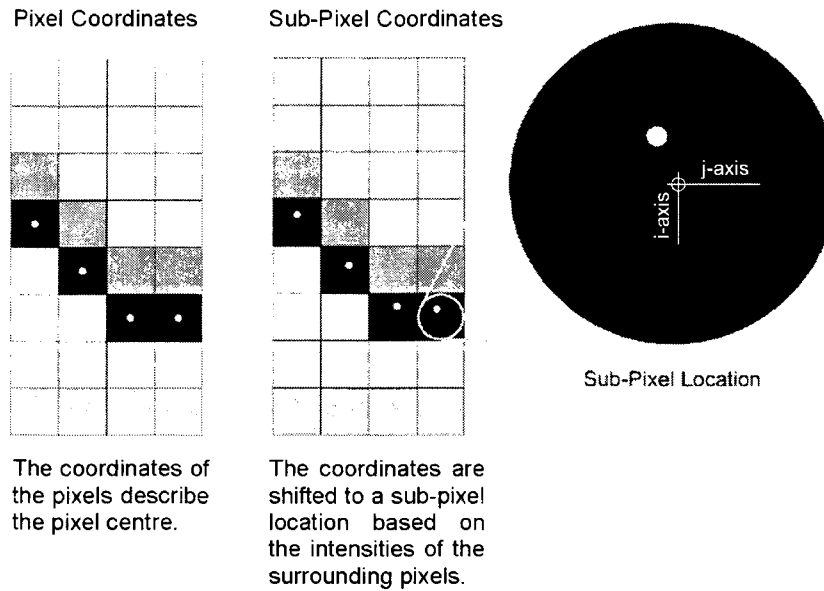


Figure 3.5: Sub-pixel coordinates [34].

### 3.2.4 Procedure

As indicated previously, three models were considered for the single-link system: experimental, analytical and numerical. Both a stationary link and a moving link were examined. The experimental model provides the observed actual deformation in a robot mechanical system, while the analytical and numerical results give predicted deformation which could potentially be exploited in a compensation methodology.

The stationary case mapped the temperature-induced deformation to the change in temperature. Effects of motion were eliminated in the stationary case. In the moving case, motion-induced mechanical effects as well as some forced convection were modelled in the numerical model.

#### Stationary Case

In the absence of link motion, the goal was to benchmark temperature-induced deformation. Experimental results from the non-contact measurements were compared to predicted

results obtained from an analytical model. The link was set in the home position and remained in this position throughout the experiment. Heat was applied to the output shaft through the heating pad. When the heating pad was turned on, an average temperature of the shaft increased from 22°C to 36°C over approximately two minutes. The CCD camera captured an image of the laser spot every two minutes over a period of one hour. These images were used to extract the drift of the laser spot centroid coordinates that represented deformation of the link. The IR camera automatically acquired an IR image immediately after each laser spot image was acquired for the corresponding temperature distribution of the link.

### Moving Case

In the moving case, the link rotated about the motor shaft axis continuously through a 180° cyclic motion between the home and the goal positions (*i.e.*, a windshield wiper motion), for a period of one hour. At 30 s intervals, the link stopped in the home position in order to allow the CCD and IR cameras to capture images of the laser spot and temperature distribution. The virtual instrument enabled the robot controller and the CCD camera to work together autonomously. IR images of the temperature distribution in the link were taken at both the beginning and end of the run.

## 3.3 Analytical Model

An analytical transient heat flow model was developed corresponding to the stationary case. The analytical model was developed to predict the total (steady state) longitudinal deformation of the heated slender link of the single-link system. For one-dimensional transient heat flow, the change in temperature,  $dT$ , at any time,  $\tau$ , and in any position,  $x$ ,

along the  $x$ -axis of a semi-infinite solid is [40]:

$$\frac{dT}{dx} = \frac{|T_i - T_o|}{\sqrt{\pi\alpha_d\tau}} e^{-x^2/4\alpha_d\tau}, \quad (3.3)$$

where  $T_i$  and  $T_o$  are the temperatures at the start and end of the period of interest, and thermal diffusivity,  $\alpha_d$ , is:

$$\alpha_d = \frac{k}{\rho c},$$

where  $\rho$  is the density,  $k$  and  $c$  are the thermal conductivity and specific heat of the material respectively. At any time,  $\tau$ , Equation (3.3) may be rewritten as:

$$dT = f(x) dx. \quad (3.4)$$

The total longitudinal deformation of the link between the centres of the shaft hole and the laser diode hole was of interest at the onset of steady state. In this case, with no motion involved, the effects of convection were considered negligible. In the absence of restraint, any differential element of the link would deform proportional to the change in temperature according to:

$$dL = L\alpha dT, \quad (3.5)$$

where  $L$  is the linear dimension, *i.e.*, nominal length ( $m$ ),  $T$  is the temperature ( $K$ ), and  $\alpha$  is the linear coefficient of thermal expansion ( $K^{-1}$ ). From Equation (3.5), the linear thermal expansion coefficient can be written as:

$$\alpha = \frac{1}{L} \frac{dL}{dT}, \quad (3.6)$$

where  $\frac{dL}{dT}$  is the rate of change of the length per unit change in temperature. If  $\alpha$  is known and does not vary over the change in temperature,  $dT$ , the change in linear dimension can be estimated as:

$$\Delta L = \alpha L |\Delta T| \operatorname{erf} \left( \sqrt{\frac{\rho c}{k \tau}} L \right). \quad (3.7)$$

Equations (3.7) is an analytical expression for the change in nominal length of the link,  $\Delta L$ , at any time,  $\tau$ , due to a change in temperature,  $\Delta T$ , at the location of the centre of the shaft hole. Material properties of the 6061 Al are listed in Table 3.1. It should be noted that the analytical model used one of the simplest semi-transient heat transfer equations, and did not include all of the boundary conditions and material properties which existed in the experimental model. Clearly the simple analytical model did not fully represent the physics of the single-link experimental model and small differences were expected between the results of the analytical and experimental models were to be expected. Nevertheless, the analytical model, in its simplicity, has the potential to be incorporated in a compensation methodology, the development of which is a goal of the thesis.

### 3.4 Numerical Model

For the moving case, ABAQUS [49] was used to perform a straight-forward coupled thermal-mechanical finite element analysis<sup>1</sup> (FEA) which incorporated transient thermal effects. The coupled thermal-mechanical FEA studies interactions of the one-way coupling in which temperatures from a thermal analysis drives a stress analysis. Convective heat transfer introduced by the motion of the link was considered, where convection heat trans-

---

<sup>1</sup>ABAQUS [49] using thermal-elastic analysis with small strains and small rotations, and user-defined material properties, was run in all cases on a Windows XP Pro OS, Pentium 4 2.8 GHz processor.

fer coefficient,  $h$ , was estimated to be  $7.75 \frac{W}{m^2 \cdot K}$  [40]. Mechanical effects (*e.g.*, inertia) were assumed to be negligible. The goal of this FEA was to provide an understanding of the thermal-mechanical environment in the moving case, in particular to examine the temperature-induced deformation.

The finite element model used eight-node trilinear (displacement and temperature) hexahedral elements. While this was a comparatively simple FEA, several mesh configurations and thermal convergence criteria were considered. Those presented here, provided good results (*i.e.*, less than 5% difference between the results of experimental and FEA models, see Section 3.5.2) in an acceptable run time. The assignment of elements of the single-link FEA model is presented in Figure 3.6. The link was modelled with 23 elements along its length, four elements across the width and was one element thick. A representative portion of the hollow drive shaft at the proximal end of the link was modelled with seven elements along its length and eight elements around its circumference to allow the application of the heat flux associated with the heating pad. The laser diode located at the distal end of the link had ten elements along its length and twelve elements in the cross section.

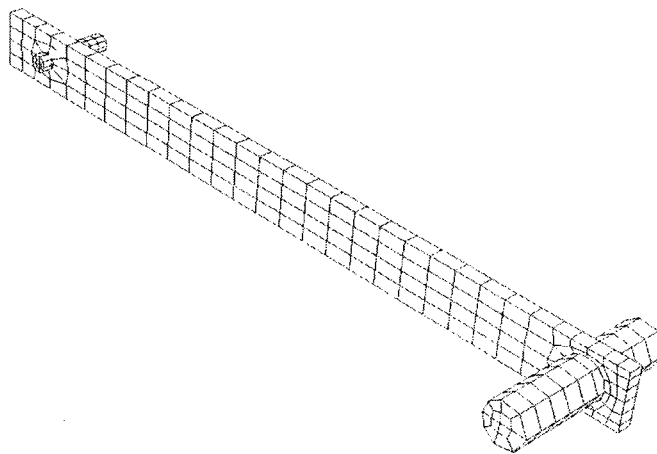


Figure 3.6: Element assignment of single-link FEA model.

### 3.4.1 Material Properties

The material properties used in the FEA are summarized in Table 3.1. All properties were selected for the expected temperature range of 20°C to 100°C and taken from material handbooks ([45, 50]). The link was 6061 Al. The shaft was 430 stainless steel (403 SS), and the laser diode was ABS plastic.

Table 3.1: Material properties.

Material Property	Symbol	6061 Al [45]	430 SS [45]	ABS [50]
Thermal conductivity $\left(\frac{W}{m \cdot K}\right)$	k	167	26.1	0.27
Density $\left(\frac{kg}{m^3}\right)$	$\rho$	2713	7800	1180
Young's modulus (Pa)	E	$7 \times 10^{10}$	$20 \times 10^{10}$	$0.23 \times 10^{10}$
Poisson's ratio	$\nu$	0.33	0.285	0.3
Linear coefficient of thermal expansion ( $K^{-1}$ )	$\alpha$	$23.6 \times 10^{-6}$	$10.25 \times 10^{-6}$	$53 \times 10^{-6}$
Specific heat $\left(\frac{J}{kg \cdot K}\right)$	c	892	460	1424
Emissivity	$\epsilon$	0.95	0.85	0.91

### 3.4.2 Boundary Conditions

Thermal and mechanical boundary conditions, based on the measurements obtained from the laboratory and physical properties of the model, were applied to the numerical model as follows:

- The initial temperature of the model was set as 22°C (ambient temperature).

- The motor shaft was heated directly with the heating pad. Accordingly, a surface temperature condition of 42°C was applied to the shaft surface.
- The convection heat transfer coefficient associated with the motion of the link was estimated to be  $7.75 \frac{W}{m^2 K}$  [40]. Convection was permitted for all free surfaces of the link.
- The duration of the analysis was one hour divided into 64 time steps. The maximum allowable temperature change for each of the 64 time increments was 1°C.
- Dynamic mechanical effects, such as inertia, were neglected.
- The centre node of one face of the motor shaft, at the proximal end, was fixed in all three directions to eliminate rigid body motion.

### 3.5 Results and Discussion

The results and discussion of the stationary case, which focused on heat distribution of the link without motion, are presented first. These results, including the temperature distributions and temperature-induced deformation, obtained from the experimental model are compared with the predictive results from the analytical model. Next, the results and discussion of the moving case, which focused on the effects of the motion in the experiment, are presented. The experimental results are compared with the predictive results from the FEA model.

Good agreement between the predictive and experimental results show that it is possible to predict temperature-induced deformation of the simple mechanical system. It is suggested that this prediction can then be used to compensate for the deformation during warm-up.

### 3.5.1 Stationary Case

Figure 3.7 shows a raw IR image obtained from the IR camera for a study of temperature distribution of the link. Note that the glowing patch on the left hand side is a heating pad that remained at high temperature in order to keep the temperature of the output shaft constant at approximately 36°C.

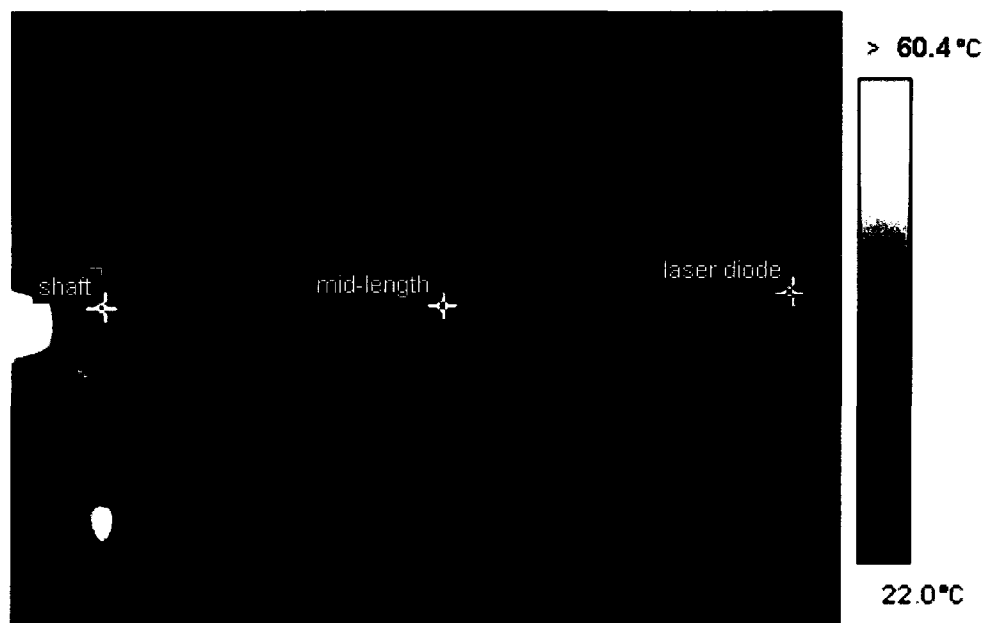


Figure 3.7: Temperature distribution at steady state of stationary case from experimental model.

The temperature of the locations of interest (as identified in Figure 3.7) and deformation results of the stationary case are plotted over a period of one hour, as presented in Figure 3.8. The time constant<sup>2</sup> was 660 s and the steady state<sup>3</sup> appears to be attained at 1,080 s. Exponential behaviour is observed in all temperature and deformation results in Figure 3.7. When comparing the temperature of the three locations, it was found that the link temperature was not linearly distributed along the link length. The temperature at the mid-length location was not an average of the temperature of the locations right

<sup>2</sup>The time constant being the time it takes to reach  $(e - 1)/e \simeq 63\%$  of steady state [41]

<sup>3</sup>Steady state means a standard deviation of  $\pm 3\sigma = \pm 15 \mu\text{m}$  [11]

above the shaft and the diode, but rather was only slightly higher than the temperature of the location right above the diode.

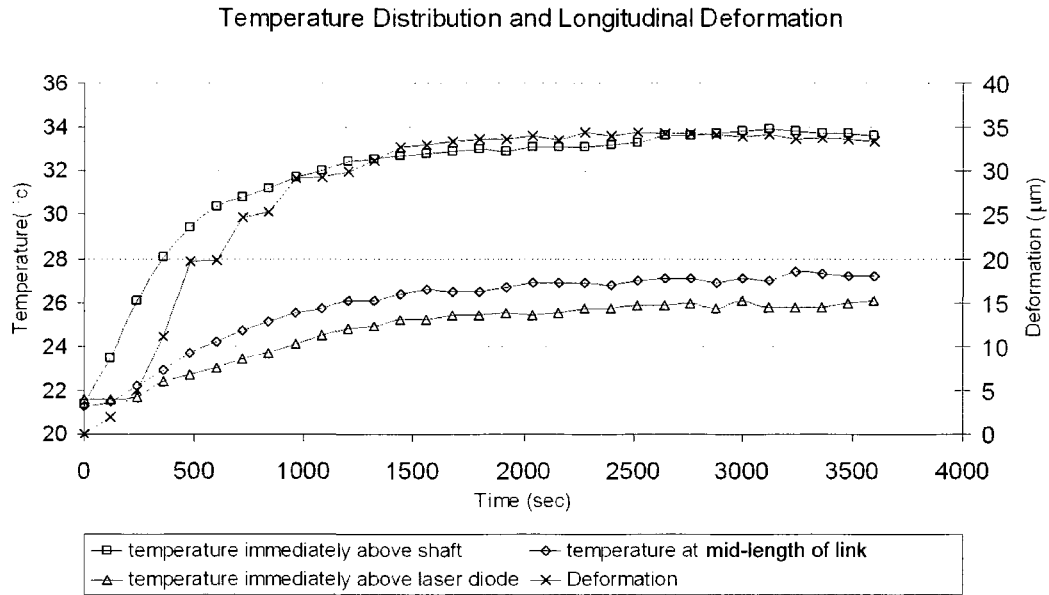


Figure 3.8: Temperature distribution and longitudinal deformation of stationary case.

Temperature distributions from the IR images were used in the analytical analysis to obtain the total longitudinal deformation of the link. The initial and final temperatures at the location right above the shaft were 22°C and 34°C respectively. Using Equation (3.7), the initial and final temperatures, and the material properties listed in Table 3.1, the total predicted predictive longitudinal deformation in the stationary case was obtained from the analytical model as described in Equation (3.7). The predictive and experimental results are listed in Table 3.2 and are in good agreement.

Table 3.2: Analytical and experimental total longitudinal deformation of stationary case.

	Deformation ( $\mu\text{m}$ )
Experimental	34.3
Analytical	33.2
% Difference	3.4

The agreement of the temperature distributions, as well as the temperature-induced deformation results, suggested the possibility of a development of a simple predictive control algorithm to compensate for temperature-induced deformation of a robot mechanical system. Given some knowledge of motor efficiencies, the analytical model could be used to predict the deformation in each link of the robot. The nominal robot dimensions could be adjusted to compensate for the induced end effector error. However, it is important to note that the stationary case was an over-simplification of virtually all robot workcell environments. Ultimately, the robot controller would require a complex algorithm incorporating multiple heat sources and their effects.

### 3.5.2 Moving Case

The temperature distribution of the link at steady state recorded during the experiment for the moving case is presented in Figure 3.9<sup>4</sup>. The temperature at the location right above the laser diode was 28.2°C and the temperature at the location right above the motor shaft was 36.6°C. Note that the temperature of the laser diode, which had a low thermal conductivity, remained at room temperature throughout the experiment, as expected.

Figure 3.10 shows the temperature history predicted by the transient FEA for the nodes right above the laser diode and right above the motor shaft. The experimental steady state results are also superimposed on the figure. There was a good agreement between the FEA and experimental results at steady state. The node above the motor shaft reached steady state sooner than the node above the laser diode.

A fringe plot of the steady state thermal distribution predicted by the FEA is shown in Figure 3.11. As expected, the temperature changed smoothly over the length of the link, as a function of distance from the motor shaft. Steady state occurred at approximately 1,800 s

---

<sup>4</sup>In Figure 3.9, a slightly different scale was assigned to in the fringe plot that was used in Figure 3.7. Note that the temperatures in Figure 3.9 are slightly higher than in Figure 3.7.



Figure 3.9: Temperature distribution at steady state of moving case.

for the node immediately above the laser diode. Figure 3.12 illustrates the longitudinal deformation predicted at steady state by the FEA (shown in red) is superimposed on the undeformed link (shown in green).

Figure 3.13 shows the experimentally-measured longitudinal deformation of the location right above the laser diode, as compared to the deformation of the corresponding node predicted by the FEA. The total deformation of both experimental and FEA results from Figure 3.13 are summarized and compared in Table 3.3. Both Figure 3.13 and Table 3.3 indicate, in this case, that the FEA when compared to the experiment, generally over predicts the temperature-induced deformation. The rise time of FEA results is approximately 500 s shorter than that of the experimental results, which resulted in a higher slope of deformation versus time during transient state compared to the experimental results, as seen in Figure 3.13. At steady state, the difference in the deformation was approximately 3.5%, which suggested that the steady state temperature-induced deformation in the moving case could be predicted with the same level of accuracy as that of the stationary case.

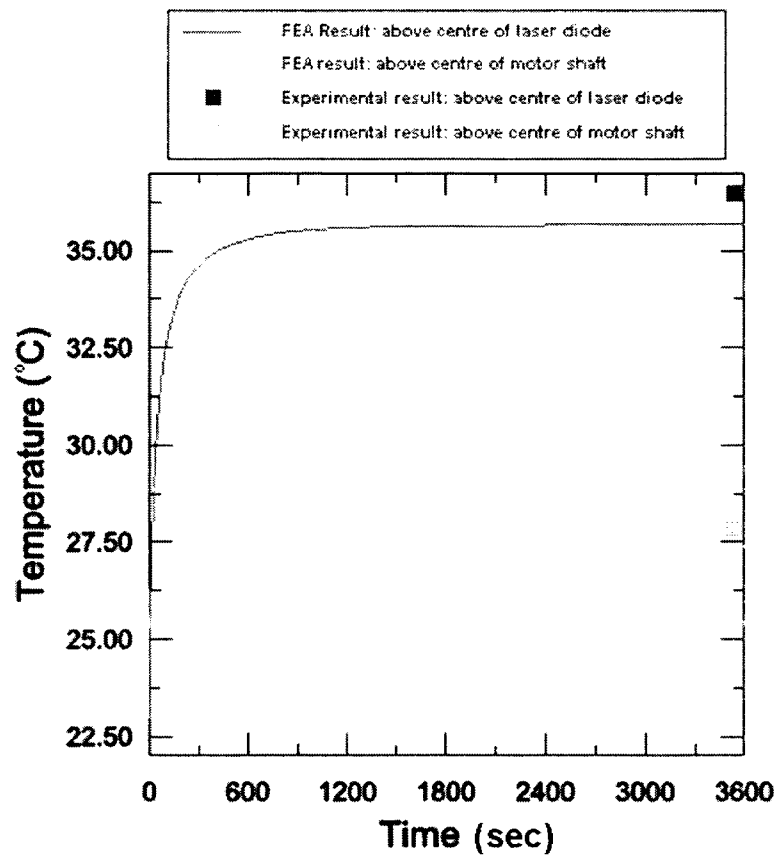


Figure 3.10: Temperature of two node locations over 3,600 s of moving case.

This was an unexpected result and, in this instance, with the relatively simple nature of FEA model and its boundary conditions; *i.e.*, essentially 1-D thermal analysis with conduction and convection driving a 1-D mechanical analysis with thermal strain, made the experiment suspect.

Table 3.3: Numerical and experimental longitudinal deformation of moving case.

	Deformation ( $\mu\text{m}$ )
Experimental	45.2
Numerical	46.8
% Difference	3.5

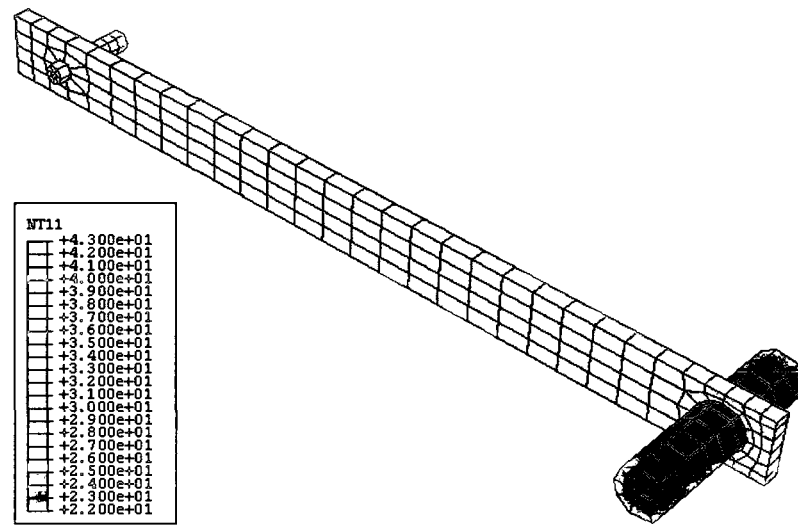


Figure 3.11: Thermal distribution ( $^{\circ}\text{C}$ ) at steady state of moving case predicted by the FEA.

While, in general, reasonable agreement was also found in the moving case between the experimental results and the predicted FEA results, it is important to identify the cause of the difference between rise times of the experimental and FEA results observed in Figure 3.13.

Although the results suggested a potential for the development of a simple predictive control algorithm to compensate for temperature-induced deformation, and reducing or

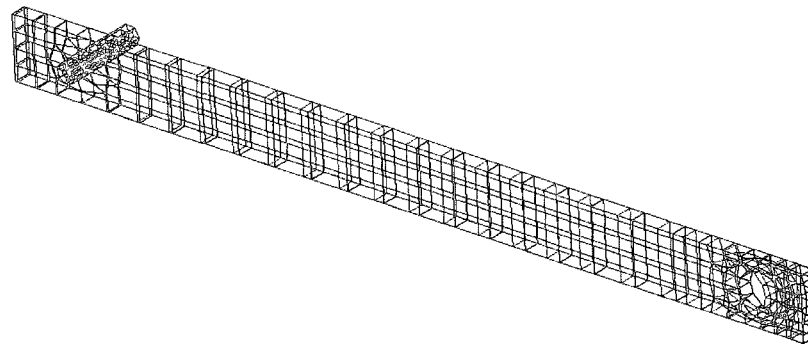


Figure 3.12: Longitudinal deformation ( $\times 100$ ) superimposed on undeformed link at steady state of moving case.

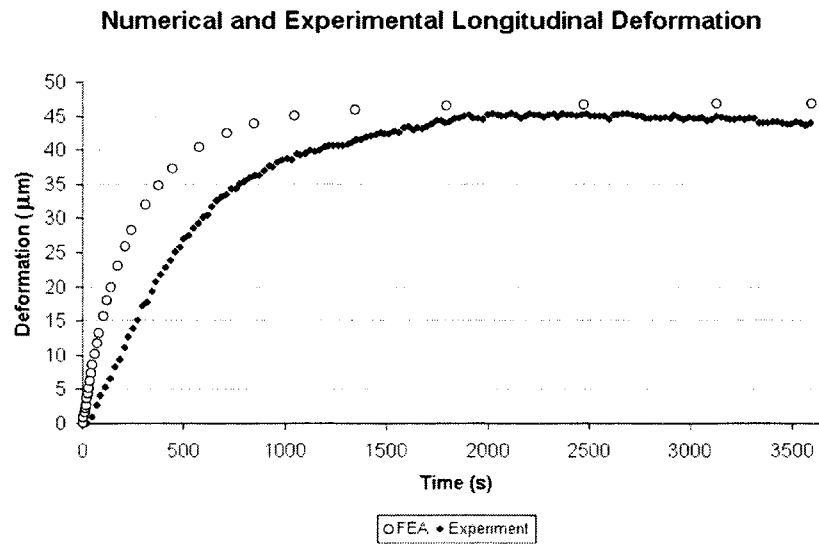


Figure 3.13: Longitudinal deformation of FEA and experimental results immediately above laser diode of moving case.

eliminating warm-up cycle times in industrial robots, some difficulty was experienced during the experiments, particularly in the moving case which indicated that the experimental results were in fact under-predicted. Unexpected errors had been noted in the results from several trials and extra attempts were made in order to obtain suitable results for the analyses. As some significant errors were detected (shown in Figure 3.13), further investigation was required for all models to verify their results, and to identify sources of error. The investigation started with the measurement system of the experimental model. A study on efficiency and improvement of the deformation measurement system is presented in Chapter 4.

Finally, while there was no intention to implement any FEA approach model in the robot controller, an implementation of the analytical model incorporating the convection coefficient (*e.g.*, Equation (3.3)) in the robot controller was pursued. A finite difference model extended from an analytical model and the concepts of thermal resistance and capacitance [40] was used in a study of a two-link system (see Chapter 5), and its results were further used as input data for a compensation algorithm (see Chapter 6).

# Chapter 4

## Investigation, Modification and Improvement of the Dimensional Deformation Measurement System

### 4.1 Introduction

In Chapter 3, experimental results, as well as numerical (FEA) and analytical models of the single-link system were presented. While the thermal results showed good agreement between the experimental (measured) and FEA (predicted) results at steady state, this was not the case for the longitudinal deformation results. As seen in Figure 3.13, two significant differences were observed in the temperature-induced longitudinal deformation between the FEA and experimental results for the moving case. First, the FEA results reached steady state faster. Second, the FEA showed a larger (3.5%) steady state deformation compared to the experimental results. It was unclear whether these differences were caused by the experimental apparatus and/or procedures, by assumptions made in the FEA (*e.g.*, boundary conditions), or both. Further studies of both the experimental and FEA models

were required to explain the differences detected. Given that the measurement system of the experimental model was manually assembled, the results of the experimental model were expected to be much more prone to error than those of the relatively straight-forward FEA model.

The objective of this chapter is to consider the experimental model in terms of potential sources of errors. The sources related to the experimental model included the physical apparatus, experimental procedures and measurement resolution. The FEA model will be considered in Chapter 5.

## 4.2 Evaluation of the Experimental Models

An examination of the experimental setup identified potential sources of error related to four main components of the experimental model: the slender link, the robot, the CCD camera and the deformation measurement system. Potential sources of error are listed in Table 4.1. Those related to the link were bending, linkage alignment, and dimensional deformation of the diode hole in the link. With respect to the robot, idle-induced vibration, which could perturb the link-diode assembly, was considered. In terms of the measurement system, the accuracy of estimating coordinates of the laser spot through the centroid extraction algorithm, concerns about laser spot size, and temperature-induced deformation of the mounting plate of the camera stand, were considered. Finally, the heating pad was considered.

For each potential source of error listed in Table 4.1, at least one of the analytical, numerical or experimental results was available for the evaluation of the impact of the error on the measurement results.

The variable used to represent additional deformation caused by the errors is  $\delta L$ . Its components on the  $x$ -axis (longitudinal) and  $y$ -axis (transverse) directions are  $\delta L_x$  and  $\delta L_y$

Table 4.1: Potential sources of error and types of available results.

Potential sources of error	Results		
	analytical	experimental	numerical
Effects of cantilever bending	✓	—	—
Effects of link alignment	✓	—	—
Expansion of diode hole	✓	—	✓
Idle-induced vibration of robot	—	✓	—
Accuracy of centroid extraction algorithm	—	✓	—
Thermal effects of CCD camera	—	✓	—
Flexibility of heating pad	—	✓	—

respectively.  $\Delta L$  is an actual temperature-induced deformation of the system (assuming no error).  $\Delta L_x$  and  $\Delta L_y$  are the  $x$ -axis and  $y$ -axis components of the temperature-induced deformation respectively. Note that the  $x$ -axis is positive in the direction of longitudinal expansion, and the  $y$ -axis is positive in the upward direction.

For a finely tuned measurement system, one should expect  $\delta L \ll \Delta L$ . To justify whether each potential source of error had an impact on the measurement results,  $\delta L_x$  obtained from analysis was compared to an expected  $\Delta L_x$  of  $45 \mu\text{m}$ , which is the average value of the expected steady state temperature-induced deformation resulting from the single-link experiment [10] described in Chapter 3. As the small deformation theory is applied, the undeformed and deformed configurations of the body can be assumed identical [51].

### 4.3 Effects of Cantilever Bending

The slender link of the single-link experiment had a length-to-width ratio greater than ten, *i.e.*, the length was 292.0 mm and the width was 25.4 mm. The link was assumed to be well fastened by two setscrews to the output shaft at one end<sup>1</sup>. The other end of the link was a free end to which the laser diode was attached. Typically, in a cantilever of this size, deflection of the free end would not be a factor, since the beam (link) was oriented in such a way as to be fully self-supporting. However, as the temperature-induced deformation of the link occurred on such a small scale, even a very small bending could contribute to the difference of the two deformation results observed in Figure 3.12 of Chapter 3. Therefore, the deflection at the free end due to cantilever bending was determined using a standard equation for small deformation bending. To examine the worst case, *i.e.* maximum downward deflection, the combined weight of the link and the diode was applied at the free end. An analytical analysis to obtain the maximum deflection of the link due to the cantilever bending is presented in Section 4.3.1.

#### 4.3.1 Analytical Analysis of the Effects of Cantilever Bending

Assuming that the link deflects at the free end, as illustrated in Figure 4.1,  $\delta L_y$  can be modelled as:

$$\delta L_y = \frac{-FL^3}{3EI}, \quad (4.1)$$

where:

$F$  is the weight of link and diode (*i.e.*,  $W_{link + diode}$ ),

$L$  is the effective length of the link (the distance between the centre of the shaft hole and the centre of the diode hole),

---

<sup>1</sup>For this experimental setup, setscrews were proven to provide adequate strength to fasten the link to the shaft without damaging the contact surface.

$I$  is  $\frac{bh^3}{12}$  (where  $b$  is the thickness of the link and  $h$  is the width of the link),  
 $E$  is Young's Modulus of the material.

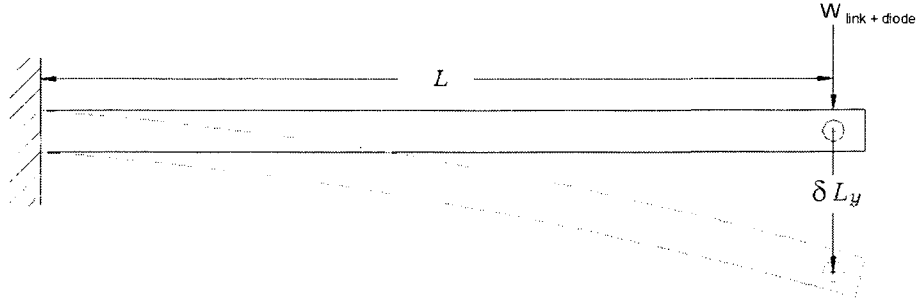
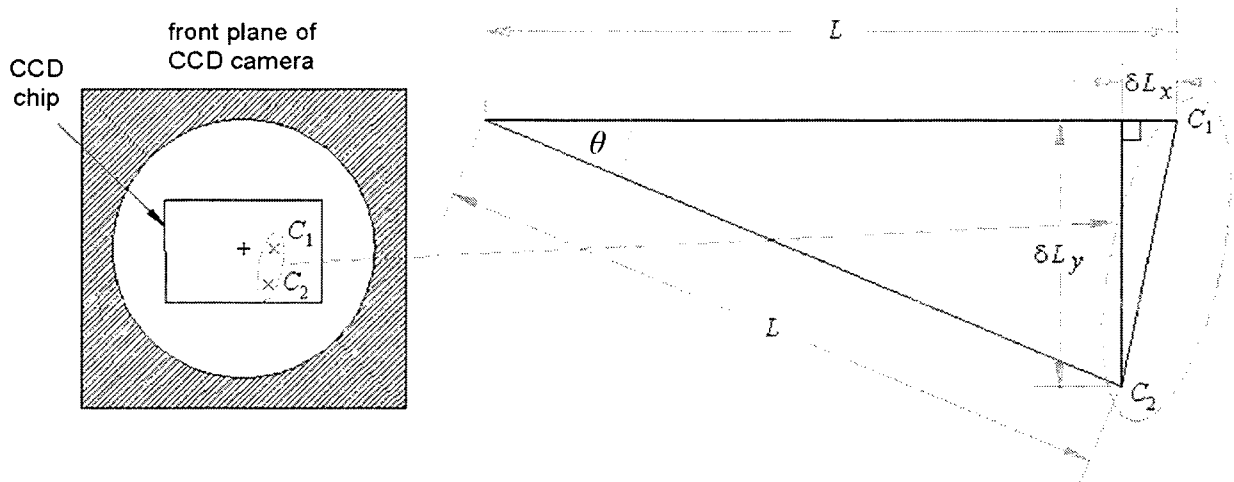


Figure 4.1: Static deformation.

### 4.3.2 Results and Discussion

The effective length of the link,  $L$ , was 292.0 mm. Using the small deformation theory,  $L$  remained constant after bending occurred. The combined weight of the link and diode was 0.2 kg. The cross-sectional dimensions  $b$  and  $h$  were 6.4 mm and 25.4 mm respectively. Young's modulus for 6061 Al was 70 MPa. Using Equation (4.1), the maximum deflection at the free end,  $\delta L_y$ , was  $27 \mu\text{m}$ . The values for  $\delta L_y$  and  $L$  show that  $\delta L_x$  was  $0.0012 \mu\text{m}$ .

The maximum value of  $\delta L_x$  was at least 3 orders of magnitude smaller than the expected temperature-induced deformation,  $\Delta L_x$ . Therefore, even in the worst case scenario, when the system had the maximum downward deflection,  $\delta L_x$  was still too small to significantly affect the value of  $\Delta L_x$ . Conversely, the value of  $\delta L_y$  that would make the value of  $\delta L_x$  become significant was  $170 \mu\text{m}$ . This value of  $\delta L_y$  was more than 10 times greater than the calculated  $\delta L_y$ . Hence, any potential effects from cantilever bending were considered to be insignificant and negligible.

Figure 4.2:  $\delta L_x$  and  $\delta L_y$ .

## 4.4 Effects of Link Alignment

The dimensions of the slender link of the single-link system were chosen so that temperature-induced deformation in the longitudinal direction would dominate, *i.e.*,  $\Delta L_x = \Delta L$ .  $\Delta L_y$  was assumed to be small by comparison, and therefore negligible. However, any misalignment of the slender link could cause the expected one-dimensional (longitudinal) deformation to be detected on the CCD camera as a two-dimensional deformation. Such a misalignment may be caused by the error in the installation of the link in the apparatus and/or the inaccuracy of dimensions of the link (due to machining resolution). Analytical analyses of the effects of the misalignment about the  $z$ -,  $y$ - and  $x$ - axes are presented in Section 4.4.1. The reference axes directions are shown in Figure 4.3.

### 4.4.1 Analytical Analysis of the Effects of Link Alignment

Misalignment of the link was considered for each of the three axes independently. In each case, it was assumed that the misalignment was in one direction only and there was no misalignment along the other two axes for the specific case considered.

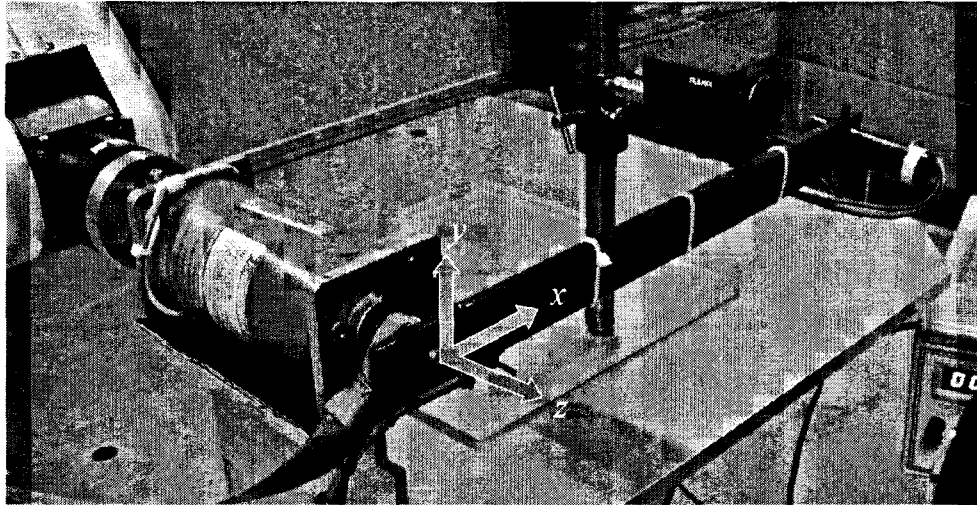
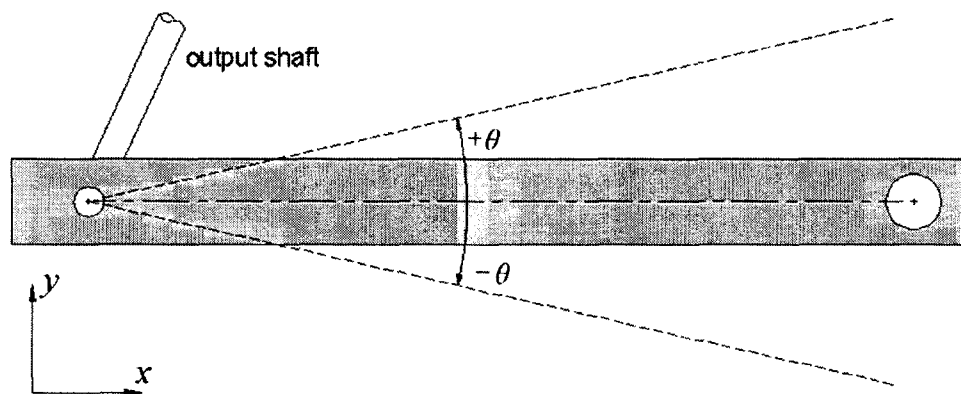


Figure 4.3: Link and axes definition.

### Misalignment about the $z$ -Axis

Misalignment about the  $z$ -axis due to the link installation on the output shaft occurs when the link is not perfectly parallel to the horizontal plane (see Figure 4.4). The resulting misalignment about the output shaft contributes to an error in the measurement of the longitudinal deformation. As shown in Figure 4.4, when the link is misaligned, it is rotated about the centre line of the output shaft by an angle  $\theta$ .

Figure 4.4: Link alignment showing misalignment  $\theta$ .

For example, when the link is rotated counterclockwise from the starting position by

the angle of  $\theta$ , the actual temperature-induced deformation,  $\Delta L$ , is not parallel to the longitudinal  $x$ - axis (assuming the CCD chip plan is parallel to the  $xy$ -plane), as shown in Figure 4.5. Instead of being detected by the CCD camera as a deformation in the direction of the  $x$ -axis,  $\Delta L$  is detected as a deformation in both the  $x$ - and  $y$ -axes, where  $C_1$  is the location of the centroid of the laser spot at the start and  $C_2$  is the location at steady state. The magnitudes of the two components in the  $x$ - and  $y$ -axes of the deformation are  $|\Delta L_x| = |\Delta L \cos \theta|$  and  $|\Delta L_y| = |\Delta L \sin \theta|$ . Hence, magnitude of  $\delta L_x$  depends on the magnitude of  $\Delta L$  and the angle  $\theta$ , and can be expressed as  $\delta L_x = \Delta L(1 - \cos \theta)$ .

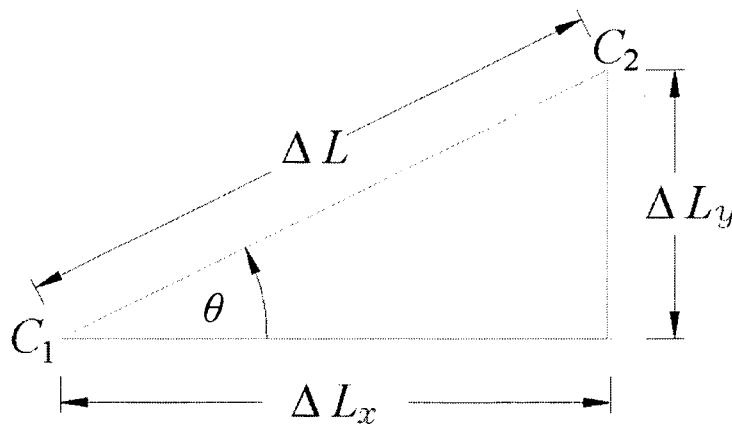


Figure 4.5: Actual and measured  $\Delta L$  due to misalignment about  $z$ -axis.

The variation in link misalignment about the  $z$ -axis due to mechanical play was found to be  $\pm 0.2^\circ$ . This range is listed with those of the other two axes in Table 4.2.

### Misalignment about the $y$ -Axis

Figure 4.6 illustrates the misalignment of the link about the  $y$ -axis, when viewed from above. The laser diode is assumed to be mounted perfectly perpendicular to the link. When the link is not parallel to the plane of the CCD chip, the laser beam from the laser diode does not point perpendicular to the CCD chip plane. The longitudinal deformation of the link detected by the CCD camera is a projection of the deformation on an incline

plane. Thus, misalignment about the  $y$ -axis only affects  $\Delta L_x$ .

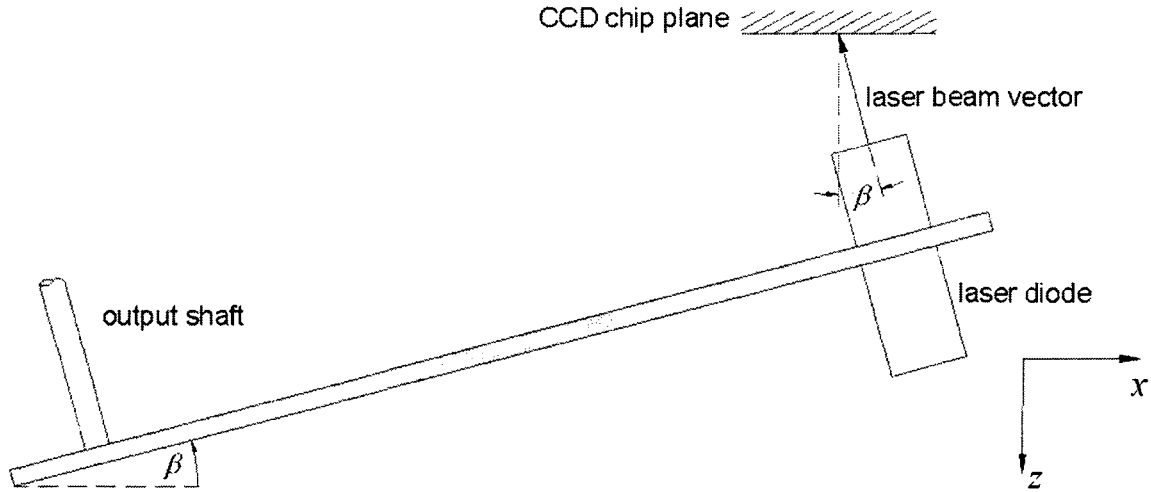


Figure 4.6: Link alignment showing misalignment  $\beta$ .

As shown in Figure 4.7, with the misalignment about the  $y$ -axis, the actual deformation,  $\Delta L$ , is extracted from CCD camera images as  $\Delta L_x$  on the CCD chip plane, which is tilted from the direction of the deformation by the angle of  $\beta$ . Note that  $C_1$  and  $C_2$  are the locations of the centroid of the laser spot at the start and at steady state, respectively. The extra deformation caused by the misalignment,  $\delta L_x$ , is the difference between magnitudes of  $\Delta L$  and  $\Delta L_x$ . Hence, magnitude of  $\delta L_x$  depends on the magnitude of  $\Delta L$  and the angle  $\beta$ , and can be expressed as  $\delta L_x = \Delta L \left(1 - \frac{1}{\cos \beta}\right)$ .

The variation in link misalignment about the  $y$ -axis due to mechanical play was found to be  $\pm 0.1^\circ$ .

### Misalignment about the $x$ -Axis

Figure 4.8 shows the experimental setup as viewed from the diode side. When the front plane of the link is tilted up or down about the  $x$ -axis by the angle  $\gamma$ , the laser beam is rotated away from the perpendicular direction to the CCD plane by the same angle  $\gamma$ . The variation in link misalignment about the  $x$ -axis due to mechanical play was found to

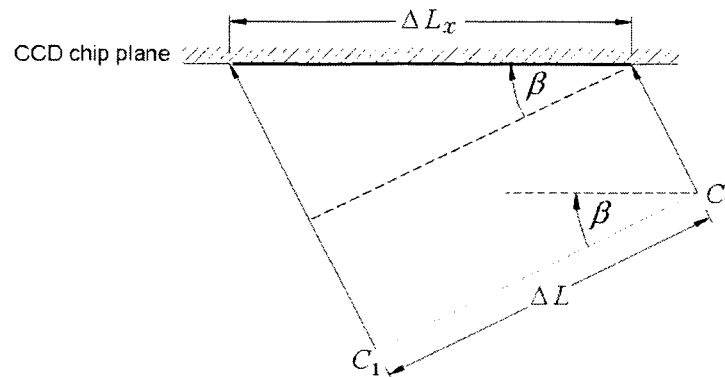


Figure 4.7:  $\Delta L$  and  $\Delta L_x$  due to misalignment about  $y$ -axis.

be  $\pm 0.4^\circ$ .

However, misalignment about the  $x$ -axis only affects the location of the centroid of the laser beam in the vertical direction. Given the assumption that there was no misalignment on the other two axes, the angle  $\gamma$  does not affect the measurement of  $\Delta L_x$ .

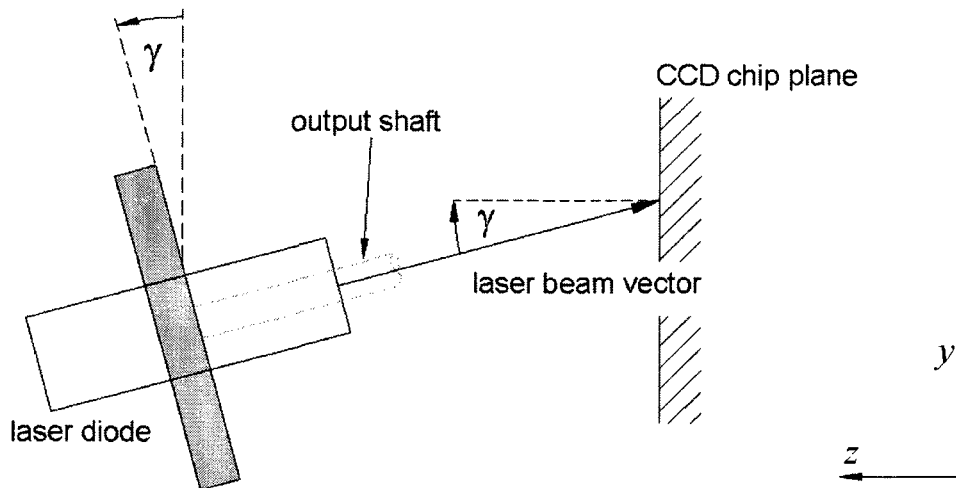


Figure 4.8: Link alignment about  $x$ -axis.

#### 4.4.2 Results and Discussion

Table 4.2 shows the variations of link misalignment due to mechanical play. The ranges imply that the magnitudes of  $\theta$  and  $\beta$  could be as large as  $0.2^\circ$  and  $0.1^\circ$  respectively.

Although the magnitude of  $\gamma$  can be as high as  $0.4^\circ$ , it has been found that misalignment about the  $x$ -axis does not affect the measurement of  $\Delta L_x$ .

Using the largest angle of misalignment described in Table 4.2, the maximum difference between actual and measured deformation,  $\delta L_x$ , due to misalignment about the  $z$ -axis, would be  $2.75 \times 10^{-10}$  m; misalignment about the  $y$ -axis would be  $6.88 \times 10^{-11}$  m; and the combination of misalignment about the  $y$ - and  $x$ -axes would also be  $6.88 \times 10^{-11}$  m. Note that, as mentioned in Section 4.2, the value of the measured deformation used in this calculation is  $\Delta L_x = 45 \mu\text{m}$ .

The misalignment about the  $z$ -axis had the biggest impact on the value of the measured longitudinal deformation; however, the value of  $\delta L_x$  was still more than 3 orders of magnitude smaller than the expected  $\Delta L_x$ . Therefore, link misalignment about any particular axis, or combinations of any axes, was considered to be insignificant. Note that any misalignment with greater angles than those presented in Table 4.2 is expected to be detected and corrected on a regular basis and prior to all experiments. As indicated in Table 4.1, only analytical results are presented for this potential source of error.

## 4.5 Expansion of Diode Hole

Naturally, during the restrained thermal expansion, every dimension of the link changes linearly by the same percentage including holes diameters. The change in dimension of

Table 4.2: Variation in link misalignment due to mechanical play.

Axis of Misalignment	Symbol	Angle( $^\circ$ )
$x$	$\gamma$	$\pm 0.4$
$y$	$\beta$	$\pm 0.1$
$z$	$\theta$	$\pm 0.2$

the hole diameter would be different from that of the laser diode diameter because of the difference in material properties. From the results of the single-link experiment, it was found that the ABS laser diode, which had low thermal conductivity, remained at room temperature throughout the experiment. Although the coefficient of thermal expansion of the ABS diode ( $\alpha = 53 \times 10^{-6} K^{-1}$ ) was higher than that of the aluminum link, the expansion in the diameter of the diode was still expected to be smaller than that of the hole, as the change in temperature of the ABS diode case was much smaller.

The hole in the link was sized to fit the laser diode snugly, and a setscrew was used to fix the diode in place. It was observed during the experiment that the diode became loosened, which implied the expansion of the diode hole. When the hole expanded, the resulting play might have enabled the diode to move and become misaligned. Two possible motions of the diode were dropping straight down and tilting. Both cases were examined analytically and numerically. It was assumed, for these analyses that there was no effect of link misalignment.

#### 4.5.1 Analytical Analysis of Diode Hole Expansion

The nominal dimensions of the link at the diode end are shown in Figure 4.9. The deformed shape of the link, due to the temperature-induced deformation (expansion), is superimposed on the dimension of the link. An increase in the hole diameter from the expansion can be expressed as  $\delta L = \alpha L |T_i - T_o|$ .

When the diode hole expands sufficiently, the laser may become loose and move. A change in location of the diode is detected through the change in location of the laser spot centroid acquired by the CCD camera. If the diode drops straight down or tilts vertically, only the magnitude of  $\delta L_y$  is affected. If the diode tilts side to side, only the magnitude of  $\delta L_x$  is affected. Both magnitudes of  $\delta L_x$  and  $\delta L_y$  are affected when the diode tilts in any direction other than vertical or horizontal.

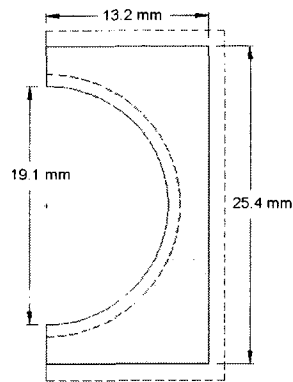


Figure 4.9: Dimension of link at diode end (dimension of the expanded link shown in dashed lines are not to scale).

When the hole expands and the diode drops down without tipping, the diode will rest at the bottom of the hole, as illustrated in Figure 4.10.  $D_1$  is the centre of the hole and the centroid of the laser spot at the start.  $D_2$  is the centroid of the laser spot when the diode is resting at the bottom of the expanded hole at steady state.  $\delta L_y$  is the change in centroid location in the vertical direction of the laser spot, which was extracted from images acquired by the CCD camera. When the diode drops straight down, only  $\delta L_y$  is expected, and the measurement of  $\Delta L_x$  is not affected by this motion of the diode.

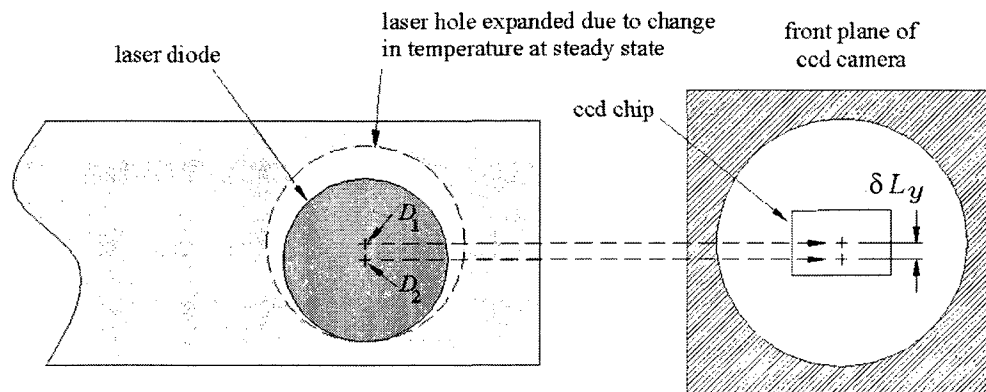


Figure 4.10: Diode dropping straight down.

When the hole expands, the diode may easily tilt because the thickness of the link is very small relative to the through-thickness length of the diode. The diode may tilt in pure

vertical (up-down) or horizontal (left-right) directions, or a direction that is a combination of both.

Figure 4.11 shows the experimental setup as viewed from the cross-section of the link at the laser diode when the diode is tilting in a pure vertical direction. When the diode tilts, the direction of the laser beam is no longer perpendicular to the CCD chip plane. Similar to the misalignment about the  $x$ -axis, described in Section 4.4, the tilt angle of the laser beam in the vertical direction only affects the location of the centroid of the laser spot in the  $y$ -axis direction. Hence, the measurement of  $\Delta L_x$  is not affected.

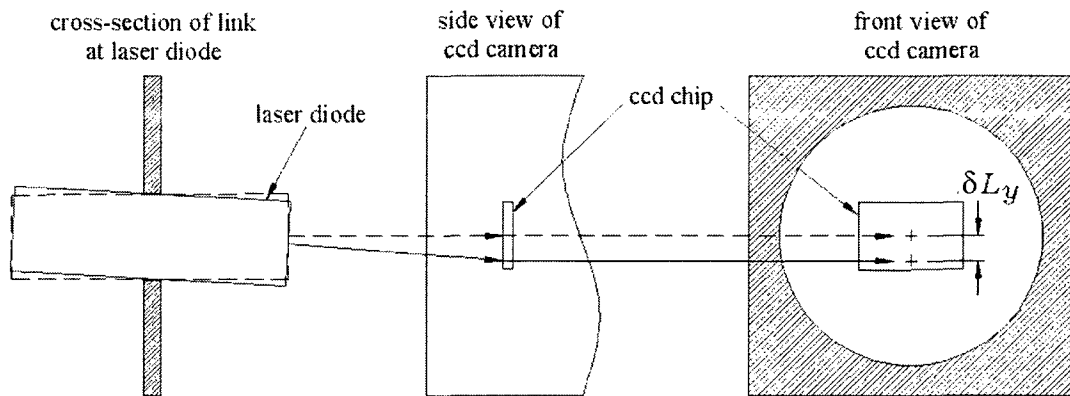


Figure 4.11: Diode tilting vertically.

When the diode tilts in the horizontal direction, and in combined directions of horizontal and vertical, as opposed to purely vertical, the measurement of  $\Delta L_x$  is then affected in a similar manner to the misalignment about the  $y$ -axis and the  $z$ -axis (Section 4.4).

### 4.5.2 Numerical Analysis of Diode Hole Expansion

Temperature results obtained from the FEA model for the moving case of the single-link experiment were used here. The temperature histories of the node immediately above the laser diode, the node at the centre of the shaft, and the node at the centre of the laser diode, were extracted from the results. For convenience, the change in temperature of

the node immediately above the laser diode was used to calculate the expansion of the diameter of the diode hole.

The temperature distribution of the link was studied to verify behaviour of heat conduction within the link. The temperature history of the nodes at the centre of the shaft was observed to confirm a constant heat input over the period of the experiment. Similarly, the temperature history of the node at the laser diode was observed to confirm the constant temperature of the laser diode.

### 4.5.3 Results and Discussion

#### Analytical Results

The diameter of the laser diode hole in the link was 19 mm. The coefficient of thermal expansion of the 6061 Al link was  $23.6 \times 10^{-6} \text{ (K}^{-1}\text{)}$ . As noted from the experimental results of the single-link system, presented in Chapter 3, the initial and steady state temperatures of the link at the location of the node immediately above the laser diode were 22°C and 28.2°C, respectively. Using the equation for thermal expansion, the change in the diameter of the diode hole was found to be 2.79  $\mu\text{m}$ .

Figure 4.12 shows the top view of a tilt angle,  $\alpha$ , of the the laser diode when the hole has expanded. From the geometry of the diode and the hole, the maximum tilt angle in any direction around the circumference of the hole can be obtained from the following relations:  $\tan \alpha = \frac{b-x}{a}$  and  $\cos \alpha = \frac{c}{b+x}$ . Solving these equations simultaneously yields:

$$\alpha = \arctan 2 \left( \frac{2(2cb \pm \sqrt{4b^2a^2 + a^4 - a^2c^2})b}{4b^2 + a^2} - c, \frac{2cb \pm \sqrt{4b^2a^2 + a^4 - a^2c^2}}{4b^2 + a^2} \right) \quad (4.2)$$

$$x = -\frac{\left(\frac{(2cb \pm \sqrt{4b^2a^2 + a^4 - a^2c^2})b}{4b^2 + a^2} - c\right)(4b^2 + a^2)}{2cb \pm \sqrt{4b^2a^2 + a^4 - a^2c^2}}. \quad (4.3)$$

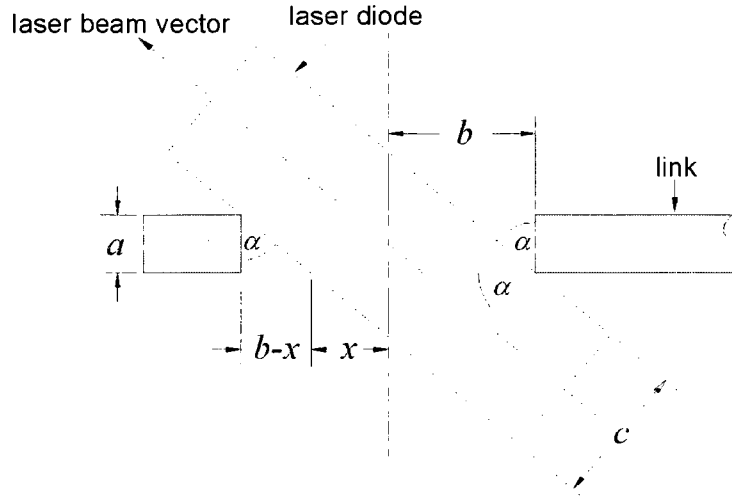


Figure 4.12: Tilt angle,  $\alpha$ , due to hole expansion (hole size is exaggerated for illustrative purposes).

For the variables illustrated in Figure 4.12, the thickness of the link was  $a = 6.4$  mm, the diameter of the expanded hole was  $2b = 19.1$  mm, and the diameter of the diode was  $c = 19.0$  mm. Using Equation (4.2), the maximum tilt angle was  $0.88^\circ$ .

As seen in Figure 4.13, the distance between the centre of the link width and the CCD chip plane was 75 mm. Using the value of the maximum tilt angle and Equation (4.3), the maximum  $\delta L_x$  due to laser diode tilting was  $1.15 \mu\text{m}$ .

## Numerical Results

The temperature distribution of the apparatus at steady state, as predicted by the FEA model, is shown in Figure 4.14. A smooth temperature gradient over the length of the link, as a function of distance away from the output shaft, is observed. The temperature

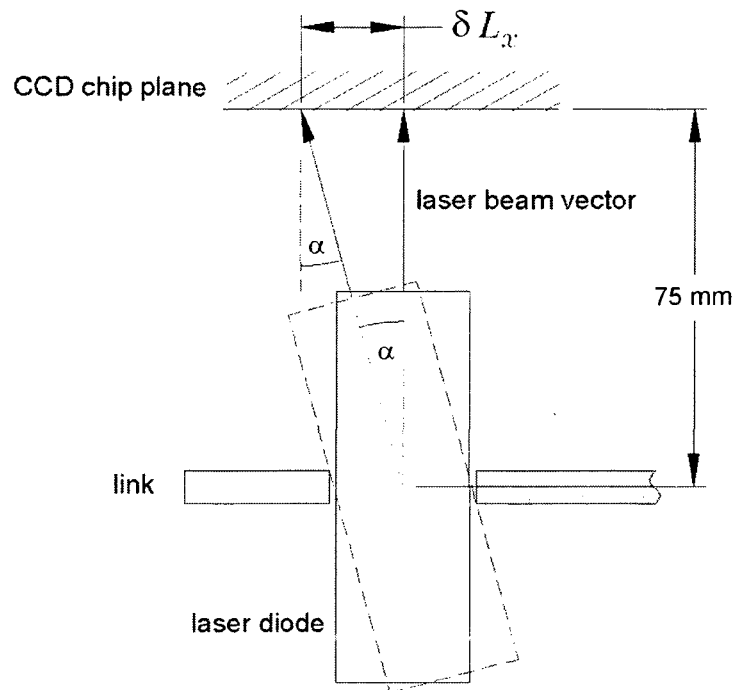


Figure 4.13:  $\delta L_x$  due to tilting of laser diode (hole expansion is exaggerated for illustrative purposes).

of the diode remained constant at room temperature throughout the experiment.

Figure 4.15a illustrates that the temperature at the steady state of the node immediately above the laser diode was  $28.08^\circ\text{C}$ . Figure 4.15b shows that the deformation in the radial direction at the same node was  $1.26\ \mu\text{m}$ , corresponding to a change in the diameter of the diode hole of  $2.53\ \mu\text{m}$ .

Considering the temperature of the link at the location immediately above the laser diode and the temperature of the laser diode, there was good agreement between the FEA results and the experimental results. The temperature of the link at the location immediately above the laser diode was found to be  $28.2^\circ\text{C}$  from the experimental results, and  $28.08^\circ\text{C}$  from the FEA results. The temperature of the laser diode remained constant at room temperature throughout the whole experiment for both experimental and FEA results.

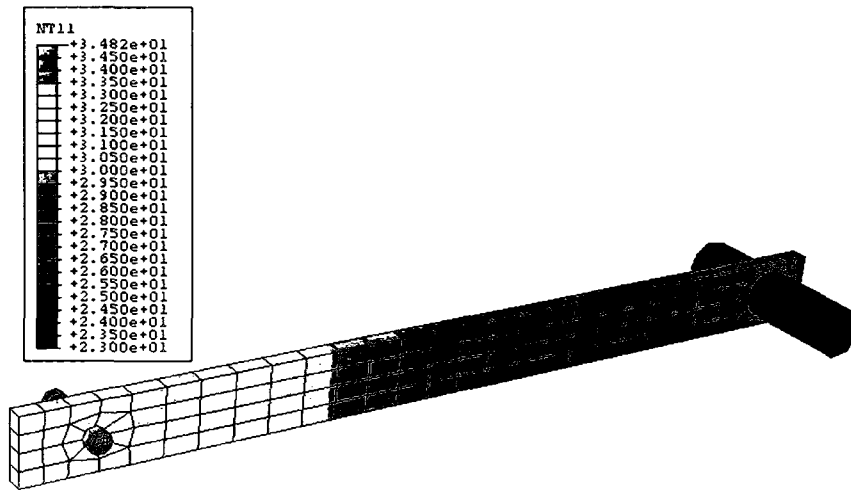


Figure 4.14: Temperature distribution ( $^{\circ}\text{C}$ ) at steady state from FEA of single-link model.

### Discussion

The constant temperature of the diode and the expansion of the diode hole indicate that the dimensions of the laser diode are not affected by temperature-induced deformation. However, the dimension of the diode hole is affected through heat conduction along the link. Therefore, the accuracy of the deformation measurement may be reduced due to the motion(s) of the diode when the hole expands and no longer snugly fits the diode. With

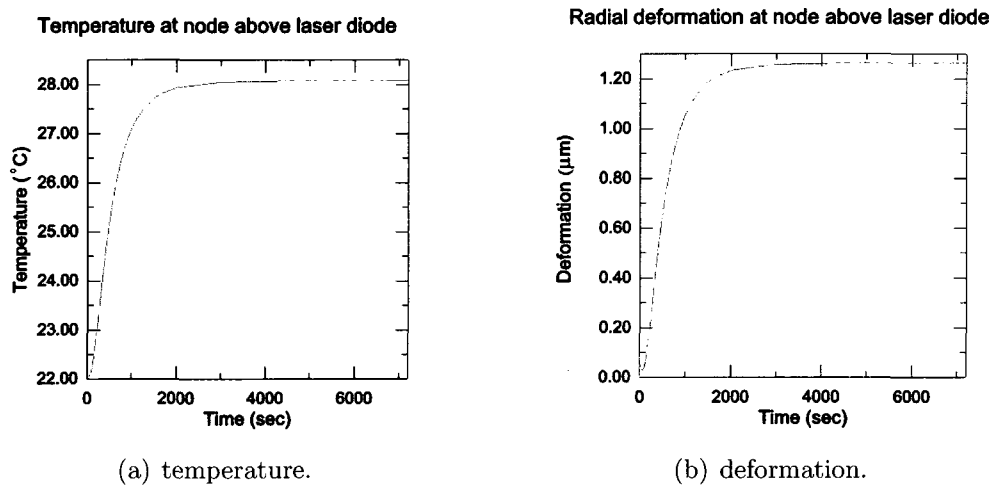


Figure 4.15: Temperature and deformation at node above laser diode.

the resulting play, the diode may tilt in various directions when physically disturbed.

The maximum value of  $\delta L_x$  was approximately 65% to 80% of  $\Delta L_x$ . This large percentage indicates that when the diode was tilted in a pure horizontal direction, or a combined direction with a large portion of horizontal component, the error in the measurement may become unacceptably large, and the measured value cannot be used.

This analysis clearly demonstrates that the setup requires an isolation method to ensure the diode is not physically disturbed throughout the course of the experiment. In the stationary case experiment, the diode cable must be arranged so that the weight of the cable does not cause a tension in the cable that may result in diode tilting. In the moving case experiment, sufficient slack in the diode cable and a clear path for the cable must be provided. The setscrew that fastened the laser diode to the link must also be tightened prior to each experiment.

## 4.6 Idle-Induced Robot Vibration

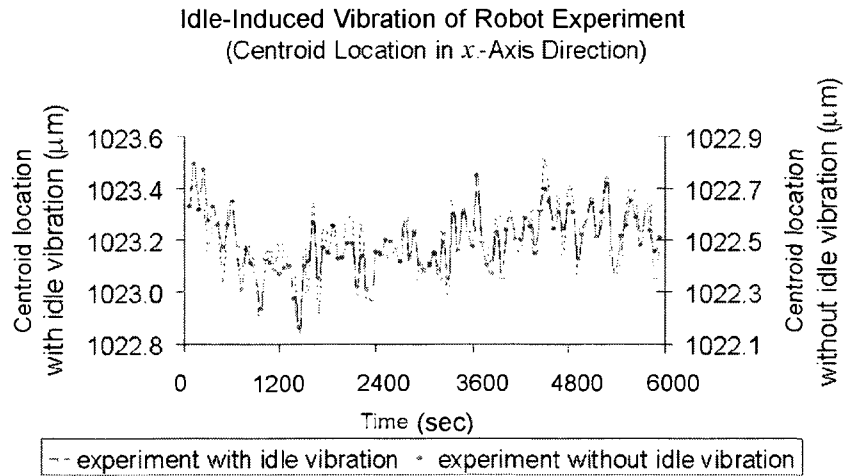
In the single-link experiment, the link was well fastened to the output shaft, which, in turn, was rigidly fastened to the robot tool flange via an aluminum coupling. The shaft and the link were considered a rigid body in the stationary experiment because the link was assigned to remain at the same location throughout the experiment. The experimental results showed a consistent trend of low amplitude oscillation of the centroid of the laser spot in the  $y$ -axis (transverse) direction. The oscillation was likely caused by vibration of the robot while it was powered on and idling. This idle-induced vibration must be considered as a source of experimental error.

### 4.6.1 Experimental Analysis of the Idle-Induced Robot Vibration

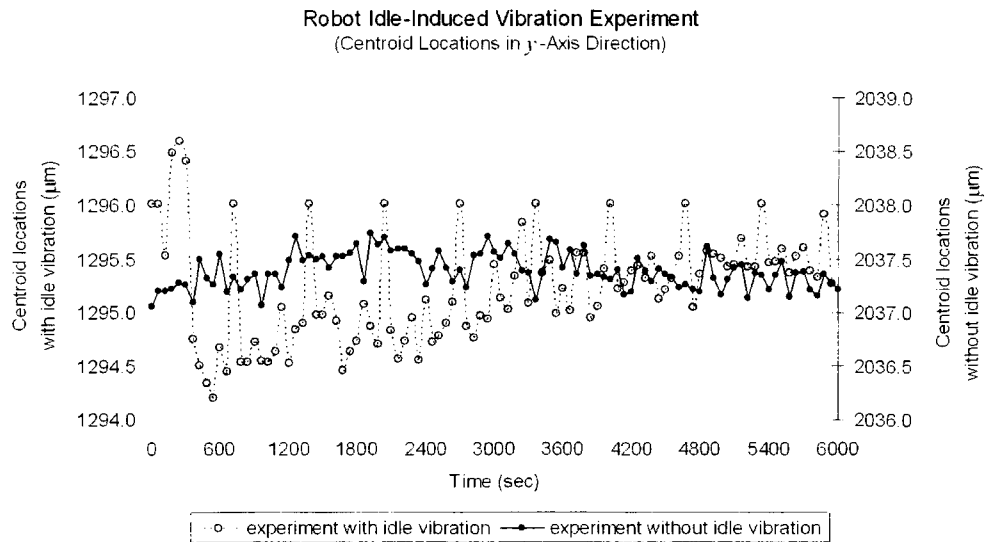
To isolate the effects of the idle-induced vibration of the robot from the single-link system, the system setup needed to be decoupled from the robot. Accordingly, the output shaft of the system was disconnected from the coupling. The link assembly (*i.e.*, the link fastened to the shaft) was then fastened directly to a workbench to minimize the effects of vibration from the robot and the environment. The single-link experiment was repeated using this vibration-isolated setup. To reduce other factors, such as unevenly distributed heat input that might mask the effects of the vibration, a heating pad was not used. Laser spot centroid locations extracted from images acquired by the CCD camera were plotted over a period of 100 minutes (6,200 s), as shown in Figures 4.16a and 4.16b.

### 4.6.2 Results and Discussion

Figures 4.16a and 4.16b present results of the experiment performed with the vibration-isolated setup superimposed on results of the experiment performed with the regular setup. As indicated above, locations of the centroid of the laser spot in both  $x$ -axis (longitudinal) and  $y$ -axis (transverse) directions, were plotted.



(a) Centroid location in  $x$ -axis direction.



(b) Centroid location in  $y$ -axis direction.

Figure 4.16: Results of robot idle-induced experiment.

Results of the regular setup experiment are shown on the primary  $y$ -axes on the left hand side of the graphs, while those of the vibration-isolated setup experiment are shown on the secondary  $y$ -axes on the right hand side of the graphs. The pair of primary and the pair of secondary  $y$ -axes are set to each have the same scale, so that the amplitudes of each curve on both figures are proportional.

Figure 4.16a shows that the vibration has only small effects on the measurement in the  $x$ -axis direction. The amplitude of the oscillation of the centroid location declines from approximately  $\pm 0.20 \mu\text{m}$ , with idle-induced vibration, to  $\pm 0.18 \mu\text{m}$  when the vibration is isolated. The standard deviation of the results of the experiment without the vibration is 12% smaller than that of the experiment with the vibration. However, it is not absolutely clear whether this oscillation is caused by the idle vibration exclusively, or in combination with other effects, such as the effects of link alignment.

In the  $y$ -axis direction, as seen in Figure 4.16b, the effects of the vibrations are more obvious. The amplitude of the oscillation of the centroid location declined from approximately  $\pm 1.5 \mu\text{m}$  to  $\pm 0.3 \mu\text{m}$  over the 100-minute period with idle-induced vibration, while the amplitude remained constant at approximately  $\pm 0.25 \mu\text{m}$  when the vibration was isolated. Therefore, at the start, the amplitude of the case with vibration was six times greater than that of the case where the vibration is isolated. These results are summarized in Table 4.3.

Table 4.3: Accuracy improvement due to idle-induced robot vibration.

Measurement direction	Idle-induced vibration	Amplitude of oscillation ( $\mu\text{m}$ )	Average % amplitude reduction
$x$ -axis	✓	$\pm 0.20$	10
	isolated	$\pm 0.18$	
$y$ -axis	✓	decreasing from $\pm 1.5$ to $\pm 0.30$	17 - 83
	isolated	$\pm 0.25$	

Clearly, the idle-induced vibration was a significant source of error in the measurement of the centroid location in the  $y$ -axis direction. When the experiment setup was mounted directly onto the workbench to isolate the effects of vibration, amplitude of the oscillation in the measurement results was greatly reduced, especially at the start. The effects of vibration were much less obvious in the  $x$ -axis direction, which suggests that the vibration may not directly affect the longitudinal deformation. However, the effects of vibration in the  $x$ -axis direction would become significant when combined with other effects such as link misalignment or tilted laser diode.

During the experiment that was conducted to verify the effects of the idle-induced vibration, the vibration was found to occur randomly, and with a variety of durations. Thus, it was not always easy to identify the specific effects of the idle-induced vibration of the robot on experimental results. Hence, idle-induced vibration for the stationary case was eliminated by turning off the robot controller when performing the experiment. For the moving case, when the robot was in motion and not idling, this vibration was not an issue. During the times when the robot paused to allow an image to be captured, it did not idle as it was under motion control commands.

## 4.7 Effects of Accuracy of Laser Centroid Extraction

### Algorithm

In Section 4.6, the idle-induced vibration of the robot was shown to be one of the sources of oscillation appearing in Figure 4.16b. When the setup was isolated from the vibration, the oscillation amplitude was reduced but not completely eliminated. The remaining oscillation demonstrated that there were additional sources for the oscillation that would have to be identified to improve accuracy.

The accuracy of the laser centroid extraction algorithm was found to be a potential

source of error that affected the accuracy of the overall deformation measurement results in [33]. Two proposed improvements were implemented and the single-link experiments were repeated to verify the oscillation was attenuated in the  $y$ -axis direction. The improvements were an adjustment of laser spot size, and a modification of the geometric centroid extraction algorithm.

### 4.7.1 Laser Spot Size Adjustment

Laser spot size was considered in [14] where it was assumed that the extraction algorithm would be most accurate if the laser spot was tuned as finely as possible, *i.e.*, close to being invisible. This was based on the assumption that a smaller area spot would impose less computational error in the extraction algorithm of the geometric centroid of the illuminated area. This assumption was also applied to the single link experiment [10]. However, the requirements of the positioning repeatability experiment [14] were different than those of the single-link experiment, and it was later found, through experimentation, that the assumption of using the near-invisible laser spot was not appropriate for the centroid extraction algorithm of the single-link experiment.

The single-link experiment was repeated using a larger size laser spot to investigate the effects on the accuracy of the laser centroid extraction algorithm. The experimental results, also presented in the following section, indicated that the centroid extraction algorithm would yield improved estimates when a large size laser spot was used, since larger numbers of brightened pixels of the laser spot image were considered.

Figure 4.17a is an image of the original near-invisible laser spot. In an approach to improve the accuracy of the centroid extraction algorithm, the laser spot was tuned and focused so that its shape was an ellipsoid with shape parameters approaching that of a sharp-edged circle (*e.g.*, Figure 4.17b). Most of the bright pixels had the highest possible value of intensity (*i.e.*, white or extremely light gray pixels). Typically, the large sharp-

edge circle laser spot, as shown in Figure 4.17b, was found to be approximately 10 times larger than the near-invisible laser spot.

The use of a large laser spot increased the number of the white pixels. Higher numbers of white pixels reduced the ratio between the number of the gray pixels on the edge of the laser spot and the white pixels in the middle of the laser spot. When the grey pixels, which were the source of error of the centroid extraction algorithm due to the inconsistency of the pixel intensity, became less significant, the accuracy of the centroid extraction algorithm was then improved. Note that with the use of a large laser spot, the use of threshold values to convert the laser spot images into binary images was no longer required. Results (centroid locations) of the verification experiment of the laser spot size adjustment were compared to the results of the single-link experiment, which was previously conducted using a near-invisible laser spot.

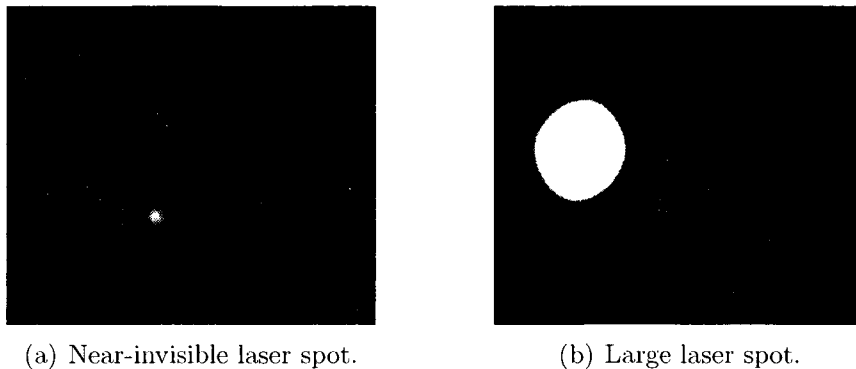


Figure 4.17: Images of laser spot acquired by CCD camera.

### 4.7.2 Modification of the Laser Spot Geometric Centroid Extraction Algorithm

Each grayscale image of the laser spot was evaluated with a geometric centroid extraction algorithm yielding coordinates of the geometric centroid of the laser spot with sub-pixel accuracy. In the original algorithm [29], all pixels were considered. Including pixels of

all shades had an impact on accuracy of the overall deformation results when the laser spot appearing on an image was insufficiently bright and/or sharp. Compared to high quality images, low quality images of dark and/or blurred laser spots contained more gray pixels, generally on the circumference of the spots. The shade of each gray pixel was not always consistent over time, as even a very small fluctuation in input voltage of the laser diode would result in a change in the intensity level of the laser spot detected by the CCD camera. Therefore, distribution of the gray pixels varied throughout the experimental period.

Each pixel in an image of a laser spot contained a 16-bit grayscale colour value corresponding to intensity of the laser at that location. The grayscale colour ranged from black to white, and was evenly divided. Each shade of the grayscale colour was assigned a 16-bit value between zero (black) and 65,535 (white). Each colour-defined value was used as a weighted fraction of the system mass for determining location of the geometric centroid of the laser spot. The method for estimating of the laser spot centroid location was similar to the method for estimating the centre of gravity of an object with a mass moment about the  $x$ - and  $y$ -axes [14].

In the original centroid extraction algorithm, in which all pixels were evaluated as system masses, a problem was detected when the quality of the laser spot images was low. The laser spot of the low quality images appeared as a blurred gray circle instead of a sharp white circle. The intensity of the pixels around the edge of the blurred laser spot was low and not always consistent. Small changes in pixel intensity could affect the overall accuracy of the centroid extraction algorithm because of the moment technique used to estimate centroid sub-pixel accuracy.

To address the inconsistency of the intensity of the laser spot periphery, the centroid extraction algorithm was modified to allow users to set a threshold value of the lowest intensity to be used for each extraction. Any shades of gray that represented a lower

intensity than the threshold would be considered black. It was found that the use of the lowest intensity threshold reduced the uncertainty of the centroid extraction algorithm associated with the inconsistency of laser intensity around the edge of the laser spot. Next, an option for the highest intensity threshold was implemented in the algorithm. All shades of gray with intensity higher than the highest threshold value would be considered as white pixels. The extraction algorithm also provided a distribution of the amount of pixels in each shade of gray, and the maximum value of the intensity of each laser spot image<sup>2</sup>.

To verify the effectiveness of the use of the threshold values, the results of the single-link experiments were re-computed using the modified extraction algorithm. In comparing the results, it was found that the use of the threshold values improved the overall accuracy of the centroid extraction algorithm, especially the extraction of the images with small and/or low intensity laser spots.

### 4.7.3 Results and Discussion

The accuracy of the extracted centroid location was expressed as the standard deviation of experimental results. A lower standard deviation indicated greater accuracy for the sub-pixel coordinate estimation of the laser spot centroid location. Figure 4.18<sup>3</sup> shows the superimposed amplitude plots of centroid locations in the longitudinal direction of the small and large laser spot centroid locations over a period of three hours. The oscillation in the large laser spot results was smaller in amplitude and more compact than that in the small laser spot results, which implied a lower standard deviation of the large laser spot results.

The modified algorithm allowed all quality images to be analyzed more accurately

---

<sup>2</sup>The use of a filter that accepts only a narrow gap of wave length in the range on the laser wave length could be implemented in future work of this type.

<sup>3</sup>Results presented in Figure 4.18 are normalized data of the original experimental results (presented in Section 4.8). All amplitudes were normalized by the magnitude of the mean values. The normalization was done to remove the effects of thermal expansion of the CCD camera stand (see Section 4.8).

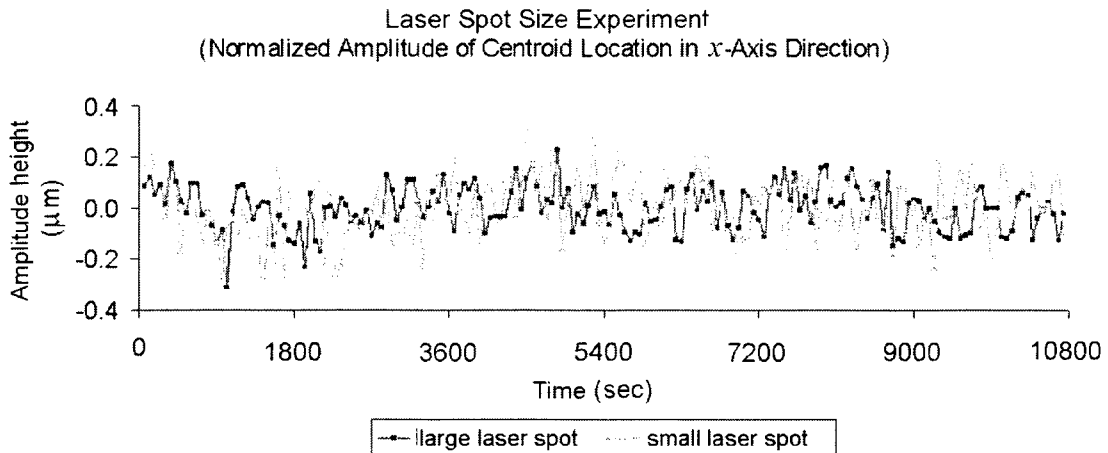


Figure 4.18: Results of laser spot size experiment.

using suitable threshold values of intensity. The values of the laser intensity thresholds were obtained by trial and error in order to obtain the best accuracy of the centroid extraction results. The threshold values varied according to the quality and composition of the extracted images. For the high quality images, *i.e.*, large bright white circle spot with sharp edge on a black background, the use of threshold values did not make significant improvements. The use of threshold values was effective for the extraction of the lower quality images, such as an image of a small oval laser spot with blurred edge, a dark gray laser spot with low distribution in the number of pixels in each colour shade, or an image with a grey background. The modified algorithm also provided the pixel distribution, categorized by intensity levels, and the maximum value of intensity of each image. The pixel distribution (Figure A.2) provided the number of high intensity (*i.e.*, white or light gray) pixels that were considered in the extraction. The maximum intensity confirmed the image quality through the level of brightness of the laser spot on the image. It was found that when the images were extracted using a proper set of threshold values, the accuracy of the extraction algorithm was improved by 5% - 30%, depending on the quality of laser spot images. The results of best improvement using the modified algorithm and the large laser spot are presented in Table 4.4.

Table 4.4: Accuracy improvement due to centroid extraction algorithm.

Modification method	Standard deviation of experimental results ( $\mu\text{m}$ )		% improvement
	before modification	after modification	
Modified algorithm	0.1433	0.1002	30
Large laser spot	0.1221	0.0878	28

## 4.8 Thermal Effects of CCD Camera

In studying the effects of laser spot centroid extraction in Section 4.7, the centroid location of the large laser spot was found to vary over time, as shown in Figure 4.19<sup>4</sup>. The resulting polynomial trend of the large laser spot, seen in Figure 4.19, was unexpected and indicated existence of another source of experimental error.

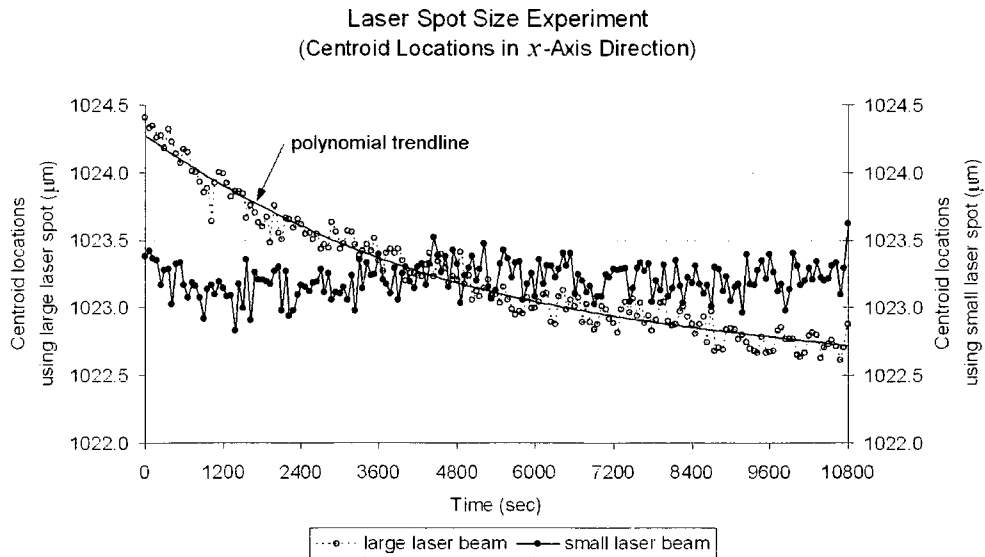


Figure 4.19: Results of the laser spot size experiment before normalizing.

Figure 4.20 illustrates the temperature results obtained at steady state of the experiment conducted to examine the effects of laser spot size. It was observed that the temperature of the CCD camera and the camera stand increased significantly over the

<sup>4</sup>The results from Figure 4.19 were normalized for presentation in Figure 4.18 as previously presented in Section 4.7.

course of the experiment. The temperature of the CCD camera was higher than the temperature of the camera stand because the camera generated heat during the experiment, and some of this heat was transferred to the camera stand. Similar to other components of the single-link experimental model, the increase in temperature of the camera stand resulted in its thermal deformation which, in turn, altered the measurements made with the CCD camera. Hence, reducing the amount of heat transferred from the CCD camera to the camera stand would reduce the deformation of the stand, and ultimately improve the accuracy of the measurement.

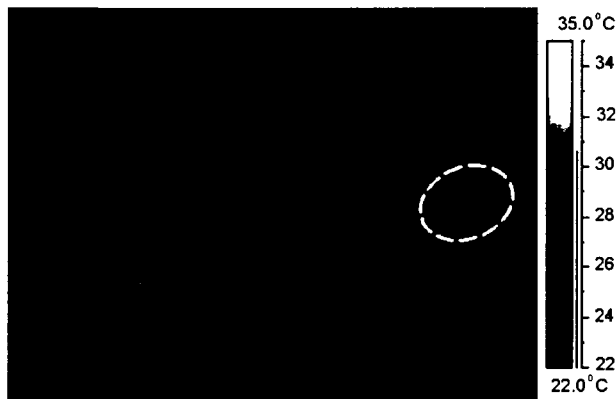


Figure 4.20: Heated CCD camera stand.

### 4.8.1 Experimental Analysis of the Thermal Effects of the CCD Camera

The CCD camera stand consisted of an aluminum mounting plate welded on one end of a short thick pipe and a metal post mounted to a thick acrylic base, as shown in Figure 4.21a. The pipe fitted around the post with a small clearance to allow the mounting plate to slide up and down, as well as spin around the post to permit adjustment of both height and direction of the camera, as shown in Figure 4.21b. The camera was placed facing away from the post, and mounted firmly to the plate with two bolts through the bottom, and

with the back of the camera located at the pipe end of the plate.

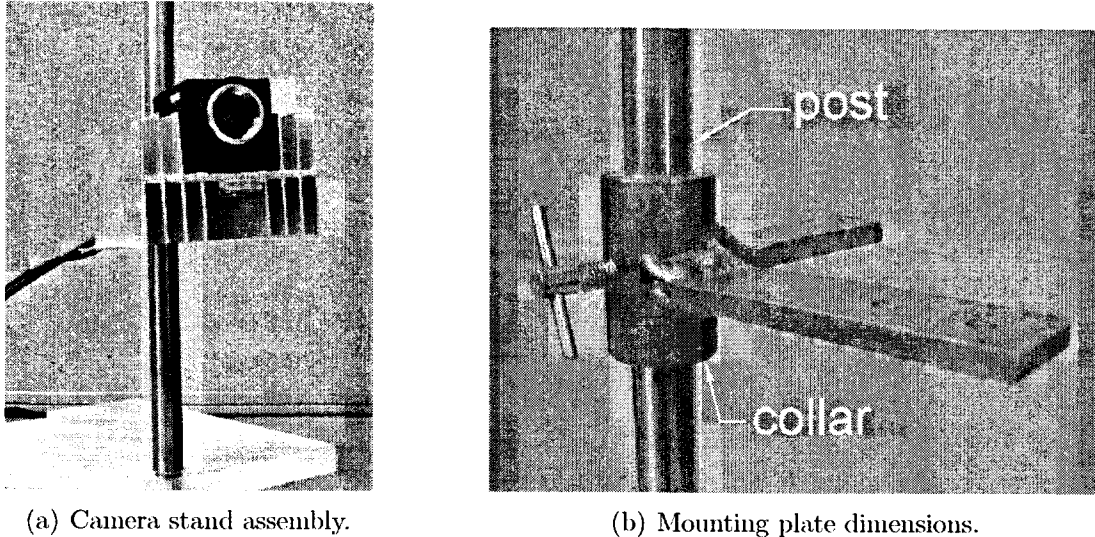


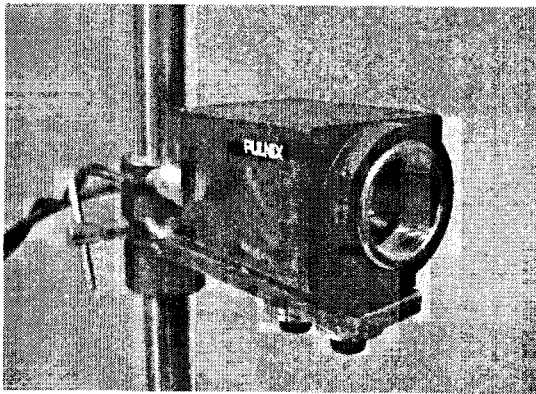
Figure 4.21: CCD Camera stand.

The CCD camera was initially at room temperature of  $22^{\circ}\text{C}$  and reached  $30^{\circ}\text{C}$  within approximately 25 minutes of continuous work (acquiring images every 30 s). Some of the heat generated by the CCD camera was conducted to the aluminum mounting plate, and convected to the environment. The relationship of warming-up in the experimental setup to the thesis work on warm-up in robots was immediately obvious. To verify the assumption that thermal effects of the CCD camera warm-up were the primary causes of the polynomial behaviour of the curve shown in Figure 4.19, a concomitant calculation was performed using the linear coefficient of thermal expansion, *i.e.*,  $\Delta L = \alpha L|T_i - T_o|$ , temperature histories, and deformation results of the camera stand in combination with changes in experimental setup.

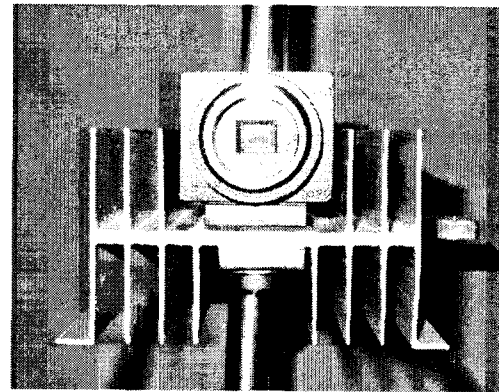
Three modifications were made to the experimental model, and one modification was made to the experimental procedure of the single-link experiment to reduce the thermal effects of the camera. First, a rubber gasket 4 mm thick was inserted between the camera and the stand to decrease conduction to the mounting plate. Second, a piece of mineral wool insulation was placed between the back of the camera and the post to reduce any

effects of convection heating to the post. Third, fins were attached to the bottom of the camera to help release heat to the environment. Finally, a camera warm-up was required as a regular step in the procedure prior to the commencement of each experiment. The change in experimental setup before and after applying the improvements, is illustrated in Figures 4.22a and 4.22b.

The single-link experiment was repeated with and without applied heat input, using the improved setup, and the camera was warmed-up before being used for the measurement. The experimental procedures for both cases were similar to those of the stationary case of the single-link experiment. In the case where heat was applied, the system was initially at room temperature, then the heating pad was turned on.



(a) Original setup.



(b) Improved setup.

Figure 4.22: CCD camera stand assembly before and after the improvement.

### 4.8.2 Results and Discussion

The aluminum mounting plate of the camera stand was assumed to be 6061 Al. As shown in Figure 4.21b, the mounting plate was 101.6 mm long, 25.4 mm wide and 6.2 mm thick. The linear coefficient of thermal expansion of 6061 Al was  $23.6 \times 10^{-6} K^{-1}$ . The initial temperature of the mounting plate was  $22^\circ C$ , and from the temperature results presented in Figure 4.20, the steady state temperature of the mounting plate was  $25.5^\circ C$ .

Using the linear coefficient of thermal expansion, and the temperature results, the change in dimension (expansion) of the mounting plate along the  $x$ -axis was estimated to be  $2.05 \mu\text{m}$ . The change in dimension of the mounting plate extracted from the polynomial trendline of the experimental results presented in Figure 4.19 was  $1.90 \mu\text{m}$ . The 7.9% difference between the estimated and measured values suggested that temperature-induced deformation of the mounting plate was a significant source of measurement error.

Figure 4.23 shows temperature results of the experimental case without the heat input at steady state. The steady state temperatures of the camera and the mounting plate were  $31^\circ\text{C}$  and  $24^\circ\text{C}$  respectively. When using the improved setup of the CCD camera stand assembly, the increase in temperature of the mounting plate was reduced to  $2^\circ\text{C}$ , from that of  $3.5^\circ\text{C}$  when using the original setup. This reduction in temperature increase was almost a 40% improvement. It was also observed that the temperature of air around the camera was greater when using the improved setup ( $26^\circ\text{C}$ , as opposed to  $24.5^\circ\text{C}$  when using the original setup), which indicated that heat was more efficiently released to the environment through the attached fins.

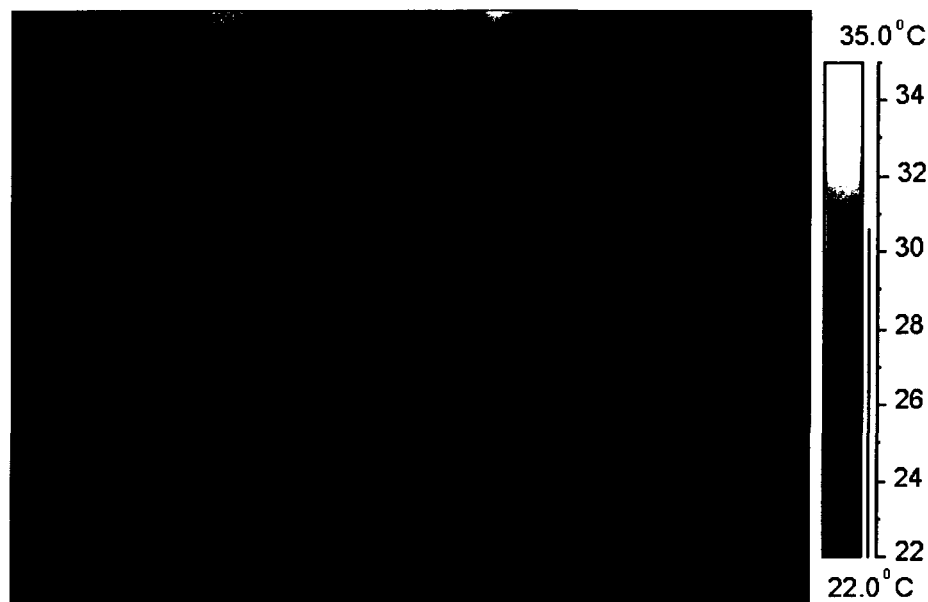
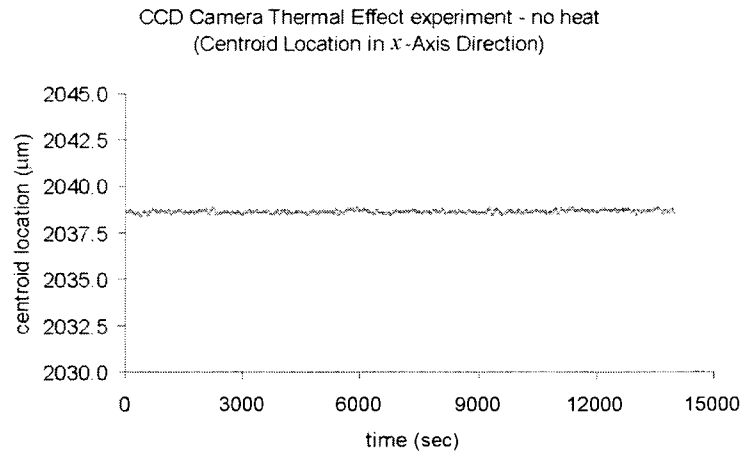


Figure 4.23: Temperature results of thermal-effect experiment with no heat applied.

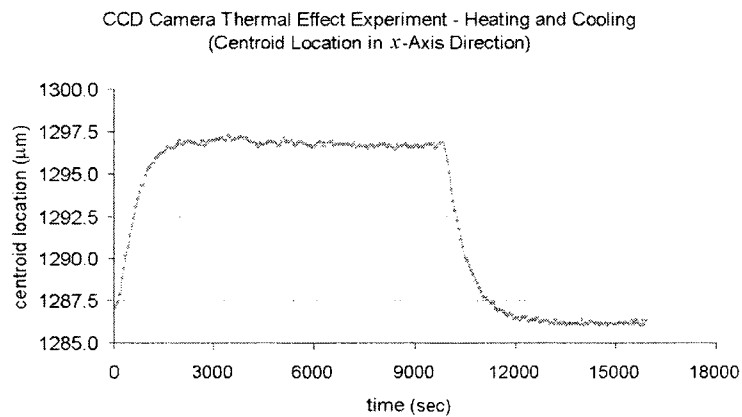
Figure 4.24a presents locations of the laser spot centroid over time in the  $x$ -axis direction of the case without heat input. The range of the resulting data was  $0.29 \mu\text{m}$  and the standard deviation was  $\pm 0.085 \mu\text{m}$ . Figure 4.24b presents the change in location of the laser spot centroid of the case with heat input. As indicated, steady state was reached at about 3,000 s, and the total deformation was approximately  $10 \mu\text{m}$ . The heating pad was turned off after 10,200 s, as observed in Figure 4.24b at the start of the second transient state of the centroid location. As expected, the system required approximately 3,000 s to cool down. Note that the magnitude of the deformation detected during the cooling down period (starting at 10,200 s) was  $0.8 \mu\text{m}$  greater than the magnitude of the deformation due to the heating up period (starting at 0 s). The difference in deformation magnitude was caused by the initial temperature of the experimental model being slightly higher than room temperature, due to the incomplete cool-down of the model from the previous experiment.

With the use of the improved setup of the CCD camera stand assembly and the use of the warmed-up camera, the polynomial behaviour, as seen in Figure 4.19, was eliminated. The standard deviation of laser spot centroid locations at the steady state of both with and without heat input cases was approximately  $\pm 0.1 \mu\text{m}$ , which was several orders of magnitude smaller than the expected value of  $\Delta L_x$  ( $45 \mu\text{m}$ ). The comparison indicated that the improved setup provided an adequate level of accuracy for the deformation measurement. Although the verification experiments were only performed with the stationary case, it was clear that the results also applied to the moving case.

The effective reduction of the thermal effects of the CCD camera was mainly achieved using fins and warming-up the CCD camera. The fins allowed heat, generated by the camera during its working period, to be released to the environment faster, thereby reducing the amount of heat transferred directly to the bottom piece of the stand. The temperature-induced deformation of the camera stand was reduced, as was its effect on



(a) Deformation results of the case without heat input.



(b) Deformation results of the case with heat input.

Figure 4.24: Deformation results of thermal-effect experiment.

the accuracy of the measurement results. Warming-up the CCD camera before acquiring images for each measurement also reduced the errors in the extracted centroid locations. The temperature results suggested that the camera would reach its thermal steady state after 30 minutes of continuous operation.

## 4.9 Heating Pad Flexibility

Irregular and poorly distributed heat input supplied to the shaft was observed during the single-link experiment. This suggested that the heating pad was a possible source of

error in the temperature measurement. Originally, a 25.4 mm  $\times$  300 mm silicone rubber, fibreglass-insulated heating pad was used to supply heat to the shaft. The large width and thickness of the heating pad did not allow it to be snugly wrapped around the exposed surface of the shaft. Instead, the heating pad was rolled into a loose hoop around the shaft, as shown in Figure 4.25. The shaft rotation during the moving case experiment caused changes in the contact points of the heating pad relative to the shaft. An increase in air temperature around the output shaft was found to be approximately 4°C, which was likely caused by convection from the unused portion of the heating pad.

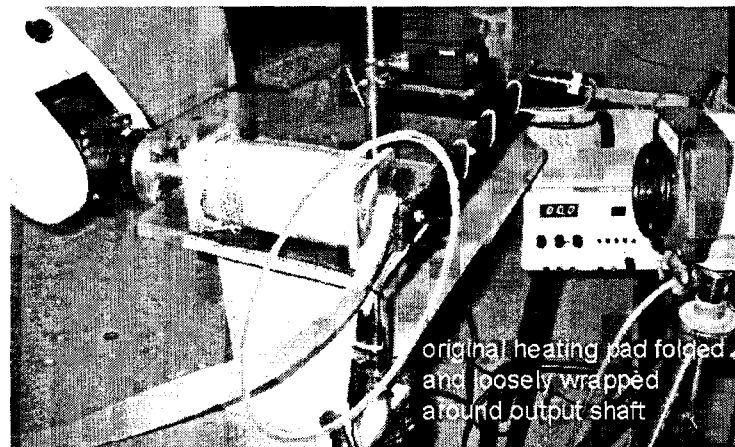


Figure 4.25: Original heating pad assembled on shaft.

#### 4.9.1 Experimental Analysis

The original heating pad was replaced by a Kapton-insulated flexible heating pad. This flexible heating pad was 100 mm long, 25.4 mm wide and 0.25 mm thick. It was tightly wrapped around the length of the shaft with thin twine. With this improved fastening, and the proper size of heating pad, heat was efficiently conducted from the flexible heating pad to the shaft, as proven by the significant reduction of the air temperature around the shaft due to the convected heat losses. Figure 4.26 shows temperature distribution at the steady state of the shaft that was wrapped by the flexible heating pad. The average temperature

in the area around the heating pad at steady state was  $23.5^{\circ}\text{C}$ . As the initial ambient temperature was  $22^{\circ}\text{C}$ , the increase in air temperature around the shaft was  $1.5^{\circ}\text{C}$ . This increase in air temperature was approximately 65% lower than when using the original heating pad.

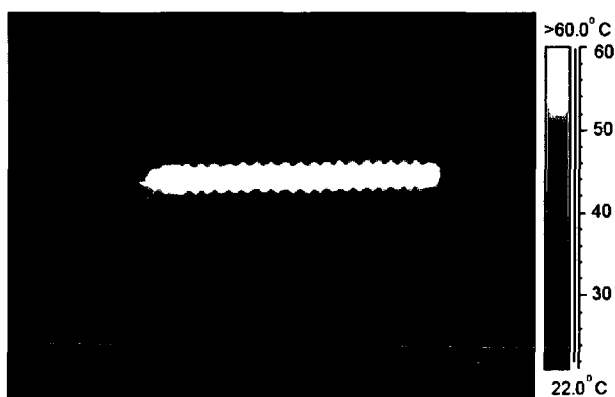


Figure 4.26: IR image of flexible heating pad when supplying heat to the single-link experimental model.

## 4.9.2 Results and Discussion

With the improved arrangement of the flexible heating pad, particularly the elimination of the heating pad motion, consistent heating was provided for the single-link experiment in both stationary and moving cases. No further study was made on the effects of the incomplete wrapping of the flexible heating pad, since an adequate level of accuracy in the measurement was obtained with the modified experiment setup and measurement system, which used the flexible heating pad.

## 4.10 The Improved Deformation Measurement System

As has been discussed, a number of studies were undertaken to investigate the possible sources of error and their effects on the deformation measurement system. A number of possible improvements to eliminate the errors were tested and all results have been presented. The results show that some possible sources of error produced insignificant effects on the output of the deformation measurement system, while others had more significant impact. All sources of error listed in Table 4.1 are listed again in Table 4.5 with their qualitative effects on the measurement system.

## 4.11 Validation Experiment of the Improved Deformation Measurement System

The goal of the work presented in this Chapter was to identify and attenuate experimental sources of error that have caused discrepancies between observed experimental results and FEA predictions of longitudinal deformation in the simplified robot mechanical system. Of particular concern was that the FEA results reached steady state faster than the experimental results and had a higher steady state deformation when compared to the experiment. All improvements to the deformation measurement system presented in Section 4.5 - Section 4.9 were implemented, and the moving link experiment was re-performed using the improved deformation measurement system shown in Figure 4.27.

Figure 4.28 shows that the longitudinal deformation from the experiment and the FEA model now have good agreement in both the rise time response and the value of deformation at steady state when compared to Figure 3.12. Having addressed the potential sources of errors, and implemented corresponding improvements to the measurement sys-

Table 4.5: Possible sources of error ranked by significance of effects on the deformation measurement system.

Possible sources of error	Effects	Resulting change in apparatus
Thermal effects of CCD camera	Temperature-induced deformation of camera mounting plate.	Warm-up camera, and use fins, rubber gasket and insulation.
Effects of accuracy of laser centroid extraction	Decrease in overall accuracy of centroid location extraction.	Use large laser spot and use modified algorithm with suitable intensity threshold values.
Idle-induced robot vibration	Vibration of link and laser diode mounted on robot wrist.	Turn robot off during stationary case.
Expansion of diode hole	Laser diode tipping due to physical disturbances.	Isolate link assembly from disturbances.
Heating Pad Flexibility	Inaccurate temperature results obtained due to non-uniform and inconsistent heat input from the original heating pad.	Replace the original pad with flexible heating pad.
Effects of cantilever bending	Insignificant effects.	none.
Effects of link alignment		

tem, there was sufficient assurance in the experimental setup to be certain of deformation measurements on the order of  $\pm 5 \mu\text{m}$ . The good agreement between the results of the experimental and FEA models of the single-link experiment gave the confidence to proceed to a study of a multi-link system, including experimental, FEA and finite difference, based on analytical solution, models. Provided the results proved acceptable, a motion control algorithm based on the finite difference model could be developed using material properties and boundary conditions established in new multi-link FEA models developed in support of continued experimental measurements.

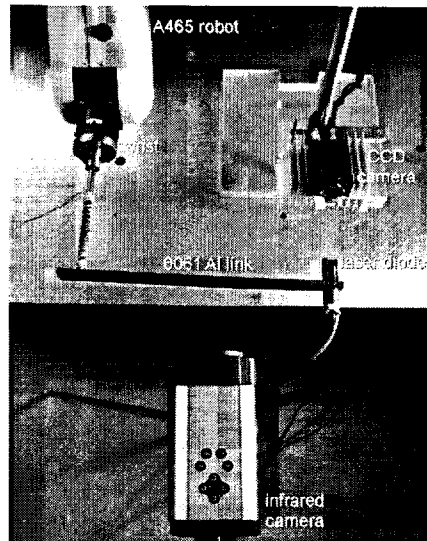


Figure 4.27: Improved deformation measurement system.

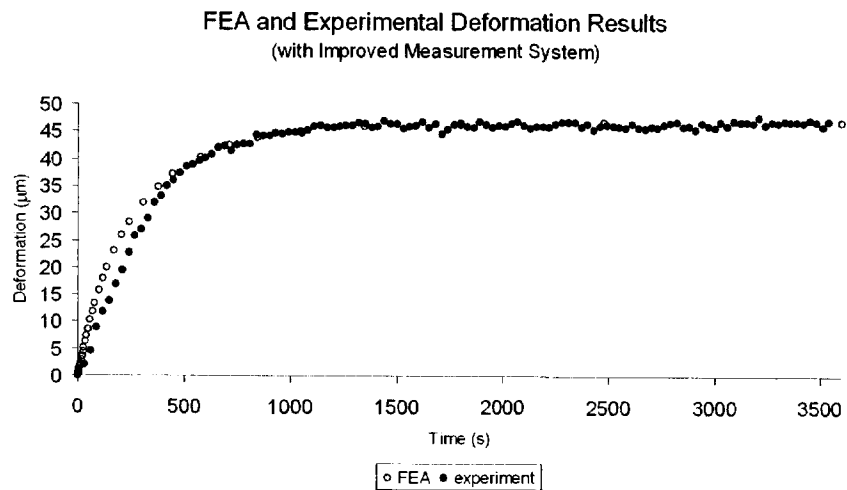


Figure 4.28: FEA and experimental deformation results of the moving case experiment using improved deformation measurement system.

# Chapter 5

## Two-Link Experiment

### 5.1 Introduction

In this chapter, a two-link experimental model is presented. A two-link model is more representative of the multiple-link mechanical systems seen in industrial robots. The model was developed based on the single-link model presented in Chapter 3. An additional link, shaft and heating pad were added to the single-link assembly. Improvements suggested in Chapter 4 were implemented in the experimental model and the deformation measurement system. Similar procedures to those of the single-link experiment were used. An FEA model of the two-link system was also developed based on the existing single-link FEA model. The analytical model (Equation (3.7)) was extended for the two-link system using the finite difference technique and the concepts of thermal resistance and capacitance [40]. Similar to the single-link experiment, results obtained from the experimental, FEA and finite difference models were used for multiple cross-checking of results, with no intention to implement the FEA model in the robot controller for deformation compensation. The finite difference model is the first step towards developing an algorithm to compensate for temperature-induced deformation of the simplified robot mechanical system.

## 5.2 Experimental Model

The two-link system consisted of two slender links, shafts, and heating pads, as shown in Figure 5.1. The second link was attached to the left hand side of the original single-link experimental setup. The shaft of the original model became the middle shaft of the two-link model. The laser diode remained at the distal end.

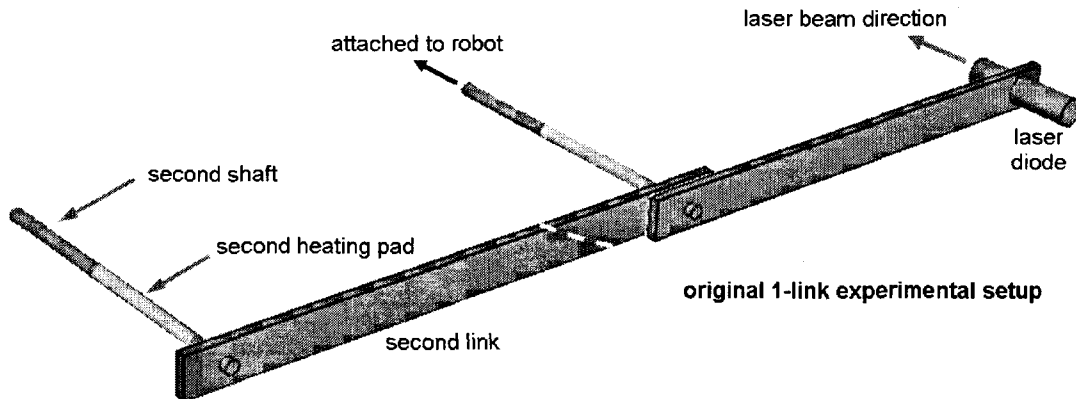


Figure 5.1: Assembly of two-link system.

The gap between the second link and the original link in the direction of the length of the shaft ( $z$ -axis direction) was 8 mm. Similarly, the gap between the original link and the heating pad of the single-link model was also 8 mm.

The second link, as shown in Figure 5.2a, was designed to have an effective link length, or a distance between the centres of the two shaft holes, of 304.8 mm (1 ft). The same temperature and deformation measurement systems used in the single-link system were also used in this experiment.

### 5.2.1 Experimental Apparatus

The width and thickness of the second link were the same as those of the original link from the single-link experimental model. The shaft hole centres were located 25.4 mm

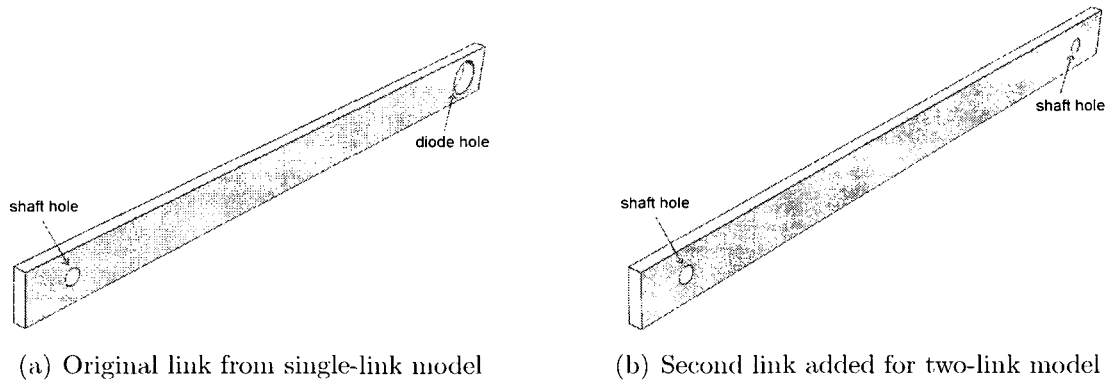


Figure 5.2: Slender links.

from each end of the shaft, and each hole diameter was 8.0 mm. The second link was made of the same material as that of the original link, and was painted in the same flat black colour. The second set of shaft and heating pad was identical to that used in the single-link experiment, and mounted in the same manner. Both heating pads were wired together in parallel, to ensure that the same amount of current was used to generate the same amount of heat to be applied by each pad.

For clarification of part assembly, the links and shafts were labelled with new names: left link, right link, left shaft and middle shaft, as shown in Figure 5.3.

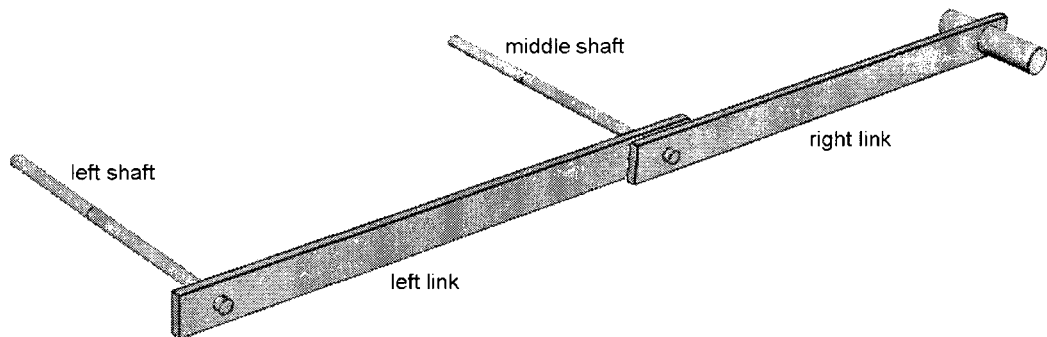


Figure 5.3: New names assigned for shafts and links.

The left shaft was fixed to the workbench. The middle shaft was fastened to the wrist of the A465 robot, which delivered motion control for the moving case experiment, described in Section 3.2.4. In the moving case, the right link was assigned to move, while the left

link remained stationary. To allow the left link to remain stationary while the right link moved, a clearance fit was used on the left link and the middle shaft, and the setscrews that attached the left link to the middle shaft were loosened. The middle shaft could then rotate freely through the shaft hole of the left link. An interference fit was used on the right link and the middle shaft, and the setscrew that fastened the right link to the middle shaft remained tight.

### 5.2.2 Experimental Procedure

Similar to the single-link experiment, the two-link experiment considered two cases: stationary and moving. In the stationary case, both links were adjusted so that their lengths were parallel to the  $x$ -axis and tightly fastened to the shafts. The pose of the links set for the stationary case was also the home position of the moving case. The moving case was performed to examine the effects of the difference in motion between the two links. While the left link remained stationary, the right link was assigned a motion of a reciprocating  $30^\circ$  arc about the middle shaft. The rest of the measurement procedure of the two-link experiment was identical to that of the single-link experiment described in Section 3.2.4.

## 5.3 Finite Element Model

ABAQUS [49] was used to perform a coupled thermal-mechanical FEA. An FEA model of the two-link system was created based on the FEA model of the single-link model presented in Section 3.4 with a few modifications corresponding to an additional link, shaft and heating pad.

### 5.3.1 Model Assembly

Similar to the modification of the experimental setup presented in Section 5.2 above, the FEA model of the two-link system was the single-link model with the additional link, shaft, and heating pad attached to its left hand side. The additional link and shaft had the same mechanical boundary conditions, element configurations (eight-node trilinear hexahedral elements), and thermal convergence criteria, as the original pair of link and shaft from the single-link model. The only two changes made were to increase the number of elements of the additional link along its length from 23 to 32 elements, and to change the boundary conditions regarding heating pads. The development of the heating pad model, and an improvement of the boundary conditions regarding the heating pads, are described in Section 5.3.2.

### 5.3.2 Heating Pads

In the single-link FEA model, using the original stiff heating pad, the heating pad was not used as a part in the model assembly. Instead, heat input at shaft surface, generated by the heating pad, was assigned as a boundary condition of a surface temperature. This was found to provide good results. In the two-link study, a slightly different approach was taken built on the combined experience with the first FEA model and the understanding of the new heating pads. Each shaft was re-modelled as a small stub (see Figure 5.4) and the heat of heat pad was applied as a surface heat flux, to the cross-section of each shaft.

### 5.3.3 Material Properties and Boundary Conditions

Materials in the FEA model of the additional link and shaft were 6061 Al and 430 SS respectively, as assumed in the single-link model. No change was made in the laser diode.

The initial temperature ( $t = 0s$ ) of the model was set to the ambient temperature of

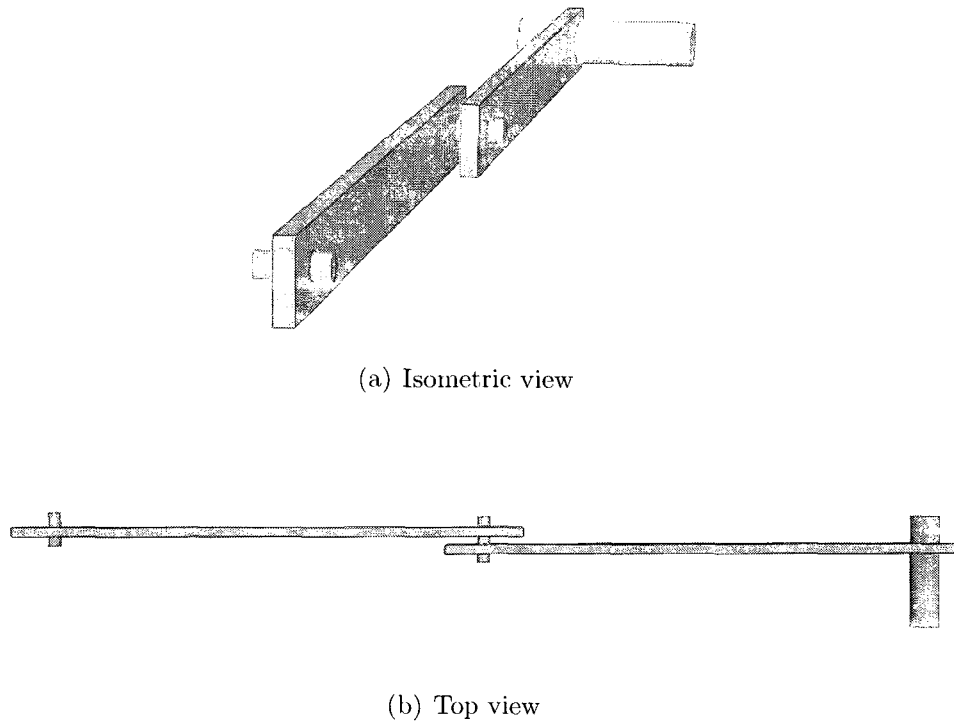


Figure 5.4: Two-link FEA model with short shafts.

22°C. The convection heat transfer coefficient for the stationary case was  $2 \frac{W}{m^2 K}$ . For the moving case, the convection heat transfer coefficient for the moving link and the stationary link were  $7.75 \frac{W}{m^2 K}$  and  $2.5 \frac{W}{m^2 K}$  respectively [40]. Convection was permitted for all free surfaces of the link.

The boundary conditions of temperature and heat transfer coefficients were similar to those assigned in the single-link FEA model. The only two exceptions were boundary conditions related to heat input due to the addition of the heating pads, and mechanical boundary conditions appropriate to the two-link system.

The heat input was computed from the output voltage produced by heating pads. Temperature results of the shaft, over time, obtained from the FEA model, were compared to those recorded by the IR camera from the experimental model in order to verify the accuracy of the computed heat input. Only a small difference between the results of the two

models was found, hence it can be concluded that the heat input was computed accurately from the voltage history. It was also found that a laser diode produced a small amount of heat. This heat input was then assigned as a new boundary condition in the two-link FEA model. To prevent rigid body motion, the centre of the left shaft cross-section at the far end was fixed in all directions, and the third point at the centre of the shaft cross-section at the end near the link was constrained to horizontal motion.

## 5.4 Finite Difference Model

The two-link system was treated as a one-dimensional finite difference model simplified to a single link with length equal to the total length of the two-link model. The shaft and diode holes on the links were omitted in the model, however, the finite difference nodes were specifically placed according to the locations of hole centres. Smaller finite difference elements were assigned near the centre of each hole. The node arrangement is shown in Figure 5.5.

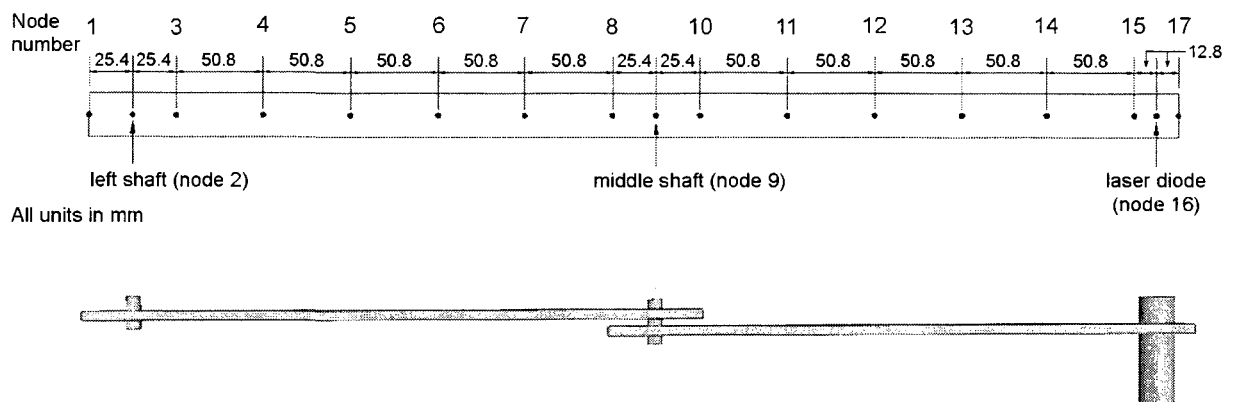


Figure 5.5: Nodal boundaries of two-link analytical model.

The width of the links was considered small compare to the length of the links, thus temperature was assumed to be constant across the cross-section of the links. Nodes were

assigned at the mid width along the length of the links. Denser positioning of the nodes was assigned near hole locations. A finite difference model was constructed using a forward-difference equation (Equations (5.1)) including thermal resistance and capacitance [40] for all nodes and boundary conditions.

$$T_i^{p+1} = \frac{\Delta\tau}{C_i} \left[ q_i + \sum_j \frac{T_j^p - T_i^p}{R_{ij}} \right] + T_i^p. \quad (5.1)$$

where:

$T_i^{p+1}$  is the temperature at each node simultaneously solved for each next time step,

$C_i$  is thermal capacity, defined as  $C_i = \rho_i c_i \Delta V_i$ ,

where  $\Delta V$  is the volume element,

$q_i$ , is the heat delivered to node  $i$ ,

$R_{ij}$  is the thermal resistance between nodes  $i$  and  $j$ ,

superscript  $p + 1$  indicates time after time increment,  $\Delta\tau$ ,

subscript  $i$  indicates node of interest,

subscript  $j$  indicates adjoining nodes.

All parameters used in Equation (5.1) are summarized in Table 5.1.

Heat input was assigned at nodes 2 and 5, representing the centres of the left and middle shafts respectively. For consistency, the magnitude of the heat input was equivalent to the magnitude of the surface heat flux assigned to the shafts in the FEA model. The value of heat convection coefficient was also the same as that assigned in the FEA model of the stationary case of the two-link model (*i.e.*,  $h = 2.5 \frac{W}{m^2 K}$ ).

To ensure stability of Equation (5.1), the time increment,  $\Delta\tau$ , must be less than or equal to the term  $\frac{C_i}{\sum_j (1/R_{ij})}$  of the most restrictive node [40]. Therefore, the time increment chosen must satisfy a condition:

$$\Delta\tau \leq \left[ \frac{C_i}{\sum_j (1/R_{ij})} \right]_{min}.$$

Table 5.1: Parameters for finite difference model.

Node Number	$R^- \left(\frac{^\circ C}{W}\right)$	$R^+ \left(\frac{^\circ C}{W}\right)$	$R_\infty \left(\frac{^\circ C}{W}\right)$	$C_i \left(\frac{J}{^\circ C}\right)$
1	2480.00496	0.984325793	496.000992	4.320792861
2	0.984325793	0.984325793	248.000496	8.641585722
3	0.984325793	1.968651586	186.000372	12.96237858
4 - 7	1.968651586	1.968651586	124.000248	17.28317144
8	1.968651586	0.984325793	186.000372	12.96237858
9	0.984325793	0.984325793	248.000496	8.641585722
10	0.984325793	1.968651586	186.000372	12.96237858
11 - 14	1.968651586	1.968651586	124.000248	17.28317144
15	1.968651586	0.492162896	403.000806	6.481189291
16	0.492162896	0.492162896	496.000992	4.320792861
17	0.492162896	2480.00496	992.001984	2.16039643

$R^-$  = resistance on the negative  $x$  side of node  $i$

$R^+$  = resistance on the positive  $x$  side of node  $i$

$R_\infty$  = resistance due to convection of node  $i$

The solution of the set of equations, Equation (5.1) of each node, was accomplished by a built-in iterative-solution feature of Microsoft Excel, which is similar to the templates shown in Appendix D of [40]. Using this temperature solution, together with Equations (3.7), the longitudinal deformation of each node was calculated at each time step. The total deformation of the two-link model was then obtained by integrating the deformation of all nodes located between the centre of the left shaft and the centre of the laser diode.

Originally, the material properties of 6061 Al were assigned to all nodes of the finite difference model. The deformation results differed slightly from those obtained from the experimental and FEA models. With further analysis of the results and material properties, it was found that the material properties used in the finite difference model must take into account the influence of the properties of the shafts (430 SS). The influence of

the 430 SS on the finite difference model corresponded to the nature of the experimental model where the links were fastened tightly to both shafts in the stationary case, and deformed as a rigid body. Therefore, a new set of material properties, which represented influences of both materials proportionally (*e.g.*, density of composite,  $\rho_c = \rho_1 V_1 + \rho_2 V_2$ ), was obtained by using the *rule of mixtures* as described in the following section.

### 5.4.1 Rule of Mixtures

To apply the rule of mixtures (ROM), the system of 6061 Al links and 430 SS shafts was considered as a composite material. A volumetric ratio of this composite material was defined with an equivalent volumetric ratio of the materials comprising the experimental model: 98% aluminum - 2% stainless steel. The volume of the stainless steel shafts was computed using the length of the shafts equal to the thickness of the link, and not the full length of the shaft due to the difference in thermal behaviour of the different portions of the shaft. To estimate changes in temperature at other portions of the shaft, such as the middle portion of the shaft whose surface contacted the heating pads, or the far end of the shaft that was exposed to ambient temperature, different mathematical models are required.

Using the ROM [52, 53], the material properties of a fibre-reinforce composite can be defined as follows. Using the volume fraction,  $V$ , fibre,  $f$  and matrix,  $m$ :

Density,  $\rho_c$ :

$$\rho_c = \rho_f V_f + \rho_m V_m. \quad (5.2)$$

Heat capacity,  $C$ :

$$C = \frac{1}{\rho_c} (V_f \rho_f C_f + V_m \rho_m C_m). \quad (5.3)$$

Longitudinal conductivity,  $k_{11}$ :

$$k_{11} = V_f k_{f1} + V_m k_m. \quad (5.4)$$

Longitudinal thermal expansion coefficient,  $\alpha_{11}$ :

$$\alpha_{11} = \frac{V_f E_{f1} \alpha_{f1} + V_m E_m \alpha_m}{E_{f1} V_f + E_m V_m}. \quad (5.5)$$

Subscript  $f$  indicates the properties of fiber, and subscript  $f1$  indicates the properties of fiber in the longitudinal direction.

Assuming Equation (5.2) - Equation (5.5) apply to the 98 *v/o* - 2 *v/o* aluminum to stainless steel assembly, properties can be estimated as listed in Table 5.2, if steel is considered the fibre portion.

Table 5.2: Material properties calculated using ROM.

Material Property	6061 Al [45]	430 SS [45]	ROM
Thermal conductivity $\left(\frac{W}{m \cdot K}\right)$	167	26.1	159.99
Density $\left(\frac{kg}{m^3}\right)$	2713	7800	2966.15
Linear coefficient of thermal expansion ( $K^{-1}$ )	$23.6 \times 10^{-6}$	$10.25 \times 10^{-6}$	$23.26 \times 10^{-6}$
Specific heat $\left(\frac{J}{kg \cdot K}\right)$	892	460	836.64

## 5.5 Results and Discussion

The surface heat flux representing heat input of the two-link system was computed, using output power of the heating pad as stated in specification sheet [54], to be  $0.016 \frac{W}{mm^2}$  ( $10 \frac{W}{in^2}$ ) at 110 V. The effective surface area of each heating pad was  $1936 \text{ mm}^2$  ( $3 \text{ in}^2$ ), and the input voltage was constant at 70 V. Therefore, the heat flux provided by each

heating pad to the shaft surface was 21 W. In the FEA model, this heat flux value was assigned as a boundary condition of heat flux per unit area  $\left(\frac{J}{s \cdot m^2}\right)$ . The heat flux was applied at the far end of the shafts. The cross-section area of both shafts was 0.50 mm<sup>2</sup>, and the flux direction was into the shafts.

An interesting thermal behaviour due to heat conduction was discovered in the overlapped area of the two links (at the middle shaft) for both moving and stationary cases. A series of temperature contour images of the overlapped area is shown in Figure 5.6. The first and last images are the results at 105 s and 143 s respectively from the start. Note that the area shown in black was the area that remained at the initial temperature (22°C) throughout the period of interest. At the left link, the temperature increased smoothly due to heat conduction from the left side of the link near the left shaft, to which heat was applied, toward the right hand side of the link. With a constant amount of heat input, the temperature of the left side of the link was constantly higher than the right side of the link. When heat reached the area around the middle shaft, a large portion of the heat flowed primarily to the tail of the left link. Once the tail was heated, the heat flow went along the shaft toward the other end (into the paper direction), to which the right link was attached. Then, the heat flowed to the left tail of the right link, which caused a deformation in a negative direction (toward the left hand side of the system). In short, the right end of the left link was expanding to the right hand side at the same time as the left end of the right link was expanding to the left hand side. The result was a small decrease in the total (positive) deformation during the transient state.

Deformation results of the stationary case are presented in Section 5.5.1. The results from the experimental, FEA and finite difference models are presented together and show their exceptionally good agreement. Temperature and deformation results of the moving case is presented in Section 5.5.2. The temperature distribution of the two-link system was obtained from the FEA model, and the deformation results were obtained from both

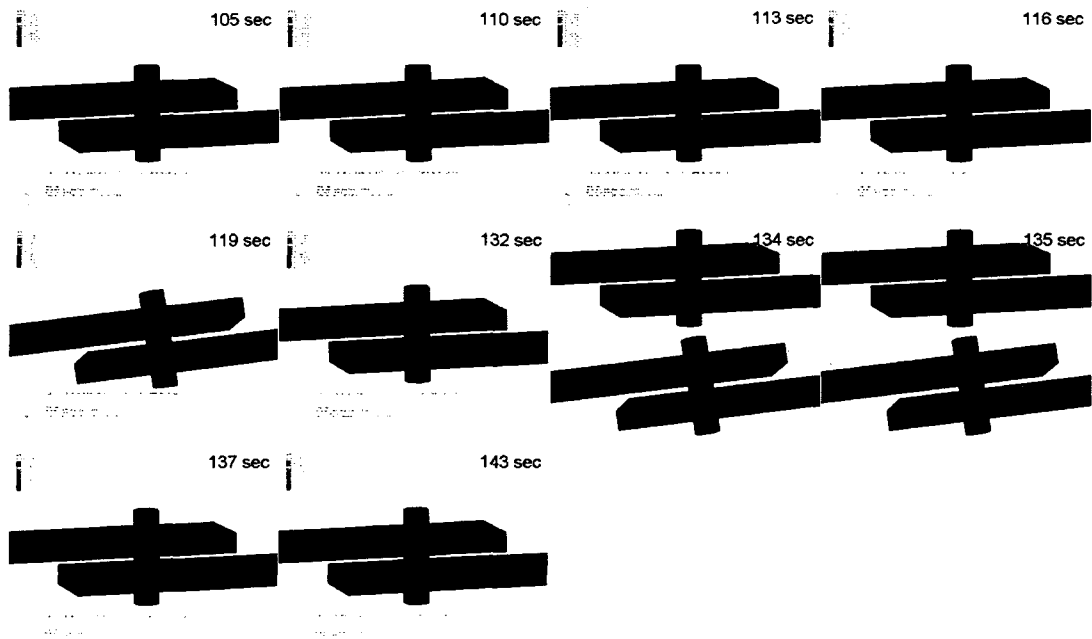


Figure 5.6: Temperature contour of the link overlapped area.

the experimental and FEA models. Similar to the results of the single-link experiment, there was good agreement between the deformation results from both models. Note that only the temperature results of the moving case are presented, as the temperature results of both the stationary and moving cases were very similar.

### 5.5.1 Stationary Case

The results from the experimental, finite difference and FEA models of the stationary case are plotted together in Figure 5.7<sup>1</sup>. The total deformation of the results from all three models was approximately  $150 \mu\text{m}$  and steady state occurred at approximately 520 s.

Excellent agreement was observed between the deformation results of the three models. The agreement confirmed that the deformation of the two-link system from the experimental model can be accurately predicted through both the FEA and finite difference models.

<sup>1</sup>The experimental results are shown as a line since images were captured on a regular basis (30s) and are best showed as a line.

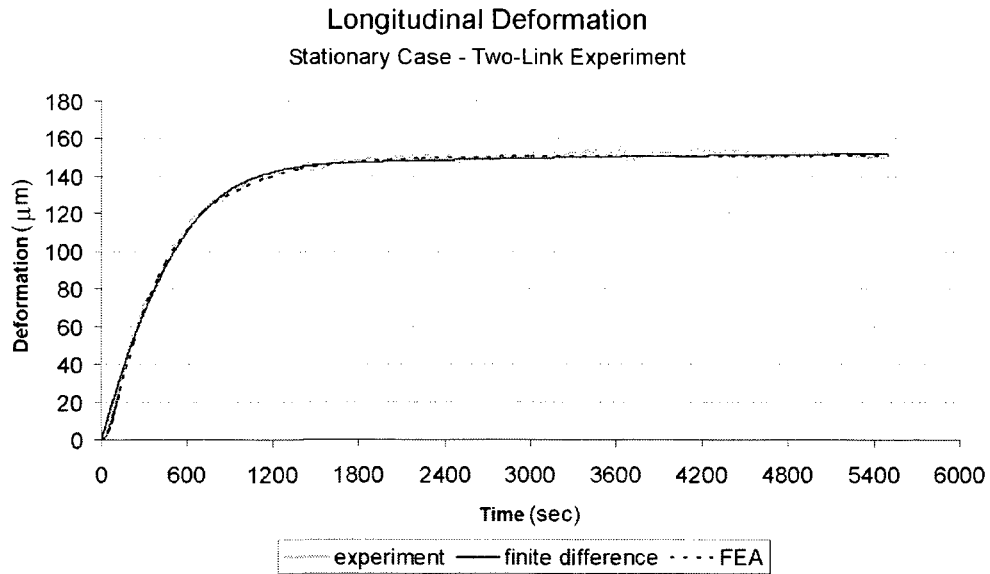


Figure 5.7: Longitudinal deformation from experimental, finite difference and FEA models.

Hence, these predicted results from the FEA and finite difference models can be further used as an input in an algorithm to compensate for the deformation of the two-link system. A compensation concept, validation experiment, and results of the validation experiment are presented next in Chapter 6.

### 5.5.2 Moving Case

The temperature distribution of the moving case obtained from the FEA two-link model is presented in Figure 5.8. The temperature distribution of the right link is similar to that of the link presented in the moving case of the single-link experiment. The right link has higher temperature at the proximal end, where the heat source is attached, and the temperature decreases toward the distal end, where the laser diode is attached. For the left link, with two heat sources attached to each end of the link, the temperature distribution is different from that of the right link. The maximum temperature ( $44.0^{\circ}\text{C}$ ) was found directly above the left shaft of the left link. Although the shafts are symmetrically-located on each end of the left link, the minimum temperature ( $32.5^{\circ}\text{C}$ ) was not located exactly at

the mid point of the link, but rather slightly closer to the middle shaft. This temperature asymmetric pattern was caused by the right link which had only one heat source attached to it, and was in motion during the moving case experiment. Therefore, more heat from the right end of the left link was conducted to the right link and convected toward that direction. A similar temperature distribution was also found in the stationary case experiment. The right link of the stationary case had a higher overall temperature than that of the moving case, due to the lower heat convection coefficient of a still link.

Figure 5.9 presents the deformation results of the experimental and FEA models of the moving case. Reasonable agreement was found in the moving case between the FEA and experimental results with less than 2% difference in deformation. The total deformation was  $120\ \mu\text{m}$  and the system reached steady state at approximately 200 s.

As mentioned in Section 5.2.1, in the moving case experiment the setscrews that fastened the left link to the middle shaft were loosened to allow the left link to remain stationary while allowing the right link to have a wiping motion. Loosening the screws caused a difference in quality of heat conduction between the contacting surfaces. However, the experimental results revealed that the difference in surface quality did not change

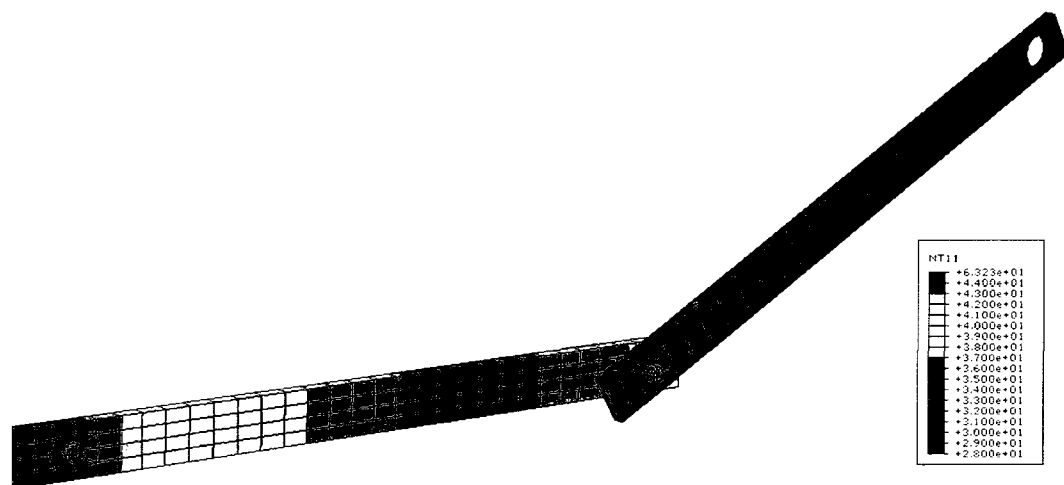


Figure 5.8: Temperature results ( $^{\circ}\text{C}$ ) of moving case.

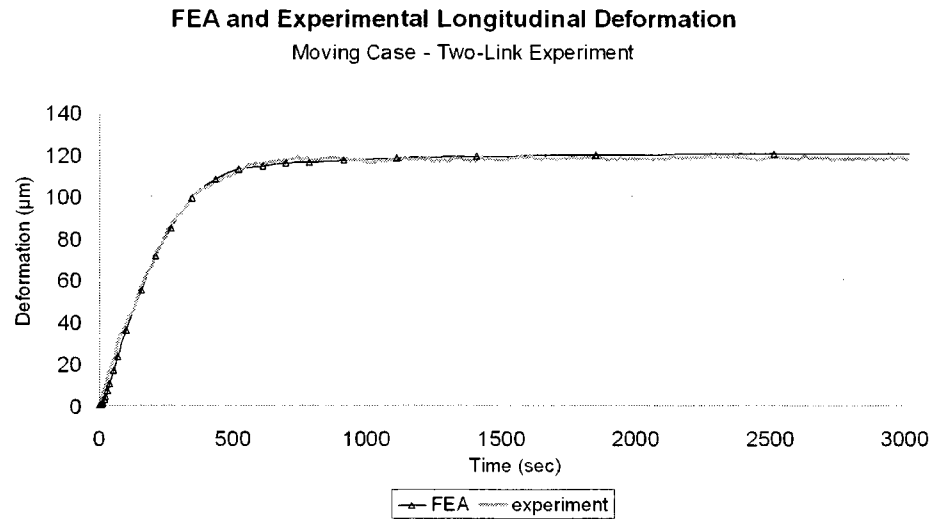


Figure 5.9: Longitudinal deformation of moving case.

the resulting deformation in an observable way, and therefore had a very small impact on the overall conduction. The impact was very small because the dimension of the shaft holes on the links was specified for a clearance fit with a very small clearance. Therefore, the heat loss due to the loose contact surface was significantly less than the total amount of heat input, which was extremely high relative to the diameter of the shaft. Hence, this small amount of heat loss could be neglected.

# Chapter 6

## Compensation Algorithm Concept

### Validation

#### 6.1 Introduction

A major concern in static positioning of robot manipulators is the response of the system to gravity. Fortunately, this has been modelled and compensated for by several robot manufacturers [2]. Typically, this compensation can be done by including a gravity term in the control law for each joint. Similarly, the compensation for the temperature-induced deformation is performed in this research. In the case of temperature-induced deformation, a set of coefficients consisting of ratios between required torque rates of each motor for the compensated and uncompensated systems are required. For each task assigned to a robot, the coefficients are extracted from predicted deformation results and described as a function of time. The coefficients computed from the joint angles required to achieve specifies for motions of the task are assigned to the corresponding motors. The joint angles are then automatically adjusted to compensate for the expected deformation. At the end of the transient state, when the robot becomes thermally and mechanically (*i.e.*,

dimensionally) stable, the compensation is no longer required.

As in the case of gravity compensation, an implementation of a control law for the compensation (*i.e.*, assigning the set of coefficients) requires access to joint controllers, which can only be achieved when an open-architecture robot controller is used. Torque commands are edited using the coefficients and sent directly to the robot motors through the open-architecture controller. However, for a closed-architecture controller, such as the C500C used by the A465 robot in this thesis, the joint controllers are inaccessible. As a result, instead of computing the coefficients, inverse kinematic solution(s) must be computed for the extra motion resulting from the temperature-induced deformation. The kinematic solutions can then be used to compute any displacement required to compensate for the deformation. The corresponding commands are sent to the C500C controller through serial communication. Validation experiments for the compensation algorithm concept were conducted and experimental results, presented here, are used to verify the accuracy of the compensation algorithm. The possibility of implementing the compensation algorithm on full scale systems (*i.e.*, industrial robots) is also implicitly validated.

It is necessary to understand that although the subject of interest of this compensation is industrial robots, in this research the robots are represented by simplified robot mechanical systems specifically the single-link and two-link systems as presented in Chapters 3 and 5. Hence, the total deformation to be compensated is the total deformation of the simplified systems. The A465 robot used in this validation experiment is used as a tool to provide compensation motion, and is not considered the subject-of-interest robot.

## 6.2 Experimental Concepts for Algorithm Validation

For a comparison of deformation results between compensated and uncompensated systems, the validation experiment was performed on one of the cases previously studied.

The stationary case of the two-link experiment was selected for compensation in this validation experiment. Deformation results obtained from the predicted model of the selected case (see Chapter 5) were used as input data. Note that the two-link experiment was not repeated.

In the stationary case of the two-link experiment, no rotary motion was assigned to the links of the system. Therefore, the two-link system could be considered to be a rigid body with one end attached to the tool flange of the A465 robot. The system remained in a desired pose with the tool frame located at the operational goal point throughout the experiment. The tool frame of the two-link system was assigned at the tip of the laser diode that was attached at the free end of the system. If no temperature-induced deformation occurred, the tool frame would remain at the operational goal. If temperature-induced deformation occurred, compensation would be required.

The two-link experiment indicated that the laser diode physically translated along the longitudinal axis of the links due to the temperature-induced deformation of the links and shafts. To compensate for the deformation, the rigid body of the two-link system must be appropriately translated in the opposite direction to that of the deformation. The compensation displacement is provided such that the diode remains at the operational goal at all times, as though the deformation does not occur. This compensation concept is illustrated in Figure 6.1. With this longitudinally dominated deformation, the compensation displacement required is simply a pure translation in the  $x$ -axis direction. The rigid body, which is attached to the tool flange of the A465 robot, is assigned to translate at the same rate, but in the opposite direction of the deformation over the period of the transient state. To allow for a smooth and accurate compensation, commands for compensating displacements must be sent to the robot controller quickly at as high a rate as possible in order to keep up with the transient deformation. After the centroid location of the laser spot was set at the start at the operational goal, an estimate of the error of the compensation can

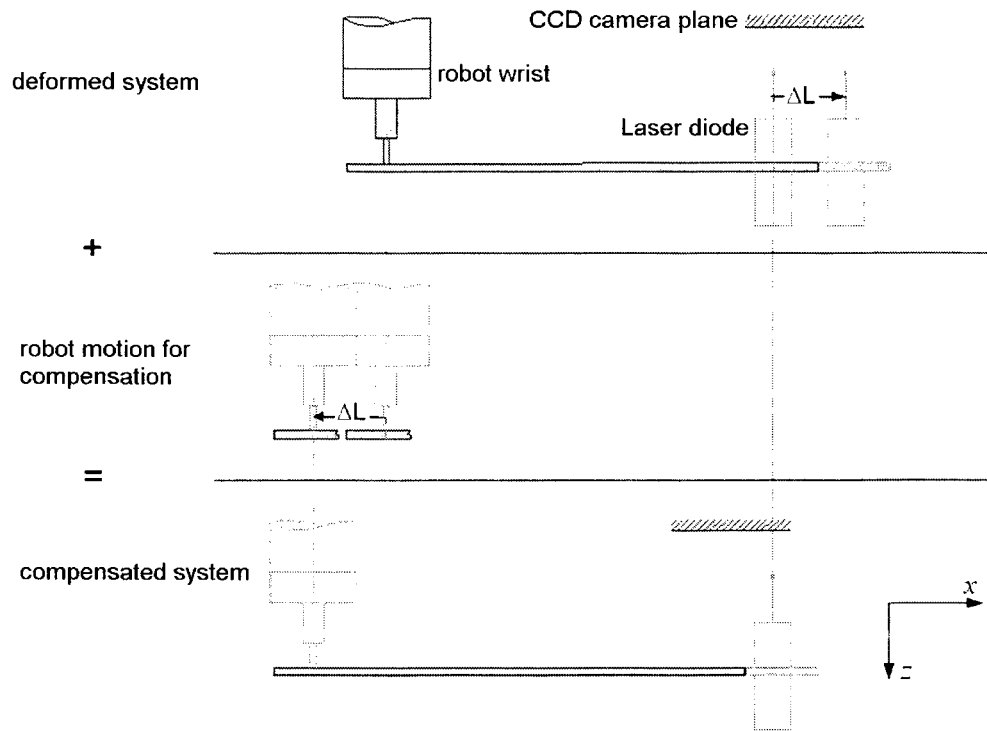


Figure 6.1: Concept of compensation for deformation.

be verified by the stillness of the centroid location throughout transient and steady states.

Validation experiments for the compensation algorithm were performed using input data that was based on deformation results obtained from the predicted models of the two-link experiment (presented in Section 5.5.1). The motions of the A465 robot that were required for the compensation of the deformation were computed and assigned to the controller of the A465 robot through an improved virtual instrument developed in LabVIEW.

For the validation experiment, the virtual instrument was improved from the original version, which was used to communicate between the development computer and robot controller in the single-link and two-link experiments. A module to compute the deformation and required compensation displacements, and forward the corresponding commands to the robot controller was added to the original virtual instrument.

### 6.3 Experimental Apparatus

Since the system was considered rigid in the stationary case, and was assumed to be isolated from any physical disturbances, it was unnecessary to attach the two-link system (*i.e.*, the links and shafts) to the robot tool flange during the validation experiment for this case. The two-link system was removed from the robot to prevent errors that may be caused by a lack of rigidity in the system. The laser diode, which was originally mounted on a link, was secured to a diode holder that was rigidly mounted to the tool flange of the A465 robot, as shown in Figure 6.2. The diode holder was a thick walled cylinder made of ABS plastic for rigidity and heat insulation. The diode was mounted in a position such that the laser beam was aligned with the  $z$ -axis of the robot tool flange and pointed perpendicularly to the CCD chip of the camera. Therefore, the displacement of the laser spot seen by the CCD chip was exactly the displacement of the centre of the tool flange.

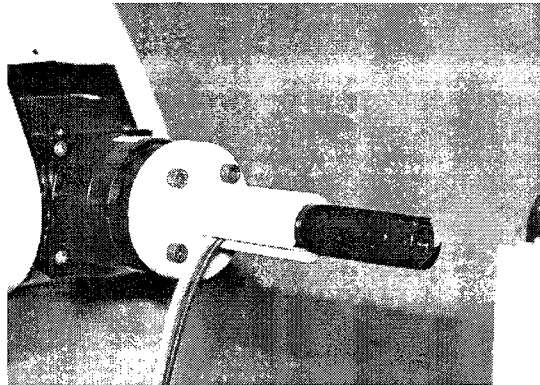


Figure 6.2: Laser diode holder.

Images of the laser spot were acquired by the CCD camera and the laser spot centroid locations were extracted in the same manner to the single-link and two-link experiments. The centroid locations of the laser spot of the compensated system were plotted over time, and were compared to the deformation input obtained from the deformation results of the two-link experiment. IR images were not required for this validation experiment.

In order to enhance the accuracy of results in the validation experiment using the

experimental apparatus developed for the single-link and two-link experiments, a small adjustment to the apparatus was required, due to the repeatability of the A465 robot. As stated in the manufacturer's specification, the repeatability of the A465 robot is  $\pm 50 \mu\text{m}$ . However, to obtain at least 90% overall compensation accuracy, a translation motion required for the first time step was required to be  $1.8 \mu\text{m}$  or smaller. Such a small translation implies that the robot was required to supply displacements smaller than its capability. To allow the robot to work within its capacity, the deformation function was mathematically scaled up to increase the size of the smallest required translation. However, the maximum value for the scaling factor was limited by the dimensions of the CCD chip. The CCD chip width limited the maximum longitudinal deformation that the system can measure. The limitation was that the entire laser spot must appear on the image from the beginning to the end of the experiment. Therefore, given that the width of the chip was  $8,600 \mu\text{m}$ , the maximum scaling factor was limited to 28. This was the maximum value that could accommodate the robot limitations without exceeding the size of the CCD chip.

## 6.4 Compensation Process

The deformation results from the two-link experiment were used as input to compute the total deformation at each time step. The resulting deformations were then used to compute required compensating displacements. Commands that corresponded to the compensation displacements were automatically sent to the robot controller by the LabVIEW virtual instrument discussed earlier. When the commands were executed, *i.e.*, the robot moved according to the commands, the controller then returned a signal to the virtual instrument to acknowledge the execution of the displacement and to initiate deformation data inquiry for a new sequence at the next time step.

To ensure that the tool frame of the two-link system remained at its desired location

at all times during the transient state, the compensation must be provided with time steps that are as small as possible. To obtain such steps, the total deformation of the system must be computed and updated as frequently as possible. However, the size of the time steps was limited by robot execution time and communication speed between the virtual instrument and the robot controller.

### 6.4.1 Finite Difference Model for Deformation

In the two-link experiment, predicted deformations were available from the FEA and finite difference models. However, from a control point of view, using deformation estimates from the FEA as inputs to the compensation calculation could be thought of as being equivalent to using an open-loop control system. Using deformation estimates from the finite difference model could be thought of as it is one step closer to being a closed-loop control system. This is because the predicted deformation estimates obtained from the FEA model were computed from start to finish all at once prior to the compensation process, while the deformation estimates of the finite difference based model were computed on demand at each time step as the deformation progressed<sup>1</sup>.

As stated in Chapter 3, the FEA model was used to cross-check and identify errors in the experimental and finite difference models, and there was no intention to implement the FEA model in the robot controller. Moreover, the FEA model was created separately using ABAQUS and could not be easily integrated into the deformation calculation module of the LabVIEW virtual instrument. On the other hand, the finite difference model was simply implemented as a single equation and can be directly integrated into the deformation calculation module. Additionally, it requires approximately one order of magnitude less computing time.

---

<sup>1</sup>Conceptually FEA results could also be computed and accessed incrementally, however, in this case, the FEA software produced far more data than a simple displacement and was, in addition, located on a workstation some distance from the robot laboratory.

Equation (6.1) represents the finite difference model that was implemented in the deformation calculation module of the virtual instrument:

$$T_i^{p+1} = \frac{\Delta\tau}{C_i} \left[ q_i + \sum_j \frac{T_j^p - T_i^p}{R_{ij}} \right] + T_i^p. \quad (6.1)$$

This model includes conduction, convection and heat supplied by the heating pads. Using this equation, the deformation input was computed on demand for each time step, and the required compensation displacement was determined according to the computed deformation. For example, for a compensation process for the deformation of the two-link system, which had one directional deformation, the compensation was simply the negative function of the deformation function (or  $-y(t)$ ), with the initial condition that at  $t = 0$ , there was no deformation, *i.e.*,  $y = 0$ .

### 6.4.2 Compensation Algorithm

After the predicted deformation value has been obtained at each time step, the deformation calculation module uses it to compute the required compensation. The corresponding displacement to be provided by the A465 robot is then transformed to the robot base coordinate system. The A465 robot uses the RAPL-3 programming language [55]. The default is to use relative displacement commands with respect to the current location. Therefore, an incremental location command was first developed on the compensation algorithm.

Although the results of the first validation experiment using the incremental location command provided acceptable steady state compensation (see Section 6.5), they also revealed unacceptable error during the transient state. It was found that the relative displacement at the core of the incremental location technique was the dominant source of error. A series of incremental displacements of the robot tool flange allowed the errors

in each individual displacement to accumulate. Absolute positioning relative to a single datum can eliminate the increment error stack-up. Therefore, an absolute location command was developed to mitigate the effects of the accumulated errors. Results for each technique are presented in the following subsections.

### 6.4.3 Incremental Location Command

The concept of the incremental location command is illustrated in Figure 6.3. At the start, when  $t = 0$ , the tool frame is set at an operational goal location. The compensation required for the first time step (time step 1) is a translation from the operational goal to the compensation goal location of time step 1. This translation has a magnitude of  $\Delta L_1$  in the negative  $x$  direction with respect to the operational goal location. When the compensation for time step 1 is completed, the deformation computation module will compute the compensation displacement required for the next time step (*i.e.*, time step 2). For time step 2, a translation of  $\Delta L_2$  is required. Assuming no positioning error in the translation of time step 1,  $\Delta L_2$  is measured with respect to the compensation goal location of time step 1 in the negative  $x$  direction. Similarly, and given the same assumption of no positioning error in the translation of time step 2, a translation of  $\Delta L_3$  for time step 3 is measured relative to the compensation goal location of time step 2.

Compensation using the incremental location command has the advantage of programming simplicity in the robot controller. However, in practice, this technique suffers from the accumulation in positioning errors from compensation displacement of each time step. When the positioning errors occur in early time step(s), the sum of the errors may significantly affect the overall compensation accuracy. To eliminate the problem of accumulated errors, the absolute location command was implemented using a different referencing technique. Experimental results presented in Section 6.5 show the improvement in compensation accuracy when the absolute location command is used.

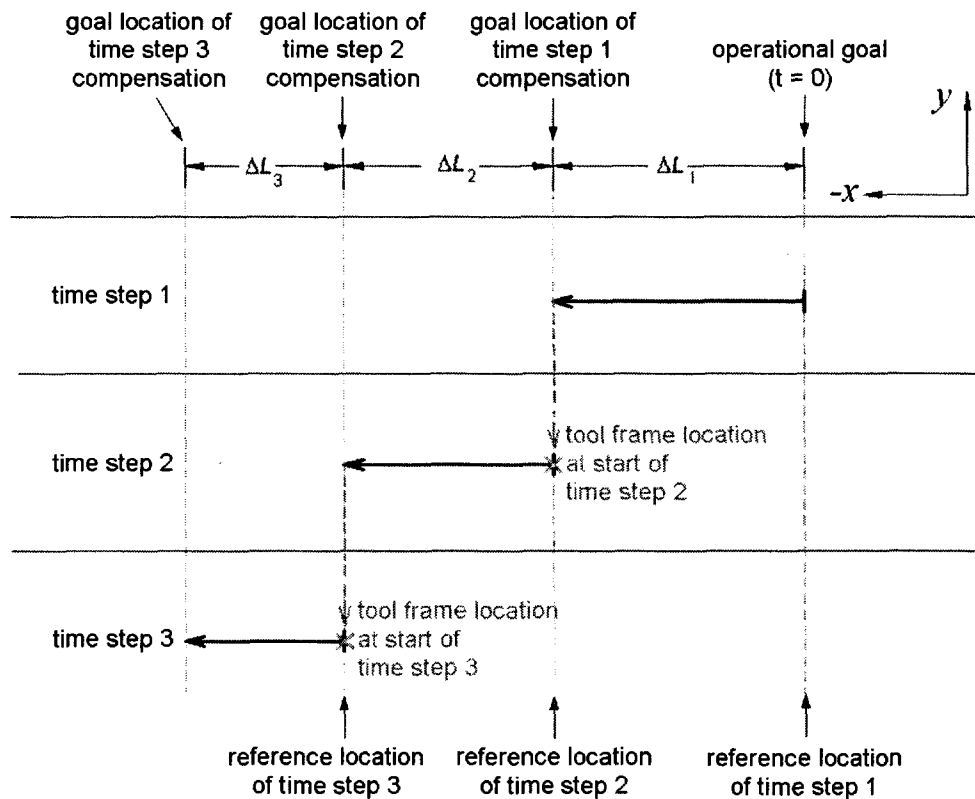


Figure 6.3: Incremental location command.

#### 6.4.4 Absolute Location Command

The reference location of the current tool frame, which varies over time, was replaced by the location of the operational goal of the two-link system, the fixed reference location for the entire compensation process. The robot must still move to the next compensation goal location from its current location, in the same manner as in the incremental location command, but all compensation goals of the absolute location command are assigned relative to the same operational goal location.

The concept of the absolute location command is illustrated in Figure 6.4. As with the incremental location command, the tool frame is set at the operational goal location at the start. For time step 1, there is no change in commands from those of the incremental location commands, because the operational goal is used as a reference for both techniques.

Command modification begins at the start of time step 2, when the tool frame is located at the compensation goal of time step 1. While the actual required translation of time step 2 is  $\Delta L_2$  in the negative  $x$  direction, with respect to the current tool frame location (*i.e.*, the compensation goal of time step 1), the translation for the absolute location command is redefined with respect to the operational goal. Therefore, the translation required for time step 2 becomes  $\Delta L_1 + \Delta L_2$  in the negative  $x$  direction with respect to the operational goal. Similarly, for time step 3, instead of a translation of  $\Delta L_3$  in the negative direction with respect to the compensation goal of time step 2, the translation defined for the absolute location command becomes  $\Delta L_1 + \Delta L_2 + \Delta L_3$  in the negative  $x$  direction with respect to the operational goal.

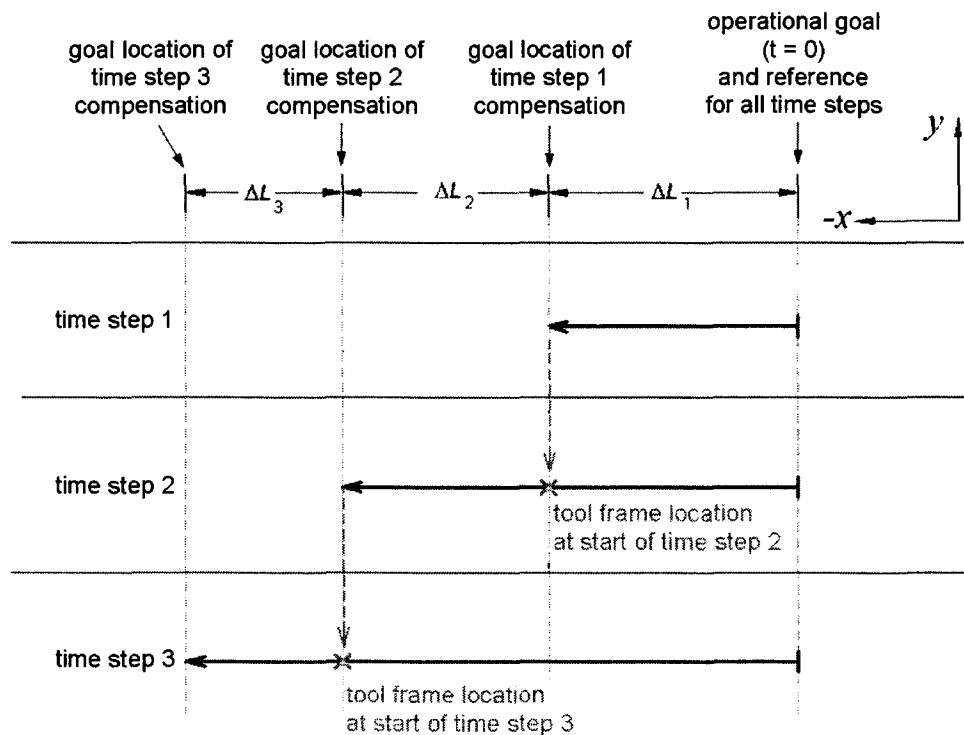


Figure 6.4: Absolute location command.

A major advantage of the absolute location command is that any positioning error that occurs in the translation at each time step can be automatically corrected as part of

the compensation displacement for the following time step, thereby eliminating the error accumulation. The correction is made as part of the process because the robot controller identifies the current tool frame location of the robot and the required displacement for the tool frame to reach the next goal location with respect to only one reference location (*i.e.*, the operational goal) for every time step. Experimental results discussed in the following section confirm that a significant improvement in compensation accuracy was achieved with the use of the absolute location command.

## 6.5 Experimental Results

The temperature-induced deformation that occurred in the stationary case of the two-link experiment was compensated for by the translation of the robot tool flange to which the two-link system was attached. Accuracy of the compensation was analyzed by comparing the compensation displacement, represented by locations over time of the tool frame of the compensated system, with the deformation input. The locations of the tool frame were extracted from laser spot images acquired by a CCD camera during validation experiments.

When the compensation displacement was assigned, an attempt was made to match the amplitude of the compensation curve with the amplitude of the deformation input curve at any given time. The similarity of the amplitudes of the two curves suggests that the translation of the tool frame due to the temperature-induced deformation is compensated for by the compensation displacement of the translation of the same amplitude in the opposite direction. Therefore, the tool frame location remains constant throughout the experiment. The error curve is the summation of the deformation and compensation curves, *i.e.*, a difference in amplitude between the deformation and compensation curves. Ideally, a perfectly compensated system will have a compensation curve that is a mirror image about the  $x$ -axis of the deformation curve and the error curve will have a value of

zero at all times.

Figure 6.5 show the results of the validation experiment for compensation using the incremental location command. Laser centroid locations of the compensated system, are plotted over the 4,800 s and are compared to the deformation input curve. As mentioned in Section 3.6 and Section 5.6 of the single-link and two-link experiments, the direction of the deformation was always assigned to be positive ( $+y(t)$ ). Therefore, the compensation curve, which had the opposite direction of the deformation, was assigned to be negative ( $-y(t)$ ) as seen in the negative portion of the  $y$ -axis of all deformation and compensation result graphs. As expected, the compensation curve shown in Figure 6.5 is close to being a mirror image about the  $x$ -axis of the deformation curve.

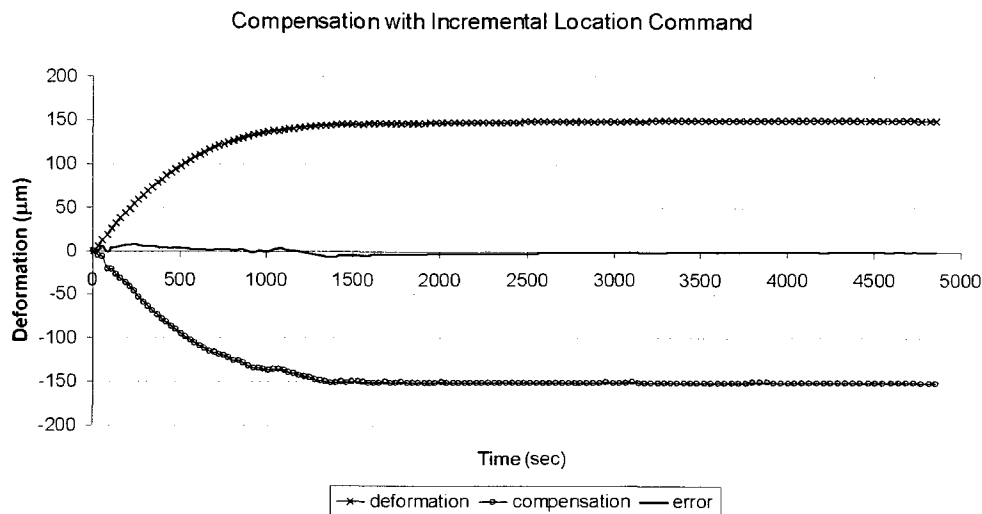


Figure 6.5: Results of validation experiment using incremental location command.

The error curve shows two periods of significant error: during the first 500 s and between 1,200 s and 2,000 s. The maximum error of  $6.38 \mu\text{m}$  is found at approximately 240 s after the start. The steady state error is approximately  $-0.52 \mu\text{m}$  and the mean error of the experiment is  $0.38 \mu\text{m}$ . The negative values on the error curve are obtained when the system is under-compensated. The small errors indicate that the compensation and deformation curves have similar amplitudes during both transient and steady states. The

high similarity in the amplitudes suggests that the deformation of the two-link system can be compensated through translations of the robot tool flange.

Results of the validation experiment for a compensation using the absolute location command are presented in Figure 6.6. The maximum error of  $2.95 \mu\text{m}$  is found at the start. The steady state error is approximately  $-0.15 \mu\text{m}$  and the mean error was  $-0.01 \mu\text{m}$ . The errors remain low in general for the entire experiment and no major difference between the errors of transient and steady states was observed.

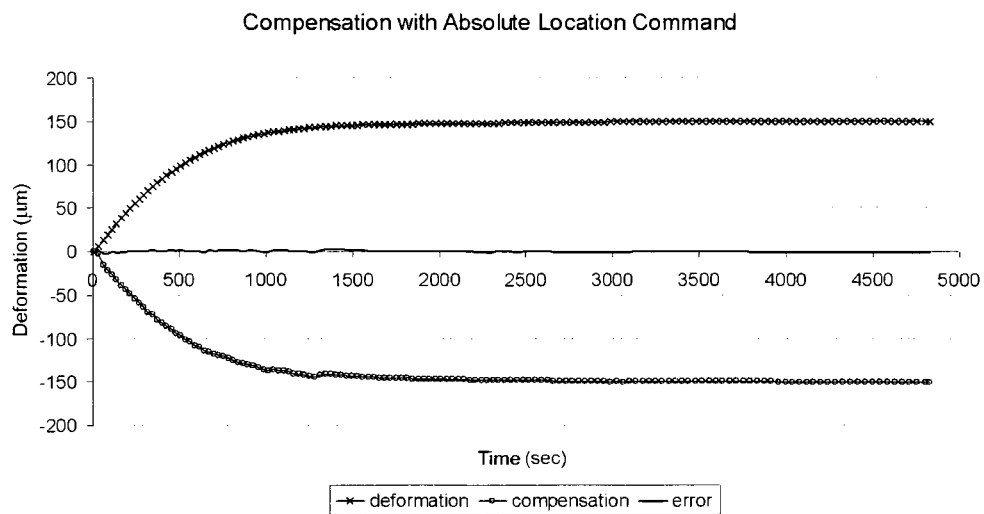


Figure 6.6: Results of verification experiment using absolute location command.

Figure 6.7 illustrates a comparison between results of the incremental and absolute location commands. The deformation curves in both cases are not included on the result comparison graph as they were identical. The absolute location command noticeably improved the compensation accuracy relative to the incremental location command, as can be seen in the reduction of errors during the first 700 s, and between 1,200 s to 3,000 s. A 98% reduction of the mean error was found with the absolute location command compare to the incremental location command. A summary of statistical results from the experiment data is presented in Table 6.1.

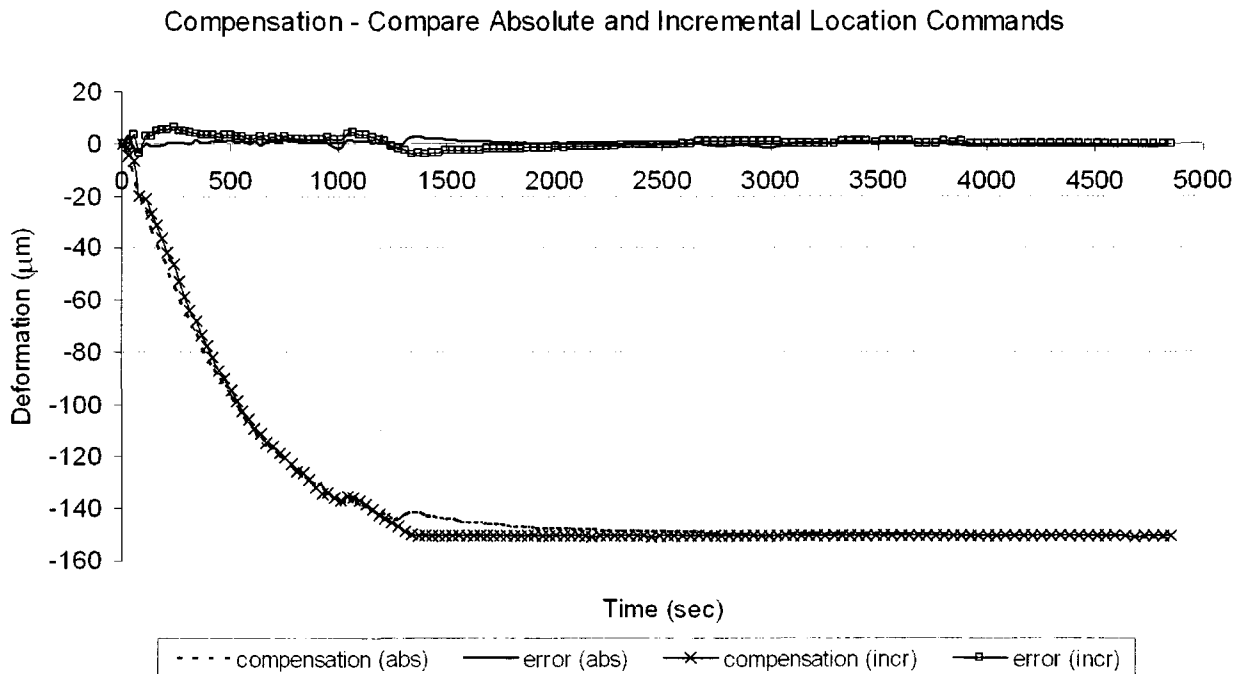


Figure 6.7: Comparison of compensation and error curves between incremental and absolute commands.

## 6.6 Statistical Analysis

In the compensation process, the robot is commanded to move according to deformation input that is computed at each time step. The compensation error is the difference between the actual location of tool frame and targeted location according to the command for the compensation at each time step. The smaller the difference in the locations, the higher the compensation accuracy. To estimate the expected accuracy of the compensation, a statistical analysis of the error was performed. A sample,  $x_i$ , is the error at each time step, and a sample size,  $N$ , is the number of time steps used in the validation experiment. For each experiment the sample mean,  $\bar{x}$ , is computed. If each sample set is normally distributed, then the data set consisting of the  $\bar{x}$ 's from those sample sets is also normally distributed [41]. The standard deviation of this data set is called the standard deviation of the means,  $S_{\bar{x}}$ . The standard deviation of the means is a measure of the precision of

the sample mean that indicates how it is distributed about the true mean value.

The standard deviation of the means can be obtained experimentally through a number of repeated experiments, as well as statistically estimated from the value of the standard deviation of just one normally-distributed data set using the following equation [41]:

$$S_{\bar{x}} = \frac{S_x}{\sqrt{N}}.$$

First, all data sets must be verified to be normally distributed. To verify that the errors from both the incremental and absolute location commands of the validation experiment, presented in both Figure 6.5 and Figure 6.6, are normally distributed, the chi-squared ( $\chi^2$ ) goodness-of-fit test is applied to the data [41]. This test quantifies how well the data are governed by the assumed distribution compared to the possibility that the data are not drawn from the assumed distribution. The  $\chi^2$  value is calculated from a histogram as

$$\chi^2 = \sum_{j=1}^K \frac{(n_j - n'_j)^2}{n'_j}, \quad (6.2)$$

where  $n_j$  is the observed number of occurrences and  $n'_j$  is the predicted number of occurrences in the  $j^{th}$  interval based on the presumed probability density function.

For a given degree of freedom, the lower the  $\chi^2$  value, the better a data set fits the assumed distribution. The degree of freedom in the variance for the data set,  $\nu$ , is calculated as:

$$\nu = K - m,$$

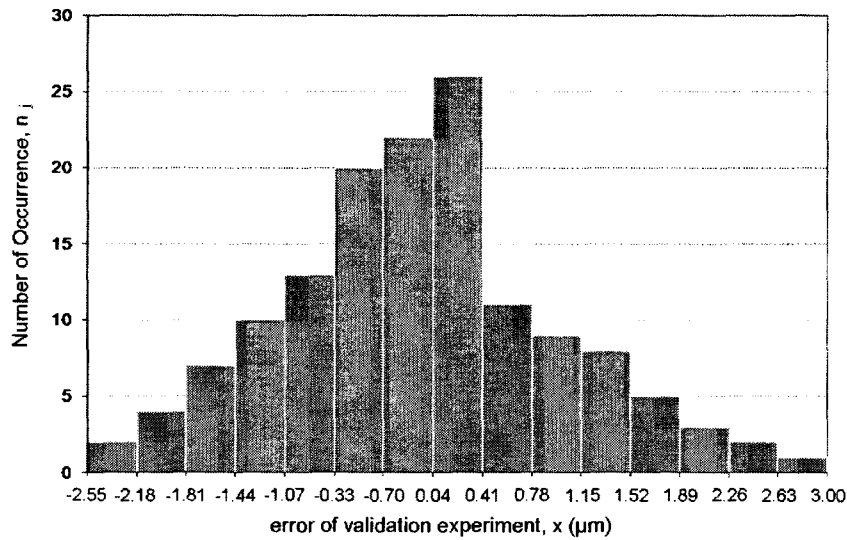
where  $K$  is the number of intervals in the histogram and  $m$  is the number of statistical parameters calculated with the existing data. For  $\chi^2$ , two calculated statistical parameters ( $\bar{x}$  and  $S_x$ ) are used, therefore  $\nu = K - 2$  for the data sets used in the experiments. Generally, if the probability  $P(\chi^2)$  is less than 0.05 (*i.e.*,  $P(\chi^2) < 5\%$ ), it can be concluded that there is a strong measure of good fit between the observed data and the assumed distribution.

A histogram of errors was constructed from the data set. For  $N > 40$ , number of intervals,  $K$ , required for a viable statistical analysis can be estimated [41] from:

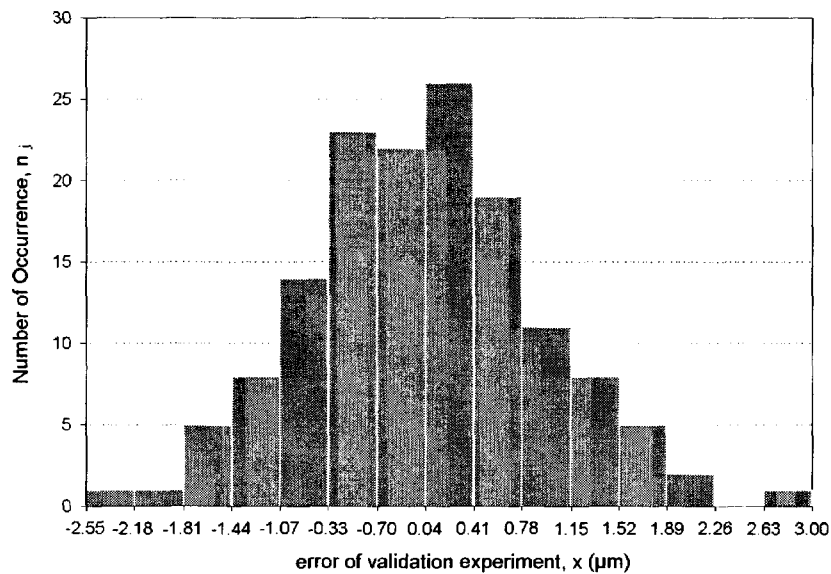
$$K = 1.87(N - 1)^{0.40} + 1.$$

The sample size  $N$  is the total number of time steps. For the experiments reported here,  $N$  is 143 for both incremental and absolute location commands. For  $N = 143$ ,  $K$  is found to be 15, and therefore  $\nu$  is 13. The intervals and  $n_j$  of the incremental and absolute location commands are listed in Tables C.1 and C.2 in Appendix C. The histograms are shown in Figure 6.8.

Next, the  $n'_j$  for each interval was predicted based on a normal distribution using  $n'_j = N \times P(j^{\text{th}} \text{ interval})$ . The probabilities of each interval (*e.g.*,  $P(-4.40 \leq x < -3.68)$  for the first interval,  $j = 1$ , in Table C.1) was computed based on the  $z$  statistic values. The values of  $n_j$ ,  $n'_j$  and  $\frac{(n_j - n'_j)^2}{n'_j}$  for all intervals, with the  $\chi^2$  based on Equation (6.2) are listed in Table C.3 for the incremental location command and Table C.4 for the absolute location command in Appendix C. From Table C.3,  $\chi^2 = 6.48$  in the incremental location



(a) Errors from incremental location command (data in Table C.1).



(b) Errors from absolute location command (data in Table C.2).

Figure 6.8: Histograms.

command case, and from Table C.4,  $\chi^2 = 5.66$  in the absolute location command case.

In the incremental location command case, for  $\chi^2 = 6.48$  and  $\nu = 13$ ,  $P(\chi^2) = 0.0733$  or 7.33%. In the absolute location command case, for  $\chi^2 = 5.66$  and  $\nu = 13$ ,  $P(\chi^2) = 0.0425$  or 4.25%. With the value of  $P(\chi^2)$  less than 0.05 in the absolute location command case, the hypothesis that the data set consists of the errors from the absolute location

commands of the validation experiment is normally distributed is accepted to be true. In the incremental location command case, although the value of  $P(\chi^2)$  is greater than 0.05, the difference of 2.33% suggests that it is still very likely that the data are normally distributed.

If the errors are accepted as normally distributed, they can be used to statistically estimate the standard deviation of the mean. The sample size,  $N$ , or the total number of time steps, is 143 for both incremental and absolute location commands. From the results of the incremental location command, the standard deviation,  $S_x$ , of the sample is  $2.11 \mu\text{m}$ . Using Equation (6.2), the standard deviation of the mean is  $0.18 \mu\text{m}$ . Similarly, from the results of the absolute location command,  $S_x$  was  $0.92 \mu\text{m}$ , and  $S_{\bar{x}}$  was  $0.08 \mu\text{m}$ . All statistical results together with % improvement of the statistical results of the absolute location commands compared to those of the incremental location commands are summarized in Table 6.1.

Table 6.1: Statistical results.

	symbol	Incremental	Absolute	% improvement
Sample size	$N$	143	143	-
Mean	$\bar{x}$	0.376	0.007	98.16
Standard deviation	$S_x$	2.107	0.921	56.31
Standard deviation of the mean	$S_{\bar{x}}$	0.176	0.077	56.31

Results from the statistical analysis confirmed that the absolute location command provided higher accuracy compensation than the incremental location command. The standard deviation of the means of  $0.08 \mu\text{m}$  is approximately 1.5% of the value of the data range, which is shown in Figure 6.7 to be  $5.47 \mu\text{m}$ . Such a small value of the standard deviation of the mean indicates that the accuracy of the compensation is expected to be consistently high.

## 6.7 Discussion

A set of straight-forward equations, based on the finite difference model, was implemented in the deformation calculation module. Deformation input was computed on demand, and the corresponding compensation motion was executed automatically according to the commands from the LabVIEW virtual instrument. Therefore, the goal of developing an algorithm for an automated system to compensate temperature-induced deformation has been demonstrated.

The compensation strategy requires time steps to be as small as possible. However, the length of the time step was limited by the communication speed between the development computer that runs the LabVIEW virtual instrument and the robot controller. The limitation of communication speed had an impact on compensation accuracy. This was especially significant during the first 60 s when a change in deformation was much more drastic, and therefore, would require shorter time steps than the rest of the compensation process. The errors of the first two time steps were found to be ten times greater than the mean error. Therefore, the average error during the transient state was higher than during the steady state. Nevertheless, the accuracy of the compensation was acceptable as the maximum error was only 1.9% of the maximum deformation expected at steady state.

The results reveal that only a minor difference between amplitude of deformation and compensation (*i.e.*, error) was observed. The low error implies that if the temperature-induced deformation of the two-link system is compensated during the experiment, the locations of the laser spot centroid will remain at the location of the operational goal throughout the whole experiment.

To verify the success of the compensation algorithm, the deformation of this compensated system was compared to the deformation of the same system when it was not compensated. The stationary case of the two-link system was compensated for in the

validation experiment, hence, the error observed in the validation experiment was the deformation of the two-link system after compensation. Therefore, for this comparison of the compensated and uncompensated systems, the deformation of the compensated system was represented by the errors of the compensation using the absolute location command (see Figure 6.6). The deformation of the uncompensated system was represented by the deformation results of the stationary case of the two-link experimental model (see Figure 5.7).

Figure 6.9 is a comparison of the deformations of the compensated and uncompensated systems. Here, the maximum change in location of the end-effector of the uncompensated

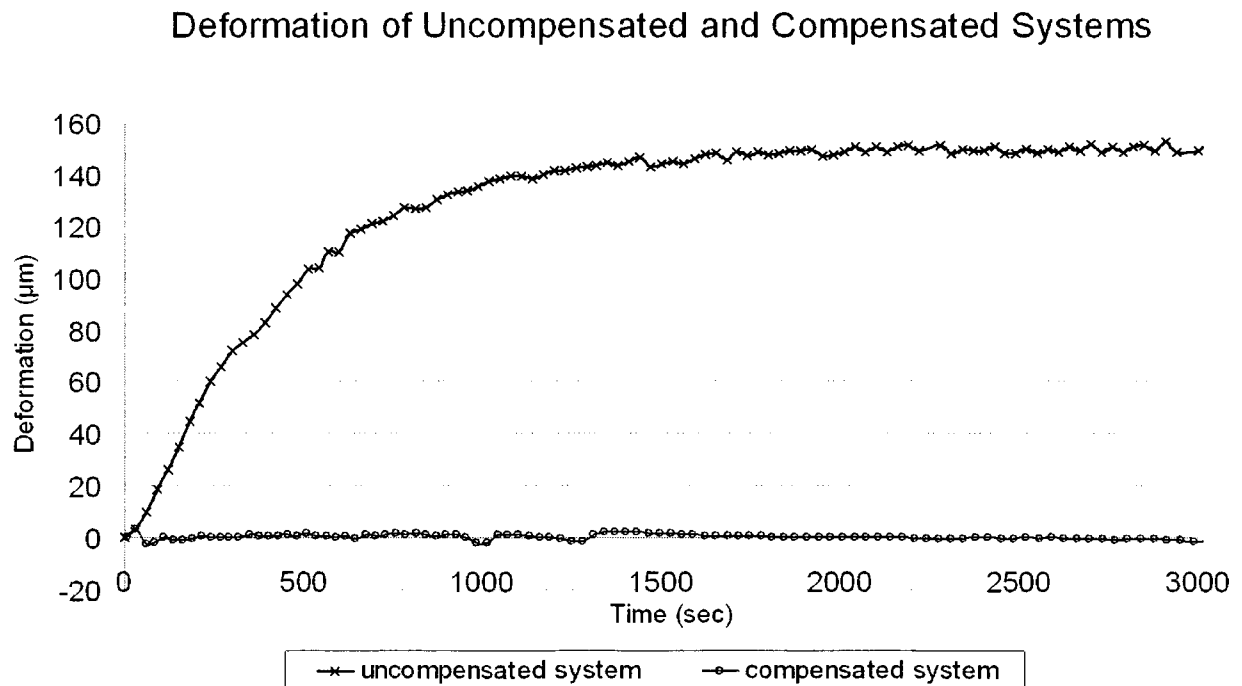


Figure 6.9: Deformation of compensated and uncompensated systems.

two-link system is approximately 150  $\mu\text{m}$ , while that of the compensated two-link system is approximately 3  $\mu\text{m}$ . With the compensation, the change in location of the end-effector of the two-link system was reduced by approximately 98%, and the mean deformation became very close to be zero microns (0.007  $\mu\text{m}$ ). The transient state of the uncompensated system

lasts 520 s, while the compensated system virtually has no transient state. The absence of the transient state in the compensated system indicates that the warm-up period of the system is no longer required. The substantially improved position of the end-effector and the elimination of the transient state are the major improvement of the performance of the two-link system thereby confirming the effectiveness of the compensation algorithm.

# Chapter 7

## Conclusions and Future Work

### 7.1 Conclusions

A means for correcting the temperature-induced deformation in a simplified robot mechanical system has been presented. When compensated, the positioning error caused by deformation of the system is decreased by as much as 98% and the effects of the transient state of the deformation as a function of time are virtually eliminated. The important implication is that warm-up cycles, which are typically required for industrial robots or any mechanical systems that undergo deformation due to changes in temperature during transient states, may be reduced or eliminated. The successful elimination of the warm-up cycles in the simplified robot mechanical systems examined here suggests the possibility of compensating temperature-induced deformations for industrial robot mechanical systems using a suitably adapted algorithm implemented in the robot controller.

When the deformation of the robot mechanical system is compensated, and the requirement for warm-up cycles is eliminated, the natural outcome is that the performance of the robot will be improved in several ways. First, the productivity of a robot workcell will be enhanced as the robot will be able to perform useful work during the time that is normally

required for the warm-up cycle. This means that unnecessary energy consumption during the warm-up cycles will be eliminated. Additionally, the overall positioning repeatability and accuracy of the robot will be improved because of the decrease in drift of pose and orientation repeatability.

During the development phase of this research, a non-contact measurement system was developed to experimentally determine temperature-induced deformation. The non-contact measurement system consisted of two optical measurement systems for deformation and temperature measurements of the simplified robot mechanical system links. The link deformation was measured by tracking the drift of a laser diode spot across the CCD camera chip. The temperature measurements were obtained using an infrared camera. This experimental technique worked in concert with a thermal-mechanical predictive finite element analysis (FEA) to develop a 1-D finite difference model that was incorporated into the robot controller algorithm to provide compensation. The use of the FEA model allowed cross-checking of the results, which was particularly important for the single-link and two-link experiments as errors in the experimental model had to be identified and overcome.

A significant improvement was achieved in the performance of the deformation measurement system. The deformation of the camera stand was found to be a significant source of error in the measurements made with the CCD camera. This deformation was caused by heat generated during the working period that was transferred to the camera stand. The transferred heat was reduced by adding heat fins to allow the heat to be released to the environment faster, adding insulation between the camera and the stand, and warming-up the camera prior to acquiring images for a measurement.

The laser spot centroid extraction algorithm was improved by allowing users to set a threshold value of the lowest and highest intensity to be used for each extraction. The use of the lowest threshold value reduced uncertainty of the extraction algorithm associated

with the inconsistency of laser intensity and location around the edge of the laser spot. The highest threshold value allowed all shades of gray pixels with intensity higher than the highest threshold value to be considered as white pixels. The use of suitable threshold values of intensity improved the accuracy of the extraction especially in sets of low quality images. It was also found that higher quality images were obtained with a large laser spot. The large spot offered more white pixels, thereby reducing the fluctuation in area and intensity distribution of laser spot.

An improved virtual instrument developed in LabVIEW facilitated communication between the development computer, CCD camera, infrared camera and robot controller. For the experimental analysis of the simplified robot mechanical systems, deformation and temperature results were obtained simultaneously and automatically. The virtual instrument also had a module to compute the deformation using an equation based on the finite difference model and calculated the required compensation motions. Through the virtual instrument, the corresponding commands were forwarded to the robot controller, and when the commands were executed, a deformation data inquiry was initiated for the next time step.

The automated system, based on a set of straight-forward equations, provided substantially improved positioning of the end-effector of the simplified robot mechanical system. The compensation algorithm using absolute positioning relative to a single datum for the entire compensation process improved the positioning repeatability of the end-effector by up to 98%. The results of the statistical analysis on the errors obtained in the compensation algorithm validation experiment confirmed that high accuracy compensation can be consistently expected.

## 7.2 Future Work

The future work for this research may be categorized into two main topics: work related to the compensation of the temperature-induced deformation in robot mechanical systems, and work related to an improvement of the non-contact measurement system.

### 7.2.1 Compensation for Temperature-Induced Deformation

The reasonable accuracy of the compensation algorithm for the simplified robot mechanical system observed in this research suggests that the algorithm should be adapted to more complex systems. The ultimate goal of this improvement is compensation for deformation in an actual industrial robot mechanical system. As most tasks of industrial robots consist of repetitive motion sequences, and are taught off-line prior to the operation, the temperature-induced deformation can be predicted using the known trajectory and loads. Therefore, the compensation can be computed off-line and stored in the controller *a priori*.

The next step toward the goal is the study of 2-D and 3-D heat transfer of more complex dimensions and features. The study should focus on constraints due to the complicated dimensions or features of the objects. The study is also required for the finite difference models of the 2-D and 3-D systems. With a study of 3-D heat transfer of a robot mechanical system and a study of material properties of all parts comprising the robot, the 3-D finite difference model can be constructed and implemented in the robot controller for compensation. An open-architecture robot controller is required for this. Accessible joint controllers will allow torque commands to be edited using the coefficients computed for the temperature-induced deformation and sent directly to the robot motors through the controller. However, with the compensation through the open-architecture, a faster rate of communication between the development computer and the robot controller will be required.

### 7.2.2 Improvement of the Non-Contact Measurement System

With some development, the non-contact measurement system will have the ability to perform measurement of temperature-induced deformation in 3-D. It can also be applied to a broader range of applications in a variety of electro-mechanical devices.

To allow 3-D deformation measurement, two new pairs of CCD and infrared cameras are required. Each pair of cameras should be orthogonally mounted to record the changes in both dimension and temperature in the  $x$ -,  $y$ - and  $z$ -axes directions, *i.e.*, one pair of cameras per direction.

To improve the accuracy of the deformation measurement, which is affected strongly by the accuracy of the laser spot extraction algorithm, a calibration of the CCD coordinates as functions of rows and columns of CCD grid is required. The laser spot will also be replaced with a structured laser line to eliminate errors caused by the unexpected relatively poor image quality. The advantages of a line coordinate approach include the ability to measure temperature-induced changes in location of the robot reference tool point, but also changes in tool orientation as well by determining changes in the laser line angle in subsequent images. The current laser extraction algorithm based on geometric centroid could be updated to use Plücker line coordinates.

# Bibliography

- [1] *ISO 8373, Manipulating industrial robots - Vocabulary*, Std. ISO standard 8373:1994, May 1996.
- [2] J. Craig, *Introduction to Robotics, Mechanics and Control*, 2nd ed. Reading, MA: Addison-Wesley Publishing Co., 1989.
- [3] Y. Edan, L. Friedman, A. Mehrez, and L. Slutski, “A Three-dimensional Statistical Framework for Performance of Robotic Systems,” *Robotics and Computer-Integrated Manufacturing*, vol. 14, pp. 307–315, 1998.
- [4] J. Merlet, *Parallel Robots*. Dordrecht, The Netherlands: Kluwer Academic Publishers, 2000, pp. 183–184.
- [5] M. Leitner, M. Hayes, R. Ofner, and C. Sallinger, “Repeatability of Industrial Robots,” Institute for Automation, University of Leoben, Austria, Tech. Rep., July 2000.
- [6] *KR15 Technical Data: Operating Handbook*, KR C1 Release 2.2, KUKA Roboter GmbH.
- [7] *A465 Robot System User Guide*, UMI-A465-400, Thermo CRS Ltd., July 2002.

- [8] T.-F. Niaritsiry, N.Fazenda, and R.Clavel, "Simulation Analysis of the Sources of Inaccuracy of a Parallel Manipulator," in *Proc. IEEE Int. Conf. on Robotics, Intelligent Systems and Signal Processing (RISSP)*, Changsha, China, October 2003.
- [9] M. Hayes, M. Husty, and P. Zsombor-Murray, "Singular Configurations of Wrist-Partitioned 6R Serial Robots: a Geometric Perspective for Users," *Transactions of the CSME*, vol. 26, no. 1, pp. 41–55, 2002.
- [10] P. Poonyapak, M. Hayes, and J. McDill, "Temperature-Induced Deformation in a Mechanical System," in *Proc. 12th IFToMM World Congress*, Besancon, France, June 2007.
- [11] *ISO 9283, Manipulating industrial robots - Performance criteria, and related test methods*, Std. ISO standard 9283:1998(E), April 1998.
- [12] C. Gong, J. Yuan, and J. Ni, "Nongeometric Error Identification and Compensation for Robotic System by Inverse Calibration," *International Journal of Machine Tools and Manufacture, Design, Research and Applicaiton*, vol. 40, pp. 2119–2137, 2000.
- [13] P. Ngernthong, Thai Auto Works, Co., Ltd., December 2007, private communication.
- [14] M. Leitner, M. Hayes, R. Ofner, C. Sallinger, and P. O'Leary, "Thermal Effects and Consequences for Repeatability of an Industrial Robot," in *Proc. 18th Canadian Congress of Applied Mechanics (CANCAM)*, St. John's, NF, Canada, 2001, pp. 299–300.
- [15] P. Poonyapak, J. McDill, and M. Hayes, "Improving Robot Efficiency to Reduce Energy Consumption," in *ICWES14 International Network of Women Engineers and Scientists*, Lille, France, July 2008.

- [16] (2007, December) The motoman website. Motoman, Inc. [Online]. Available: <http://www.motoman.com>
- [17] (2007, December) Energy Audit. Ontario Energy Board. [Online]. Available: <http://www.powerwise.ca>
- [18] (2007, June) Energy Statistics. CIA World Factbook. Central Intelligence Agency (CIA). [Online]. Available: <http://www.nationmaster.com>
- [19] (2007, October) Electricity Prices for Regulated Price Plan Consumers. Ontario Energy Board (OEB). [Online]. Available: <http://www.oeb.gov.on.ca>
- [20] O. F. Offodile and K. Ugwu, "Evaluating the Effect of Speed and Payload on Robot Repeatability," *Robotics and Computer-Integrated Manufacturing*, vol. 8-1, pp. 27–33, 1991.
- [21] B. Mooring and T. Pack, "Aspects of Robot Repeatability," *Robotica*, vol. 5, pp. 223–230, 1987.
- [22] J. Jeswiet and R. Helferty, "Measuring Robot Repeatability [sic] an Application of ISO and ANSI Standards," *Advanced Robotics*, vol. 10, no. 5, pp. 503–520, 1996.
- [23] J. Hollerbach and C. Wampler, "The Calibration Index and Taxonomy for Robot Kinematic Calibration Methods," *International Journal of Robotics Research*, vol. 15, pp. 705–712, 1996.
- [24] N.Fazenda, T.-F. Niaritsiry, and R.Clavel, "Simulation-Based Kinematic Modeling of a High Precision Parallel Manipulator," in *Proc. 9th IEEE Int. Conf. on Methods and Models in Automation and Robotics*, Miedzyzdroje, Poland, August 2003.
- [25] S. Hayati, "Robot Arm Geometric Link Parameter Estimation," in *Proc. 22nd IEEE Conf. on Decision and Control*, San Antonio, TX, 1983, pp. 1477–1483.

- [26] C. Wampler, J. Hollerbach, and T. Arai, "An Implicit Loop Method for Kinematic Calibration and its Application to Closed-Chain Mechanisms," *IEEE Trans. Rob. Autom.*, vol. 11, no. 5, pp. 710–724, 1995.
- [27] K. Grossmann, B. Wunderlich, and S. Szatmari, "Progress in Accuracy and Calibration of Parallel Kinematics," in *Proc. Parallel Kinematic Machines in Research and Practise: the 4th Chemnitz Parallel Kinematics Seminar*, Chemnitz, Germany, 2004, pp. 49–68.
- [28] Y. Hatamura, T. Nagao, M. Mitsuishi, K. Kato, S. Taguchi, T. Okumura, G. Nakagawa, and H. Sugishita, "Development of an Intelligent Machining Center Incorporating Active Compensation for Thermal Distortion," *Annals of the CIRP*, vol. 42/1/1993, pp. 549–552, 1993.
- [29] P. Poonyapak and M. Hayes, "Towards a Predictive Model for Temperature-Induced Deformation of an Industrial Robot," in *Proc. EuCoMeS, the First European Conference on Mechanism Science*, Obergurgl, Austria, February 2006.
- [30] P. Poonyapak, J. McDill, and M. Hayes, "Experimental Error in Measuring Temperature-Induced Deformation in a Single-Link System," in *Proc. RAAD 2008, 17th International Workshop on Robotics in Alpe-Adria-Danube Region*, Ancona, Italy, September 2008.
- [31] C. Chen and A. Kak, "Modeling and Calibration of a Structured Light Scanner for 3-D Robot Vision," in *Proc. IEEE Int. Conf. on Robotics and Automation*, vol. 4, 1987, pp. 807–815.
- [32] R. Rohling, P. Munger, J. M. Hollerbach, and T. Peters, "Comparison of Relative Accuracy Between a Mechanical and an Optical Position Tracker for Image-Guided Neurosurgery," McGill University, Montreal, Tech. Rep., 1994.

- [33] M. Vincze, J. Prenniger, and H. Gander, "A Laser Tracking System to Measure Position and Orientation of Robot End Effectors Under Motion," *The International Journal of Robotics Research*, vol. 13, no. 4, pp. 305–314, August 1994.
- [34] A. Fratpietro and M. Hayes, "Relative Measurement for Kinematic Calibration Using Digital Image Processing," in *Proc. CSME Forum 2004*, University of Western Ontario, London, Canada, June 2004, pp. 758–767.
- [35] R. Winn and C. Morin, "Low Cost Shadowgraph Technique for Flammable Vapor Visualization," in *Proc. IECEC-97*, vol. 1, Honolulu, Hawaii, 1997, pp. 642–647 692.
- [36] E. Goodwin and J. Wyant, *Field Guide to Interferometric Optical Testing*. Bellingham, Washington: SPIE Press, 2006.
- [37] L. Cheng. (2009, May) Measuring Nanometers with Light. TNO. [Online]. Available: <http://www.tno.nl>
- [38] G. Plantier, N. Servagent, A. Sourice, and T. Bosch, "A Low-Cost Optical Feedback Interferometer for Real-Time Velocity Measurement," in *Proc. 17th IEEE Instrumentation and Measurement Technology Conf.*, Baltimore, Maryland, May 2000, pp. 738–743.
- [39] N. Simpson and M. Hayes, "Simulation of Kinematic Calibration Procedure that Employs the Relative Measurement Concept," in *Proc. CSME Forum 2004*, University of Western Ontario, London, ON, Canada, June 2004, pp. 684–692.
- [40] J. P. Holman, *Heat Transfer*, 7th ed. NY: McGraw-Hill Inc., 1990, pp. 149–171.
- [41] R. Figliola and D. Beasley, *Theory and Design for Mechanical Measurements*, 3rd ed. New York, NY: John Wiley & Sons, Inc., 2000.

- [42] S. Lampman, *Metals Handbook - Volume 2 Properties Selection: Nonferrous Alloys and Special-purpose Materials*, 10th ed. Metals Park, OH: ASM International, 1990.
- [43] (2009, May) The KUKA Website. KUKA Roboter GmbH. [Online]. Available: <http://www.kuka-robotics.com>
- [44] R. Ofner, P. O'Leary, and M. Leitner, "A Collection of Algorithms for the Determination of Construction Points in the Measurement of 3D Geometries via Light-Sectioning," *Wesic '99, 2nd Workshop on European Scientific and Industrial Collaboration promoting: Advanced Technologies in Manufacturing*, 1999.
- [45] H. Boyer and T. Gall, *Metals Handbook: Desk Edition*. Metals Park, OH: ASM International, 1985.
- [46] *FLIR Systems Thermovision TM A40M Operation's Manual*, FLIR Systems AB, Danderyd, Sweden, October 2004.
- [47] *ThermaCAM TM Researcher User's Manual*, Professional edition. Version 2.8 SR-1, FLIR Systems AB, Danderyd, Sweden, November 2004.
- [48] R. Jain, R. Kasturi, and B. Schunck, *Machine Vision*. NY: McGraw-Hill Inc., 1995.
- [49] *ABAQUS/CAE version 6.4.1*, ABAQUS Inc., Providence, RI, 2003.
- [50] C. A. Dostal, *Engineered Materials Handbook Volume 2: Engineering Plastic*. Metals Park, OH: ASM International, 1988.
- [51] H. Bui. (2008, August) Fracture Mechanics. Springer Netherlands. [Online]. Available: <http://www.springerlink.com.proxy.library.carleton.ca>
- [52] K. Chawla, *Composite Materials: Science and Engineering*. New York, NY: Springer-Verlag New York Inc., 1987.

- [53] D. Askeland, *The Science and Engineering of Materials*, 2nd ed. Boston, MA: PWS-KENT Publishing Company, 1989.
- [54] (2008, November) Dupont Kapton Polyimide Film Specifications. Boedeker Plastics, Inc. [Online]. Available: <http://www.boedeker.com>
- [55] *RAPL-3 Language Reference Guide*, CRS Robotics Corporation, Burlington, ON, 2000.

# Appendix A

## MATLAB Algorithms

### A.1 Laser Spot Centroid Extraction Algorithm

The laser spot centroid extraction algorithm was developed in MATLAB to extract the locations of laser spot centroids. The algorithm also provides the distribution of intensity levels of each laser spot image, and the maximum intensity of the image.

The input for the extraction was a set of laser spot images (approximately 100 - 200 images) acquired by the CCD camera from each case of experiment. The images were in .jpg format. Important information extracted from each image is the location of the laser spot centroid, and the duration from the start of the experiment that the image was acquired.

For each extraction using this algorithm, four results were obtained:

- locations of the centroid in  $x$ -axis.
- locations of the centroid in  $y$ -axis.
- intensity distribution of each images.
- maximum intensity of each images.

All results were provided with respect to the duration from the start of the experiment, which was converted from the image numbers using the recording speed of the CCD camera.

Figure A.1 shows the coordinates of the laser spot over time presented separately in  $x$ - and  $y$ - axes directions.

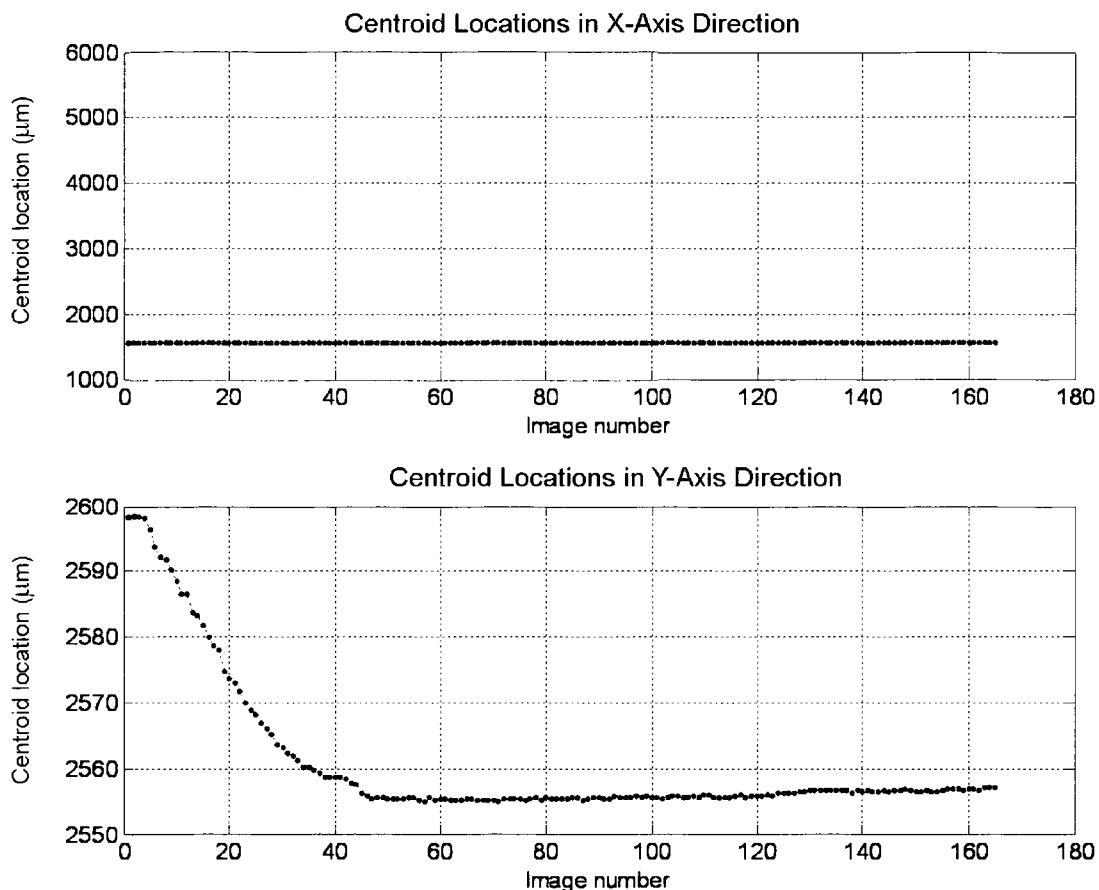


Figure A.1: Location of laser spot centroids in  $x$ - and  $y$ - axes directions.

The intensity distribution and the maximum intensity of each image in the sample image set are presented in Figure A.2 and Figure A.3 respectively.

Two MATLAB codes were used in the extraction algorithm, *find\_computed\_trajectory* and *extract\_centroid*. The first code, *find\_computed\_trajectory*, was the main body of the extraction algorithm. The second code, *extract\_centroid*, was the function that performed the sub-pixel moment calculations and provided the coordinates of the laser spot centroid

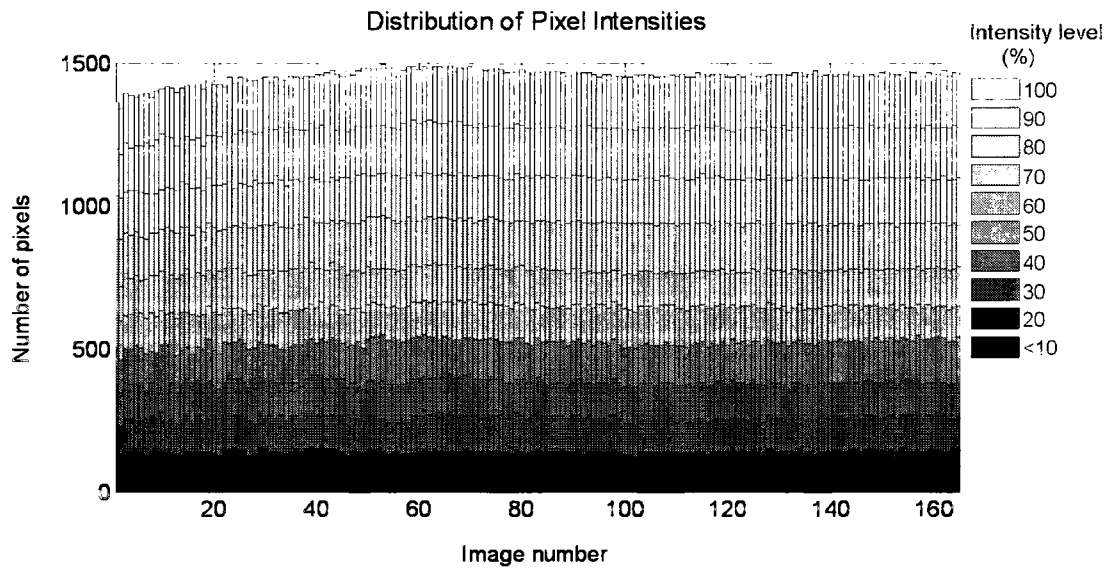


Figure A.2: Intensity distribution of each laser spot image.

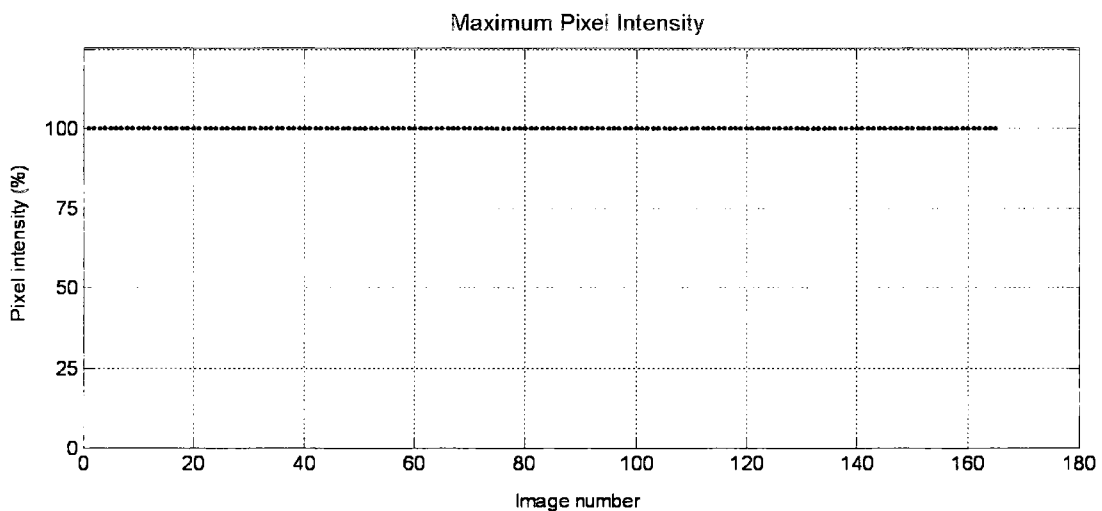


Figure A.3: Maximum intensity of each laser spot image.

of each laser spot image. Both codes are presented below.

For an extraction of a set of laser spot images from each experiment, all images must be located in the same folder as the MATLAB codes. To start the extraction algorithm, *find\_computed\_trajectory* was executed. The first image was read, and values were assigned to each pixel according to its intensity, one image at a time. The intensity values and their

pixel locations were then forwarded to the function *extract\_centroid* for the extraction of the centroid location using the sub-pixel moment calculations. The coordinate of the centroid of the laser spot obtained from *extract\_centroid* was sent back to the the main body of the algorithm and recorded for plotting against the image number (which was later converted into the time duration from the start of the experiment). When the extraction was completed for the first image, the process was repeated for the next one. The extraction was completed one image at the time for all images in the image set.

MATLAB codes for both *find\_computed\_trajectory* and *extract\_centroid* are presented below.

```

%%%%%%%%%%%%%%%%%%%%%%%%%%%%%%%%%%%%%%%%%%%%%%%%%%%%%%%%%%%%%%%%%%%%%%%%
% Name      : find_computed_trajectory.m
% Author    : Pranchalee Poonyapak
% Created   : January 2005
% Description : For a set of images acquired from the CCD camera,
%              extract centroid coordinates of the laser spot,
%              convert into deformation in x- and y- axes
%              directions, plot and save the data in an excel file
%%%%%%%%%%%%%%%%%%%%%%%%%%%%%%%%%%%%%%%%%%%%%%%%%%%%%%%%%%%%%%%%%%%%%%%%

close all; clear all; clc;

%%%%%%%%%%%%%%%%%%%%%%%%%%%%%%%%%%%%%%%%%%%%%%%%%%%%%%%%%%%%%%%%%%%%%%%%
%% Global variables declaration
%%%%%%%%%%%%%%%%%%%%%%%%%%%%%%%%%%%%%%%%%%%%%%%%%%%%%%%%%%%%%%%%%%%%%%%%

global g_x g_y g_high g_nbPixel TRESHOLD SIZEBOX MAXIMUM

```

%%%

SIZEBOX = 400;

% with the highest value

% Extract a box of size SIZEBOX around the pixel

isRoundPixel = 0.0;

% In all cases, below TRESHOLD, it is set to 0

% = 0 means the value of the pixel above TRESHOLD is left as is

% = 1 means the value of the pixel above TRESHOLD is set to white

% isRoundPixel

round(TRESHOLD/100\*MAXIMUM);

TRESHOLD = 80; MAXIMUM = 2^16-1; TRESHOLD =

% - only valid for png images encoded in 16 bits

% - TRESHOLD range is from 0 to 100.

% set to black (=0) and above TRESHOLD to white (= 65535 = 2^16-1).

% TRESHOLD value. Every pixel value below TRESHOLD will be

NBIMAGE = 165;

% Number of images to be processed

%%%

%% Parameters

%%%

```

%% Global variables initialization
%%%%%%%%%%%%%%%%%%%%%%%%%%%%%%%%%%%%%%%%%%%%%%%%%%%%%%%%%%%%%%%%%%%%%%%%
g_area      = zeros(NBIMAGE,1); g_x      = zeros(NBIMAGE,1); g_y
= zeros(NBIMAGE,1); g_high      = zeros(NBIMAGE,1); g_nbPixel =
zeros(NBIMAGE,10);

%%%%%%%%%%%%%%%%%%%%%%%%%%%%%%%%%%%%%%%%%%%%%%%%%%%%%%%%%%%%%%%%%%%%%%%%
%% Conversion value: from pixel to microns
%%%%%%%%%%%%%%%%%%%%%%%%%%%%%%%%%%%%%%%%%%%%%%%%%%%%%%%%%%%%%%%%%%%%%%%%
ppi_x = 10.22; ppi_y = 9.72;
%ppi_x = 8.4; ppi_y = 9.8;

%%%%%%%%%%%%%%%%%%%%%%%%%%%%%%%%%%%%%%%%%%%%%%%%%%%%%%%%%%%%%%%%%%%%%%%%
%% Main
%%%%%%%%%%%%%%%%%%%%%%%%%%%%%%%%%%%%%%%%%%%%%%%%%%%%%%%%%%%%%%%%%%%%%%%%

% Data
x_c = []; y_c = [];

% Create waitbar
h = waitbar(0,'Processing...'); posbar = get(h,'Position');
set(h,'Position',[posbar(1) 100 posbar(3) posbar(4)]);

for i=1:NBIMAGE

    % Update waitbar

```

```
waitbar(i/NBIMAGE,h)

% Create the image name
if(i < 10)
    str_num = [ '0' num2str(i) ];
else
    str_num = num2str(i);
end
fname = [ 'image' str_num '.png' ] ;

% Read image
I = imread(fname);

% Debug - display info about the image
info = imfinfo(fname);

% Debug - check type
class(I);

% Convert values to double - Replacing by single does make any
% difference
pic = double(I(:, :, 1));

% Get the size
[ m, n ] = size(pic);
```

```
% Find the centroid - pic is assumed to have been converted
% to double already
[ xx, yy, err ] = extract_centroid(pic,i,isRoundPixel);

% Store data
x_c = [ x_c xx ];
y_c = [ y_c yy ];

if err == 1
    buf = sprintf('TRESHOLD is too high: stopped calculation
    at image %s.',fname);
    disp(buf)
    close(h);
    return;
end
end

% Convert to microns
x_c = x_c*ppi_x; y_c = y_c*ppi_y;

% Close bar
close(h);

% First figure
figure,subplot(2,1,1),plot(x_c,':+r')
grid on
```

```
title('X Centroid Pixel Positions VS Image Number')
xlabel('Image Number') ylabel('X Centroid Position (microns)')
subplot(2,1,2),plot(y_c,':+r')
grid on
title('Y Centroid Pixel Positions VS Image Number')
xlabel('Image Number') ylabel('Y Centroid Position (microns)')

% Second figure
figure bar(g_nbPixel,'stacked')
grid on
set(gca,'xlim',[1length(g_nbPixel)])
xlabel('Image Number') ylabel('Nb of pixels')
title('Distribution of pixel values')

% Third figure
figure plot(g_high,':+r') grid on xlabel('Image Number')
ylabel('Maximum pixel value')

% Write results in an excel file
[SUCCESS,MESSAGE]=xlswrite('.\Centroids.xls',[x_c' y_c']);

% Open time text file (comes from LabVIEW)
fidt = fopen('time.txt','r');
t     = fscanf(fidt,'%f');
fclose(fidt);
```

```

% Scale time (see LabVIEW code)

t = t*20.0;

% Scale deformation (see LabVIEW code) with 8 is the def scale.
% Translate to t(2)

% Fourth figure
for i=2:length(t)
    defTh(i) = x_c(2)-8*time2def(t(i)-t(2));
end figure grid on hold on
plot(t(2:length(t)),x_c(2:length(t))-x_c(2),'.-k')
plot(t(2:length(t)),defTh(2)-defTh(2:length(t)), 'o-k') title('X
Centroid Pixel Positions VS Image Number') xlabel('Image Number')
ylabel('X Centroid Position (microns)')

% Write results in an excel file
v1 = t(2:length(t)); v2 = x_c(2:length(t))-x_c(2); v3 =
defTh(2)-defTh(2:length(t));
[SUCCESS,MESSAGE]=xlswrite('.\lastexp.xls',[v1 v2' v3']);

return;

%%%%%%%%%%%%%%%%%%%%%%%%%%%%%%%%%%%%%%%%%%%%%%%%%%%%%%%%%%%%%%%%%%%%%%%%
% Name      : extract_centroid.m
% Author    : Pranchalee Poonyapak
% Created   : January 2005
% Description : Extract centroid coordinate(pixel value)

```

```

%           of a laser spot from an input image
%%%%%%%%%%%%%%%%%%%%%%%%%%%%%%%%%%%%%%%%%%%%%%%%%%%%%%%%%%%%%%%%%%%%%%%%
function [ x, y, err ] = extract_centroid(myImage,idx,isRoundPixel)

global g_x g_y g_high g_nbPixel TRESHOLD SIZEBOX MAXIMUM

% Initialize some variables
x      = 0.0; y      = 0.0; err      = 0.0; pic      = myImage;

% Locate every pair of indices where the maximum is reached
[col, row] = find(pic == max(max(pic)));

% Record the highest pixel value in the image
g_high(idx) = pic(col(1),row(1))/MAXIMUM;

% Find the middle of these pairs: it is located at pic(cc,rr)
rr = ( min(row) + max(row) )/2; cc = ( min(col) + max(col) )/2;

% Extract a box around it of size SIZEBOX
[m, n] = size(pic);
minc = max(1,round(cc - SIZEBOX));
maxc = min(round(cc + SIZEBOX),m);
minr = max(1,round(rr - SIZEBOX));
maxr = min(round(rr + SIZEBOX),n);
small_pic = pic(minc:maxc, minr:maxr);
[small_m, small_n] = size(small_pic);

```

```
% Parse and set 0 below the TRESHOLD value
for i=1:small_m
    for j=1:small_n
        if small_pic(i,j) > 0.0

% Counting pixels for intensity distribution
        normalizedPixel = small_pic(i,j)/MAXIMUM;
        if 0.0 <= normalizedPixel & normalizedPixel < 0.1
            g_nbPixel(idx,1) = g_nbPixel(idx,1) + 1;
        elseif 0.1 <= normalizedPixel & normalizedPixel < 0.2
            g_nbPixel(idx,2) = g_nbPixel(idx,2) + 1;
        elseif 0.2 <= normalizedPixel & normalizedPixel < 0.3
            g_nbPixel(idx,3) = g_nbPixel(idx,3) + 1;
        elseif 0.3 <= normalizedPixel & normalizedPixel < 0.4
            g_nbPixel(idx,4) = g_nbPixel(idx,4) + 1;
        elseif 0.4 <= normalizedPixel & normalizedPixel < 0.5
            g_nbPixel(idx,5) = g_nbPixel(idx,5) + 1;
        elseif 0.5 <= normalizedPixel & normalizedPixel < 0.6
            g_nbPixel(idx,6) = g_nbPixel(idx,6) + 1;
        elseif 0.6 <= normalizedPixel & normalizedPixel < 0.7
            g_nbPixel(idx,7) = g_nbPixel(idx,7) + 1;
        elseif 0.7 <= normalizedPixel & normalizedPixel < 0.8
            g_nbPixel(idx,8) = g_nbPixel(idx,8) + 1;
        elseif 0.8 <= normalizedPixel & normalizedPixel < 0.9
            g_nbPixel(idx,9) = g_nbPixel(idx,9) + 1;
```

```
elseif 0.9 <= normalizedPixel & normalizedPixel < 1.0
    g_nbPixel(idx,10) = g_nbPixel(idx,10) + 1;
end

% Filtering - for extracting images with small laser spots, don't need
if small_pic(i,j) < TRESHOLD
    small_pic(i,j) = 0.0;
else
    if isRoundPixel == 1
        small_pic(i,j) = 1.0;
    end
end
end
end

end

% Compute the total area
area = 0; for(i = 1:small_m)
    for(j = 1:small_n)
        area = area + small_pic(i, j);
    end
end

% If the total area is 0, the TRESHOLD is too high, then stop
if area == 0
    err = 1;
```

```
        return
end

% Compute the weighted average of x (first moment)
for(i = 1:small_m)
    for(j = 1:small_n)
        x = x + (j-1)*small_pic(i, j);
    end
end x = x/area;

% Compute the weighted average of y (first moment)
for(i = 1:small_m)
    for(j = 1:small_n)
        y = y + (i-1)*small_pic(i, j);
    end
end y = y/area;

% Find the proper coordinates
x = x + minr; y = y + minc;

g_x(idx) = x; g_y(idx) = y;

return;
```

## A.2 Predictive Deformation Generations

To utilize the deformation results, obtained from any of the three models of the two-link experiment, as an input for the compensation algorithm, the source of the deformation results were simplified. The deformation results were regenerated via curve fitting, and the curve-fitted function was implemented in the MATLAB code, *time2def*, for predictive deformation generation. The same curve-fitted function was also implemented in the LabVIEW virtual instrument for the compensation algorithm (see Appendix B). Figure A.4 shows the predictive deformation generated by *time2def* plotted over time. The *time2def* MATLAB code is also presented below.

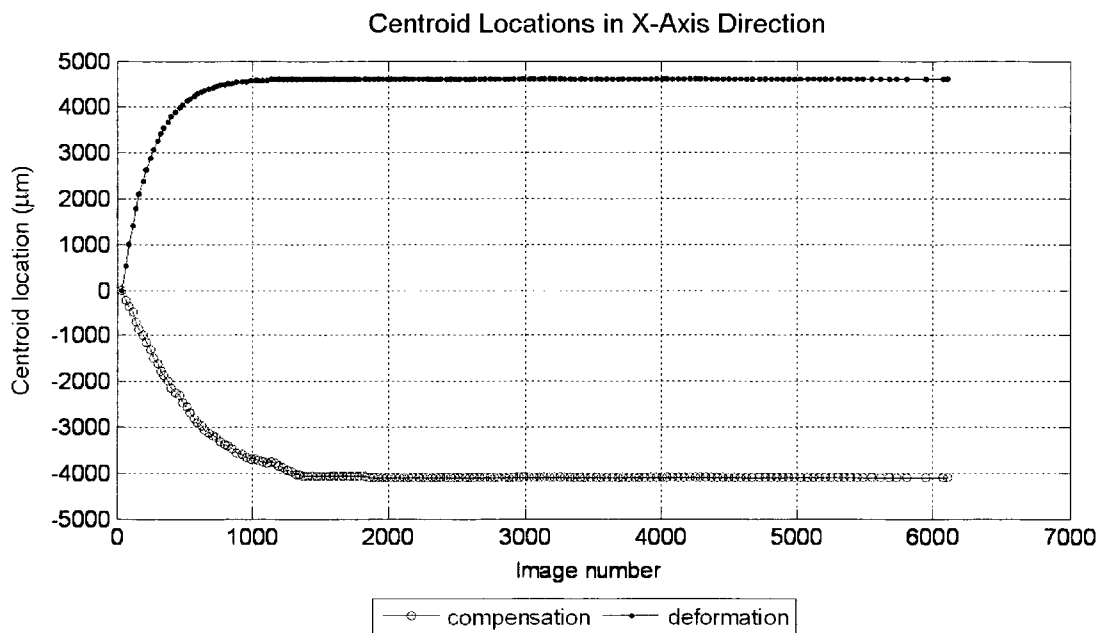


Figure A.4: Locations of laser spot centroids required for compensation corresponding to the deformation.

```
%%%%%%%%%%%%%%%%%%%%%%%%%%%%%%%%%%%%%%%%%%%%%%%%%%%%%%%%%%
% Name      : time2def.m
% Author    : Pranchalee Poonyapak
```

```
% Created : January 2009
% Description : Provide the predictive deformation given the time.
%             The equation has been obtained by fitting
%             the experimental data.
%             This function is also used in the LabVIEW code.
%%%%%%%%%%%%%%%%%%%%%%%%%%%%%%%%%%%%%%%%%%%%%%%%%%%%%%%%%%%%%%%%%%%%%%%%
function [def] = time2def(t)

def = 577.7035*(1-exp(-0.0047*t));
```

# Appendix B

## LabView Virtual Instruments

Two LabVIEW virtual instruments developed in this thesis research were built on techniques of the measurement acquisition virtual instrument of [39]. The original virtual instrument was modified to be able to communicate with the IR camera, and provide required compensation for the deformation. Also, the process time of the virtual instrument was improved by opening and closing the communication port only once at the beginning and end of the experiment, instead of opening and closing the port for each loop of the experiment.

The first virtual instrument, communication virtual instrument, facilitated the communication between the development computer, CCD camera, IR camera and robot controller. The instrument managed and scheduled the image acquiring processes of both a CCD and an IR cameras, and the required robot motions. The second virtual instrument, compensation algorithm virtual instrument, was developed based on the virtual instrument, with the additional features to compute and provide required compensation for the deformation via robot motions. As the IR camera was not required for the compensation algorithm, therefore, it was excluded from the compensation virtual instrument.

The front panel of the communication virtual instrument is shown in Figure B.1. The

communication port, storing location of the images acquired by the cameras, trial and name of images, and maximum and minimum reference voltages of the CCD camera were specified in the virtual instrument. Each acquired laser spot image was also presented in the front panel of the virtual instrument to confirm the quality of the image. The flow diagram of the communication virtual instrument and the description of the diagram are presented in Figure 3.4 and Section 3.2.3 respectively.

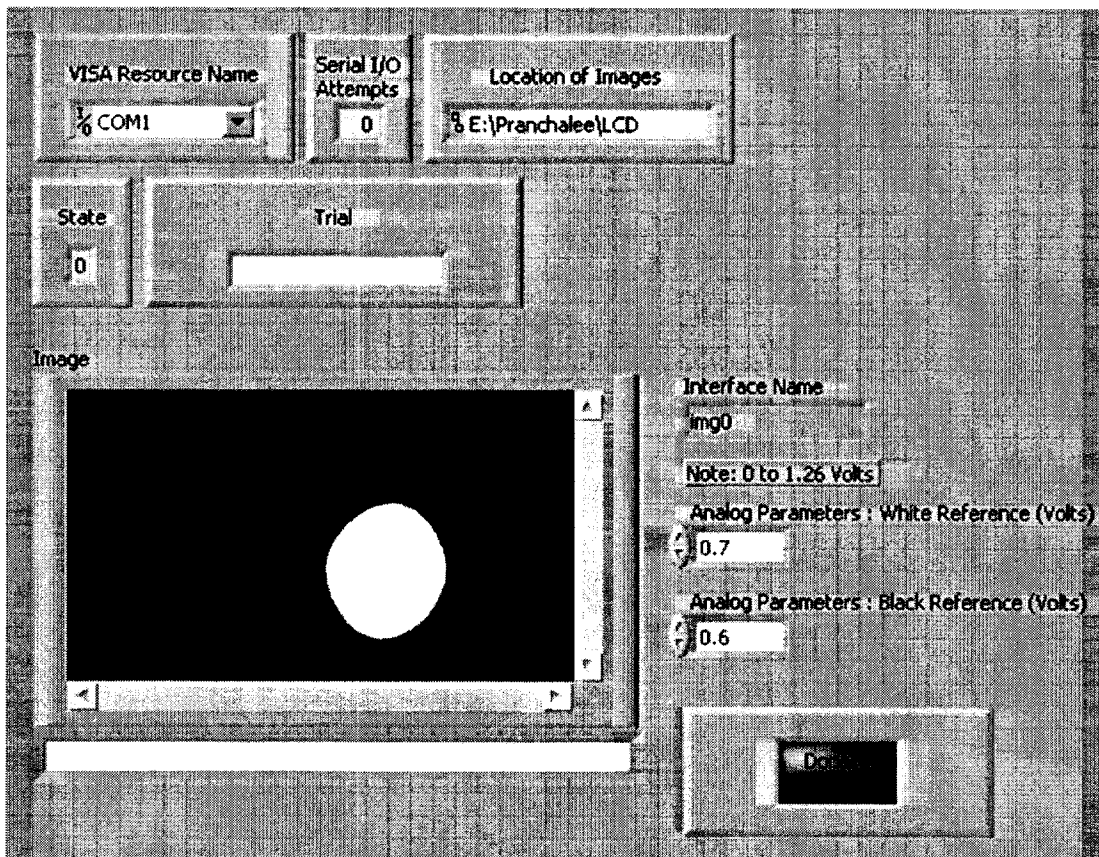


Figure B.1: Front panel of image acquisition and robot motion control process.

Figure B.2 illustrates the front panel of the compensation virtual instrument. Similar to the communication virtual instrument, the communication port, maximum and minimum reference voltages of the CCD camera were specified in the compensation virtual instrument. The additional feature related to the compensation algorithm were the deformation over time graph, which was used as the input for the compensation, and the

scaling factors of time and input deformation required for compensation experiment.

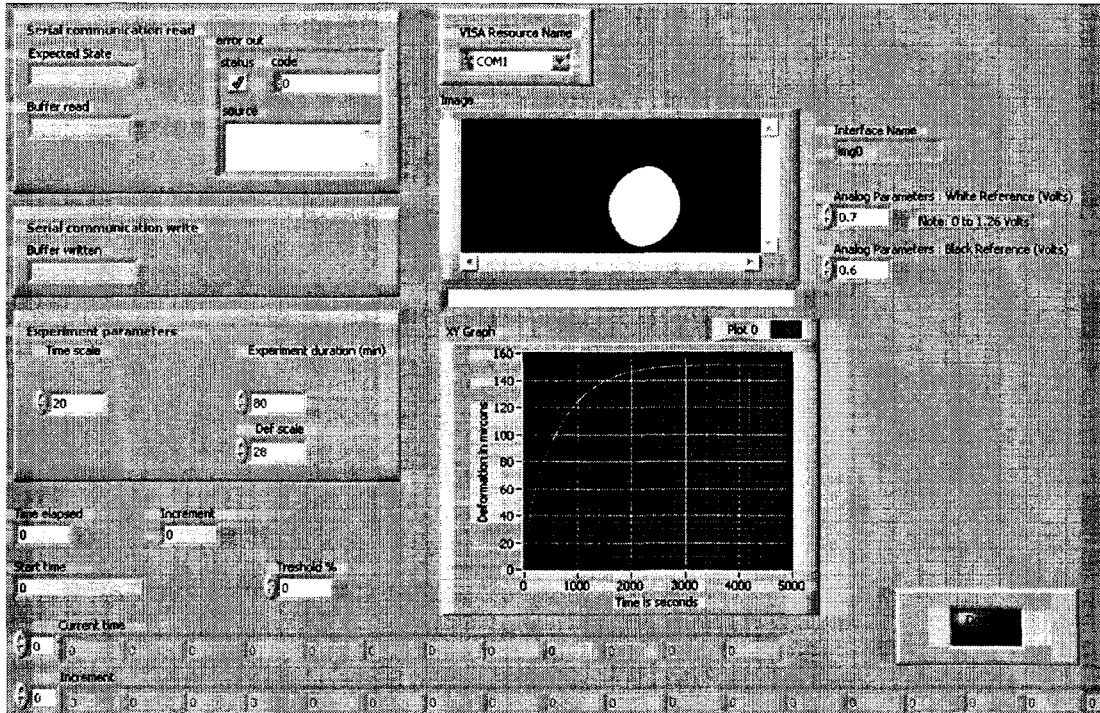


Figure B.2: Front panel of compensation algorithm LabView virtual instrument.

The flow diagram of the compensation virtual instrument is presented in Figure B.3. The core procedure is similar to that of the communication virtual instrument. The commands related to the IR camera were removed, and the commands related to the computation and assignment of the robot motion for the compensation were added.

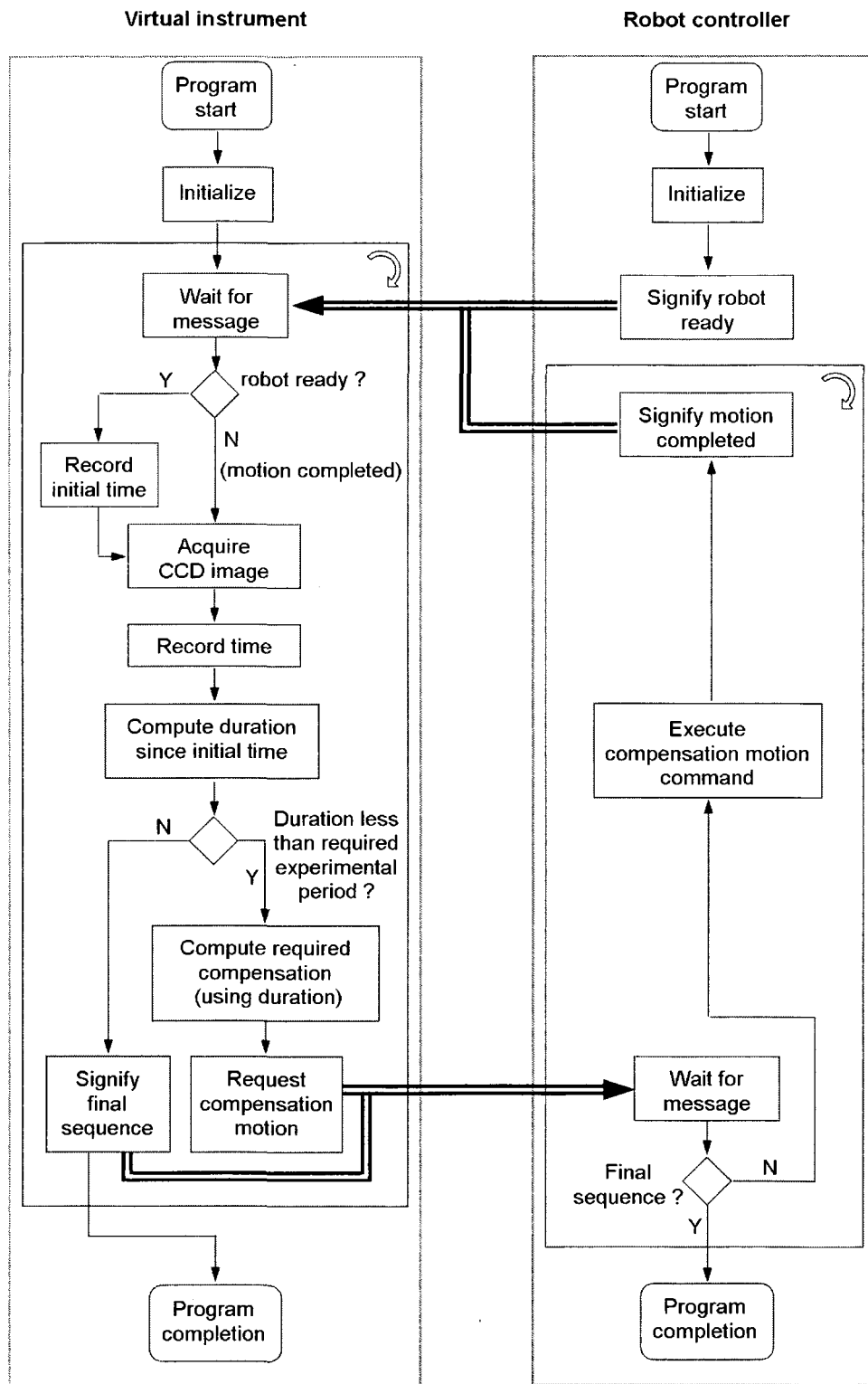


Figure B.3: Flow diagram of compensation algorithm.

# Appendix C

## Statistical Analysis from Validation

### Experiments

Table C.1: Intervals and frequency distribution of errors from incremental location command.

j	Interval	$n_j$	j	Interval	$n_j$
1	$-4.40 \leq x_i < -3.68$	2	9	$1.36 \leq x_i < 2.08$	11
2	$-3.68 \leq x_i < -2.96$	4	10	$2.08 \leq x_i < 2.8$	9
3	$-2.96 \leq x_i < -2.24$	7	11	$2.8 \leq x_i < 3.52$	8
4	$-2.24 \leq x_i < -1.52$	10	12	$3.52 \leq x_i < 4.24$	5
5	$-1.52 \leq x_i < -0.80$	13	13	$4.24 \leq x_i < 4.96$	3
6	$-0.80 \leq x_i < -0.08$	20	14	$4.96 \leq x_i < 5.68$	2
7	$-0.08 \leq x_i < 0.64$	22	15	$5.68 \leq x_i < 6.40$	1
8	$0.64 \leq x_i < 1.36$	26			

Table C.2: Intervals and frequency distribution of errors from absolute location command.

j	Interval	$n_j$	j	Interval	$n_j$
1	$-2.55 \leq x_i < -2.18$	1	9	$0.41 \leq x_i < 0.78$	19
2	$-2.18 \leq x_i < -1.81$	1	10	$0.78 \leq x_i < 1.15$	11
3	$-1.81 \leq x_i < -1.44$	5	11	$1.15 \leq x_i < 1.52$	8
4	$-1.44 \leq x_i < -1.07$	8	12	$1.52 \leq x_i < 1.89$	5
5	$-1.07 \leq x_i < -0.7$	15	13	$1.89 \leq x_i < 2.26$	2
6	$-0.7 \leq x_i < -0.33$	21	14	$2.26 \leq x_i < 2.63$	0
7	$-0.33 \leq x_i < 0.04$	22	15	$2.63 \leq x_i < 3$	1
8	$0.04 \leq x_i < 0.41$	24			

Table C.3: Chi-squared test for errors from incremental location command.

j	$n_j$	$n'_j$	$\frac{(n_j - n'_j)^2}{n'_j}$	j	$n_j$	$n'_j$	$\frac{(n_j - n'_j)^2}{n'_j}$
1	3	2.20	0.019	9	3	15.86	1.820
2	4	4.23	0.012	10	9	12.07	0.779
3	6	7.22	0.007	11	7	8.18	0.004
4	10	10.99	0.090	12	4	4.93	0.001
5	14	14.91	0.244	13	4	2.65	0.045
6	32	18.01	0.220	14	2	1.27	0.418
7	35	19.38	0.695	15	2	0.54	0.387
8	8	32.81	1.744	$\chi^2 = 6.48$			

Table C.4: Chi-squared test for errors from absolute location command.

j	$n_j$	$n'_j$	$\frac{(n_j - n'_j)^2}{n'_j}$	j	$n_j$	$n'_j$	$\frac{(n_j - n'_j)^2}{n'_j}$
1	1	0.86	0.022	9	19	18.62	0.008
2	1	2.21	0.662	10	11	13.35	0.413
3	5	4.83	0.006	11	8	8.16	0.003
4	8	9.01	0.114	12	5	4.25	0.132
5	15	14.33	0.031	13	2	1.89	0.006
6	21	19.43	0.126	14	0	0.72	0.716
7	22	18.37	0.716	15	1	0.23	2.556
8	24	22.15	0.154	$\chi^2 = 5.66$			